

DEVELOPMENT OF Mg-BASED HYDRIDES FOR SOLID-STATE
HYDROGEN STORAGE AND BATTERY



PAMMARIN DANSIRIMA

A Thesis Submitted in Partial Fulfillment of the Requirements for the
Degree of Doctor of Philosophy in Chemistry
Suranaree University of Technology
Academic Year 2023

การพัฒนาวัสดุไฮโดรด์ของแมกนีเซียมเพื่อใช้ในการกักเก็บพลังงาน
ไฮโดรเจนและแบตเตอรี่ชนิดของแข็ง



นางสาวปาล์มริน แदनศิริมา

วิทยานิพนธ์นี้เป็นส่วนหนึ่งของการศึกษาตามหลักสูตรปริญญาวิทยาศาสตรดุษฎีบัณฑิต
สาขาวิชาเคมี
มหาวิทยาลัยเทคโนโลยีสุรนารี
ปีการศึกษา 2566

DEVELOPMENT OF Mg-BASED HYDRIDES FOR SOLID-STATE
HYDROGEN STORAGE AND BATTERY

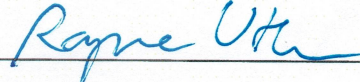
Suranaree University of Technology has approved this thesis submitted in
partial fulfillment of the requirements for the Degree of Doctor of Philosophy

Thesis Examining Committee



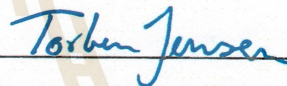
(Assoc. Prof. Dr. Anyanee Kamkaew)

Chairperson



(Assoc. Prof. Dr. Rapee Utke)

Member (Thesis Advisor)



(Prof. Dr. Torben René Jensen)

Member (Thesis Co-advisor)



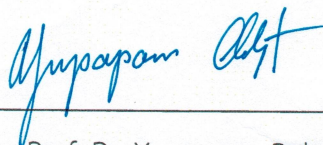
(Prof. Dr. Jatuporn Wittayakun)

Member



(Assoc. Prof. Dr. Theeranun Siritanon)


Member



(Assoc. Prof. Dr. Yupaporn Ruksakulpiwat)

Vice Rector for Academic Affairs

and Quality Assurance



(Prof. Dr. Santi Maensiri)

Dean of Institute of Science

ปาล์มริน แดนศิริมา : การพัฒนาวัสดุไฮโดรด์ของแมกนีเซียมเพื่อใช้ในการกักเก็บพลังงานไฮโดรเจนและแบตเตอรี่ชนิดของแข็ง (DEVELOPMENT OF Mg-BASED HYDRIDES FOR SOLID-STATE HYDROGEN STORAGE AND BATTERY) อาจารย์ที่ปรึกษา : รองศาสตราจารย์ ดร.ระพี อุทเคอ, 98 หน้า

คำสำคัญ: การกักเก็บไฮโดรเจนชนิดของแข็ง วัสดุไฮโดรด์แมกนีเซียม การบรรจุระดับนาโน แบตเตอรี่แมกนีเซียมชนิดของแข็ง การนำไอออนแมกนีเซียม

วิทยานิพนธ์เล่มนี้นำเสนอการศึกษาวัสดุไฮโดรด์แมกนีเซียม โดยเน้นการใช้งานในการกักเก็บไฮโดรเจนและแบตเตอรี่แมกนีเซียมชนิดของแข็ง ประสิทธิภาพการกักเก็บและปลดปล่อยไฮโดรเจนกลไกการเกิดปฏิกิริยาของสารประกอบคอมโพสิต $2\text{LiBH}_4\text{-MgH}_2$ ที่บรรจุในรูพรุนระดับนาโนเมตรของคาร์บอนกัมมันต์ถูกศึกษาในระดับถังกักเก็บขนาดเล็ก (21.7 มิลลิลิตร) จากการศึกษาพบว่าวัสดุคอมโพสิต $2\text{LiBH}_4\text{-MgH}_2$ ที่บรรจุในรูพรุนระดับนาโนเมตรของคาร์บอนกัมมันต์มีความจุไฮโดรเจนที่ผันกลับได้ 3.56 -4.55 และ 2.03-3.28 เปอร์เซ็นต์โดยน้ำหนัก ซึ่งเป็นความจุไฮโดรเจนรวมและความจุไฮโดรเจนของวัสดุตามลำดับ ความจุไฮโดรเจนที่ต่ำกว่าความจุทางทฤษฎีของวัสดุ (5.7 เปอร์เซ็นต์โดยมวล) เกิดจากปฏิกิริยาการปลดปล่อยไฮโดรเจนบางส่วนของวัสดุระหว่างการเตรียมตัวอย่างปฏิกิริยาการปลดปล่อยไฮโดรเจนที่ไม่สมบูรณ์ของ LiBH_4 และการเกิดสารประกอบที่มีความเสถียรทางความร้อน ($\text{Li}_2\text{B}_{12}\text{H}_{12}$) ระหว่างการทดลองกักเก็บและปลดปล่อยไฮโดรเจน นอกจากนี้ยังพบกลไกการเกิดปฏิกิริยาปลดปล่อยไฮโดรเจนที่หลากหลายภายในถังกักเก็บ การเพิ่มประสิทธิภาพการนำความร้อนตลอดจนระบบการควบคุมอุณหภูมิ และความสามารถในการแพร่ผ่านของแก๊สไฮโดรเจนภายในถังกักเก็บ จึงเป็นปัจจัยสำคัญในการเพิ่มประสิทธิภาพการกักเก็บไฮโดรเจน

การผลิตกระแสไฟฟ้าอย่างมีประสิทธิภาพจากถังกักเก็บไฮโดรเจนโดยใช้เซลล์เชื้อเพลิงจำเป็นต้องอาศัยแหล่งจ่ายไฮโดรเจนที่มีความเสถียรเป็นเวลานาน คุณสมบัติทางจลนพลศาสตร์ของการปลดปล่อยไฮโดรเจนจากถังกักเก็บไฮโดรเจนเป็นสมบัติที่ขึ้นอุณหภูมิและความดันของระบบ การศึกษาประสิทธิภาพการกักเก็บและปลดปล่อยไฮโดรเจนของวัสดุ $\text{TiF}_4\text{-MWCNT-MgH}_2$ (~45 g) ที่บรรจุในถังกักเก็บทรงกระบอกขนาด 96.2 มิลลิลิตร โดยมีท่อแลกเปลี่ยนความร้อนบริเวณกลางถังกักเก็บพบว่า วัสดุมีความจุไฮโดรเจนที่สามารถผันกลับได้ 5.4 เปอร์เซ็นต์โดยน้ำหนักระหว่างการทดลองกักเก็บและปล่อยไฮโดรเจน 20 รอบ การปรับอุณหภูมิและอัตราเร็วของการปลดปล่อยไฮโดรเจน

ส่งผลต่อคุณสมบัติทางจลนพลศาสตร์ นอกจากนี้ยังมีการศึกษาประสิทธิภาพการกักเก็บและปลดปล่อยไฮโดรเจนในทิศทางตามแนวแกนและรัศมีของถังกักเก็บ ตลอดจนพฤติกรรมทางจลนพลศาสตร์ และขั้นตอนกำหนดอัตราของปฏิกิริยาปลดปล่อยไฮโดรเจน ที่อุณหภูมิและอัตราเร็วของการปลดปล่อยไฮโดรเจนที่ 300-340 องศาเซลเซียส และ 0.6-1.0 ลิตรมาตรฐานต่อนาทีตามลำดับ

ทั้งนี้ ยังมีการศึกษาผลของการบรรจุระดับนาโนเมตรต่อการนำไอออนแมกนีเซียมของคอมโพสิต $(Mg(BH_4)_2 \cdot NH_3)_x (Mg(BH_4)_2 \cdot 2NH_3)_{1-x}$ ที่บรรจุระดับนาโนเมตรในรูพรุนของซิลิกอนออกไซด์ที่มีรูพรุนขนาดกลาง ที่มีระดับการเติมเต็มรูพรุน (degree of pore filling) ที่แตกต่างกัน ตั้งแต่ 100–300 เปอร์เซ็นต์ ทำได้ด้วยวิธีการแทรกซึมละลาย จากวิเคราะห์ด้วยเทคนิคนิวเคลียร์แมกเนติกเรโซแนนซ์สเปกโทรสโกปีของธาตุโบรอน (Solid-state ^{11}B nuclear magnetic resonance) พบว่าวัสดุคอมโพสิต $Mg(BH_4)_2 \cdot 1.47NH_3$ ในสถานะห่อหุ้มเหลวที่มีพลวัตสูงถูกบรรจุอยู่รูพรุนของซิลิกอนออกไซด์ที่มีรูพรุนขนาดกลางได้อย่างเสถียร โดยตัวอย่างที่มีระดับการเติมเต็มรูพรุน 200 เปอร์เซ็นต์ มีความนำไอออนแมกนีเซียม $9.1 \times 10^{-6} - 2.7 \times 10^{-4}$ ซีเมนส์ต่อเซ็นติเมตร และพลังงานก่อกัมมันต์ 0.69 eV ในช่วงอุณหภูมิ 32-80 องศาเซลเซียส

มหาวิทยาลัยเทคโนโลยีสุรนารี

สาขาวิชาเคมี

ลายมือชื่อนักศึกษา ปาศิรินทร์ ทอนเสวีวง

ปีการศึกษา 2566

ลายมือชื่ออาจารย์ที่ปรึกษา อนุชิต

PAMMARIN DANSIRIMA : DEVELOPMENT OF Mg-BASED HYDRIDES FOR SOLID-STATE HYDROGEN STORAGE AND BATTERY. THESIS ADVISOR : ASSOC. PROF. RAPEE UTKE, Ph.D. 98 PP.

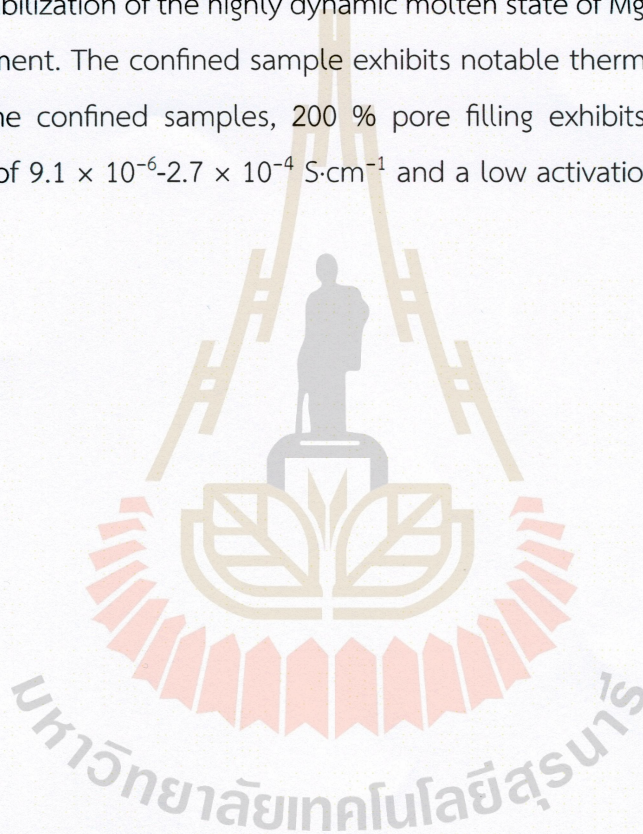
Keywords: Solid-state hydrogen storage, Mg-based hydride materials, Nanoconfinement, Solid-state magnesium batteries, Magnesium ion conductivity,

The thesis focusses on the utilization of Mg-based hydride materials in solid-state hydrogen storages and batteries. Regarding solid-state hydrogen storage, de/rehydrogenation performances and reaction pathways of nanoconfined $2\text{LiBH}_4\text{-MgH}_2$ into activated carbon (AC) in a small hydrogen storage tank (21.7 mL) are investigated for the first time. The study reveals total and material storage capacities of 3.56-4.55 and 2.03-3.28 wt. % H_2 , respectively, upon five de/rehydrogenation cycles. Inferior hydrogen content to theoretical material capacity (5.7 wt. % H_2) is due to partial dehydrogenation during sample preparation, incomplete decomposition of LiBH_4 , and the formation of thermally stable $\text{Li}_2\text{B}_{12}\text{H}_{12}$ upon cycling. Various reaction pathways are identified at different positions inside the tank, emphasizing the need for further development to enhance thermal conductivity, temperature control systems, and hydrogen permeability for efficient hydrogen storage.

The optimal electrical generation from fuel cells coupled with hydrogen storage tanks based on hydrides can be achieved through consistent supply of hydrogen over a long period of time. Dehydrogenation kinetics of hydride-based tanks strongly depends on the operating temperatures and system pressures. A cylindrical tank (96.2 mL) equipped with a central heat exchanger packed with $\text{TiF}_4\text{-MWCNT-MgH}_2$ (~45 g) exhibits admirable de/rehydrogenation and reversibility (5.4 wt. % H_2 upon 20 cycles). The optimization of kinetic properties either rapid or steady-state desorption can be achieved by simultaneously adjusting the operating temperature and H_2 mass flow rate. The performances in the axial and radial directions of the tank as well as kinetic behaviors and rate-limiting step during dehydrogenation at different

temperatures of 300-340 °C and H₂-FR of 0.6-1.0 standard L/min of MgH₂-based tank are studied.

With regards to solid-state battery, the effects of nanoconfinement on the Mg²⁺ ionic conductivity of the (Mg(BH₄)₂·NH₃)_x(Mg(BH₄)₂·2NH₃)_{1-x} composite are explored. The synthesis of nanoconfined Mg(BH₄)₂·1.47NH₃ in a mesoporous silica scaffold (SBA-15 with the pore size of 5.8 nm) with different degrees of pore filling (100-300 %) is done by melt infiltration. Solid-state ¹¹B nuclear magnetic resonance analysis confirms the successful stabilization of the highly dynamic molten state of Mg(BH₄)₂·1.47NH₃ through nanoconfinement. The confined sample exhibits notable thermal stability up to ~100 °C. Among the confined samples, 200 % pore filling exhibits promising Mg²⁺ ionic conductivity of 9.1×10^{-6} - 2.7×10^{-4} S·cm⁻¹ and a low activation energy of 0.69 eV at T= 32-80 °C.



School of Chemistry
Academic Year 2023

Student's Signature พัลลภรัตน์ แอนดริอานา

Advisor's Signature ดร. กฤษณะ

ACKNOWLEDGEMENTS

As a Ph.D. student, I have gained extensive knowledge and valuable experiences. In this regard, I wish to extend my heartfelt gratitude to the individuals whose support was influential in the completion of my thesis, enabling me to successfully achieve my goal of earning a Ph.D.

I express my sincere gratitude to the School of Chemistry, Institute of Science, Suranaree University of Technology, for providing me with an inspiring and conducive environment for conducting my research. The resources and support offered by the institution have been invaluable throughout my academic journey. My heartfelt thanks goes to Assoc. Prof. Dr. Rapee Utke, my thesis supervisor, for her guidance, mentorship, and unwavering support throughout this research work. Her expertise and dedication have been instrumental in shaping the direction of my work. I extend my appreciation to my fellow researchers in the HS lab for their company, support, and the collaborative spirit that enriched my research experience.

I express my sincere appreciation for the financial support provided by The Royal Golden Jubilee Ph.D. Program. This scholarship has allowed me to focus on my studies and research, contributing significantly to the successful completion of this thesis.

Prof. Dr. Torben René Jensen is acknowledged as a fantastic advisor during my study at the Department of Chemistry, Aarhus University, Denmark. It was my fortune and honor to have such a great opportunity in my life. The insights and perspectives shared during our interactions have added valuable dimensions to my research. I also appreciate his kindness and support. I would like to express my gratitude to the members of Prof. Dr. Torben René Jensen's lab for their collaboration and contributions to this study; their expertise has been invaluable. Special thanks to Dr. Jakob B. Grinderslev and Lasse G. Kristensen for their kind help, suggestions, and assistance throughout my stay.

To my friends, especially Kesara Ar-sanork, Nawee Jantarit, and Puttimate Thongtan, thank you for your steady support, encouragement, and understanding during the ups and downs of this academic journey. Your friendship has been a constant source of inspiration.

Finally, to my family, thank you for your unconditional love, encouragement, and belief in my abilities. Your support has been my anchor, and this achievement is as much yours as it is mine.

Each of you has played a vital role in the completion of this thesis, and for that, I am truly grateful.

Pammarin Dansirima



CONTENTS

	Page
ABSTRACT IN THAI	I
ABSTRACT IN ENGLISH	III
ACKNOWLEDGEMENTS	V
CONTENTS	VII
LIST OF TABLES	IX
LIST OF FIGURES	X
CHAPTER	
I INTRODUCTION.....	1
1.1 Age of renewable energy.....	1
1.2 Hydrogen-related energy storages.....	3
1.3 Batteries.....	5
1.4 References.....	7
II LITERATURE REVIEWS.....	10
2.1 Fundamental principle of solid-state hydrides for hydrogen storage.....	10
2.2 Solid-state hydrogen storage materials.....	12
2.2.1 Metal alanates.....	15
2.2.2 Metal amides.....	16
2.2.3 Metal borohydrides.....	16
2.2.4 Mg-based hydrides.....	19
2.3 Mg-based solid-state batteries.....	21
2.3.1 Oxides.....	22
2.3.2 Metal–organic frameworks (MOFs).....	23
2.3.3 Chalcogenides.....	24
2.3.4 Polymers.....	25
2.3.5 Hydrides	26
2.4 References.....	27

CONTENTS (Continued)

		Page
III	EXPERIMENTAL SECTION	43
	3.1 Sample preparation.....	43
	3.1.1 Solid-state hydrogen storage.....	43
	3.1.1.1 Nanoconfined 2LiBH ₄ -MgH ₂ in activated carbon.....	43
	3.1.1.2 MgH ₂ doped with TiF ₄ and MWCNTs	44
	3.1.2 Mg-based solid-state batteries.....	46
	3.1.2.1 Nanoconfined Mg(BH ₄) ₂ in mesoporous silica	46
	3.2 Characterizations.....	47
	3.2.1 Powder x-ray diffraction	47
	3.2.2 Fourier-transform infrared spectroscopy.....	48
	3.2.3 Solid-state nuclear magnetic resonance spectroscopy.....	48
	3.2.4 N ₂ adsorption-desorption.....	48
	3.2.5 Thermal analysis.....	49
	3.2.6 Sievert type apparatus.....	49
	3.2.7 Rate-limiting step determination.....	50
	3.2.8 Electrochemical impedance spectroscopy.....	51
	3.3 References.....	52
IV	RESULTS AND DISCUSSION	54
	4.1 Solid-state hydrogen storage.....	54
	4.1.1 Nano LB-MH-AC-based small hydrogen storage tank.....	54
	4.1.2 TiF ₄ -CNT-MH-based hydrogen storage tank.....	65
	4.2 Solid-state batteries.....	82
	4.2.1 Nanoconfinement of an ammine magnesium borohydride composite electrolyte in a mesoporous silica scaffold.....	82
	4.3 References.....	93
V	CONCLUSION	96
	CURRICULUM VITAE	98

LIST OF TABLES

Table	Page
1.1 U.S. Department of Energy targets for onboard hydrogen storage systems for light-duty vehicles.....	5
2.1 Examples of non-interstitial hydrides.....	15
3.1 Composition and degree of pore filling of samples.....	47
3.2 Gas-solid kinetic models for fitting the experimental data during dehydrogenation.....	51
4.1 Linewidth of the dominant resonance at -40 ppm for Mg(BH ₄)-1.47NH ₃ and MI100-300. It is not possible to get an accurate assessment of the starting compound due to significant peak overlap. All values are within the margin of error of the measurement.....	87
4.2 Magnesium ionic conductivity ($\sigma(\text{Mg}^{2+})$) and the activation energy (E_A) at the temperature range of 32 - 80 °C of MI100-300 and other amine magnesium borohydride nanocomposites.....	91

LIST OF FIGURES

Figure	Page
1.1 Global atmospheric CO ₂ concentration (A) and annual CO ₂ emission by world region (B).....	1
1.2 Share of renewable energy in power sector in 2011 and 2021.....	2
1.3 Electrical storage technologies and their appropriate applications.....	3
1.4 The envisioned infrastructure for harvesting hydrogen energy.....	4
1.5 A schematic diagram of a proton exchange membrane fuel cell.....	4
1.6 A schematic diagram of current ion batteries (A) and conventional solid-state batteries (B).....	6
2.1 Schematic illustration of solid solution phase (α -phase) (A), Pressure-Composition-Isotherm (PCI) and the deduced Van't Hoff plot(B), and hydride phase (β -phase) (C).	11
2.2 Van't Hoff plot of various hydride materials.	12
2.3 Interstitial hydrides (upper) and non-interstitial hydrides (bottom).....	13
2.4 The reaction mechanisms of interstitial (A) and non-interstitial (B) hydrides.....	14
2.5 Dehydrogenation enthalpies of 2LiBH ₄ + MgH ₂ composite and the single phase of LiBH ₄	17
2.6 The components (A) and cycling performance (B) of MgH ₂ -TiF ₄ -MWCNTs tank.....	21
2.7 Crystal structure of β -Fe ₂ (SO ₄) ₃ -type and NASICON-type of A _x M _y (XO ₄) ₃	23
2.8 Synthesis procedure of Cu[(Cu ₄ Cl)(ttpm) ₂] ₂ ·CuCl ₂ , Cu ₄ (ttpm) ₂ ·0.6CuCl ₂ , and the Target MOF-MX _n	24
3.1 Components of small hydrogen storage tank with packing volume of 21.7 mL (A) and the positions of thermocouples (TC1-TC3) in the tank (B).	44

LIST OF FIGURES (Continued)

Figure	Page
3.2 The components of the sample container (A) and the position of thermocouple inside the sample container (B) used for kinetic studies in laboratory scale.....	45
3.3 The components (A) and the positions of thermocouples inside the sample container (B) used for kinetic study in hydrogen storage tank scale (packing volume of 96.2 mL).....	46
4.1 Hydrogenation profile ($T_{\text{set}} = 400\text{ }^{\circ}\text{C}$ and $p(\text{H}_2) = 40\text{-}50\text{ bar}$)(A) and positions of TC1-TC3 in the tank as well as PXD (B) and FTIR (C) spectra of nano LB-MH-AC (1).....	55
4.2 DSC curves of the powder samples randomly collected from the tank (A) as well as PXD (B) and FTIR (C) spectra of nano LB-MH-AC (2).....	57
4.3 The 1 st dehydrogenation profile of LB-MH-AC (2) at $T_{\text{set}} = 350\text{ }^{\circ}\text{C}$	58
4.4 The PXD (A) and FTIR (B) spectra of dehydrogenated LB-MH-AC (2) at TC1-TC3.....	59
4.5 Rehydrogenation profile ($T_{\text{set}} = 350\text{ }^{\circ}\text{C}$ and $p(\text{H}_2) = 30\text{-}40\text{ bar}$) of LB-MH-AC (2).	60
4.6 The 2 nd dehydrogenation ($T_{\text{set}} = 350\text{ }^{\circ}\text{C}$) of LB-MH-AC (2).....	62
4.7 Dehydrogenation kinetics and reversibility upon five hydrogen release and uptake cycles of hydrogen storage tank.	62
4.8 PXD (A) and FTIR (B) spectra of the 5 th hydrogenated samples at TC1-TC3.....	64
4.9 PXD pattern (A) and hydrogen capacities upon de/rehydrogenation cycles (B) of as-prepared $\text{TiF}_4\text{-CNT-MH}$	65
4.10 Temperature, pressure, and hydrogen mass flow rate profiles (A), kinetics (B), and $(t/t_{0.5})_{\text{theoretical}}$ versus $(t/t_{0.5})_{\text{experimental}}$ plots fitted with different kinetic models (C) during dehydrogenation with $\text{H}_2\text{-FR}$ of 0.6 and 1.0 SLM of $\text{TiF}_4\text{-CNT-MH}$ in laboratory scale.....	66

LIST OF FIGURES (Continued)

Figure	Page
4.11 Temperature, pressure, and hydrogen mass flow rate profiles during dehydrogenation of TiF ₄ -CNT-MH at ~300 °C under 0.6 SLM (A), 0.8 SLM (B) and 1.0 SLM (C).	69
4.12 Temperature, pressure, and hydrogen mass flow rate profiles during dehydrogenation of TiF ₄ -CNT-MH tank under 0.6 SLM at 310 °C (A), 320 °C (B) and 340 °C (C).	71
4.13 Temperature, pressure, and hydrogen mass flow rate profiles during dehydrogenation of TiF ₄ -CNT-MH tank under 1.0 SLM at 310 °C (A), 320 °C (B) and 340 °C (C).	73
4.14 Dehydrogenation kinetics of TiF ₄ -CNT-MH tank at 300 °C under 0.6-1.0 SLM (A) and at 300-340 °C under 0.6 SLM (B) and 1.0 SLM (C).	75
4.15 Plots of $(t/t_{0.5})_{\text{theoretical}}$ versus $(t/t_{0.5})_{\text{experimental}}$ and model fitting during dehydrogenation of TiF ₄ -CNT-MH tank with H ₂ -FR of 0.6-1.0 SLM.	77
4.16 Plots of $(t/t_{0.5})_{\text{theoretical}}$ versus $(t/t_{0.5})_{\text{experimental}}$ and model fitting during dehydrogenation of TiF ₄ -CNT-MH tank at 310-340 °C with hydrogen mass flow rate of 0.6 SLM.	78
4.17 Plots of $(t/t_{0.5})_{\text{theoretical}}$ versus $(t/t_{0.5})_{\text{experimental}}$ and model fitting during dehydrogenation of TiF ₄ -CNT-MH tank at 310-340 °C with hydrogen mass flow rate of 1.0 SLM.	79
4.18 Rate-limiting step for desorption as a function of H ₂ -FR and temperatures of TiF ₄ -CNT-MH in laboratory and tank scales.	81
4.19 Nitrogen adsorption-desorption isotherms (A) and corresponding pore size distribution (B) of mesoporous silica SBA-15 after drying at 300 °C under dynamic vacuum overnight.	83
4.20 Rietveld refinement of powder X-ray diffraction (PXRD) data for as-prepared Mg(BH ₄) ₂ ·2NH ₃ and Mg(BH ₄)·NH ₃ composite ($\lambda = 1.54056 \text{ \AA}$).	84

LIST OF FIGURES (Continued)

Figure	Page
4.21 Powder X-ray diffraction diagrams of the composite, the scaffold and the nanoconfined samples, (A) after synthesis and (B) after 5 months of storage under argon atmosphere.....	85
4.22 Solid-state ^{11}B MAS NMR spectra, illustrating the central-transition region, for the composite and the nanoconfined samples.....	87
4.23 Mg^{2+} ion conductivity as a function of temperature of the MI100, MI200, and MI300 during the 2 nd heating cycle and the other ammine magnesium borohydrides doped with oxide nanoparticles.....	89
4.24 Temperature-dependent Mg^{2+} -ionic conductivities of the MI100-300 upon heating and cooling for 3 cycles at temperature range of 30–80 °C.....	90
4.25 Thermogravimetric analysis (TGA) - differential scanning calorimetry (DSC) and Mass spectroscopy (MS) results of as prepared $\text{Mg}(\text{BH}_4)_2 \cdot 1.5\text{NH}_3$ heated from 30 to 200 °C (2 °C min^{-1}). The mass loss in the temperature range 100 to 200 °C is $\Delta m/m = 5.7\text{ wt.}\%$, which corresponds to loss of 0.26 NH_3 molecules per formula unit. Black is hydrogen, blue is ammonia, red is diborane and green in water.....	92

CHAPTER I

INTRODUCTION

1.1 Age of renewable energy

Since the start of industrial revolution, the atmospheric CO₂ concentration has been increasing, leading to global warming and rising sea levels (Figure 1.1). In 2021, there was the record where the increase rates of the atmospheric CO₂ concentration are unprecedented over at least the last 800,000 years. The transformation of the global energy sector from fossil fuel to zero-carbon sources is the key success for the energy transition.

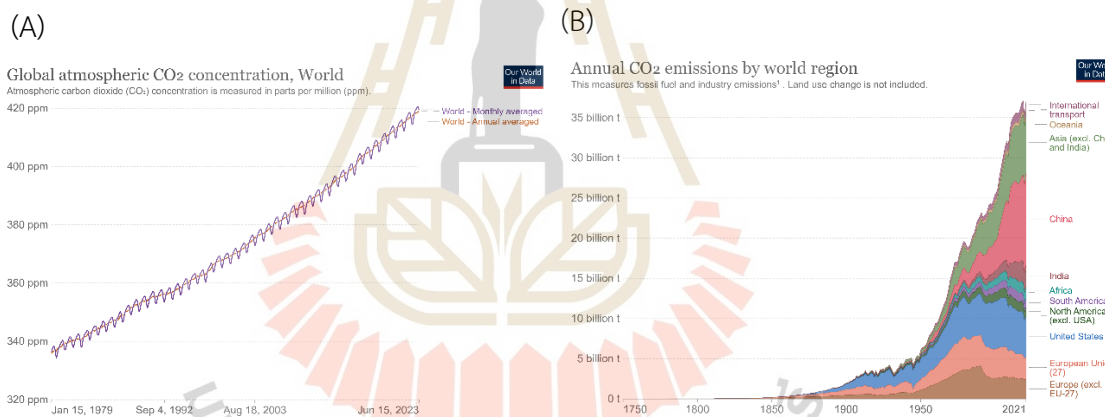


Figure 1.1 Global atmospheric CO₂ concentration (A) and annual CO₂ emission by world region (B). (“Annual CO₂ Emissions by World Region,” n.d.; “Greenhouse Gases Continued to Increase Rapidly in 2022,” 2023)

Renewable energy technologies harvest the power of the sun, wind, and heat from the Earth’s core and transform it into usable forms of energy, such as heat, electricity, and fuel. Although fossil fuels still dominate the global energy landscape, the share of renewable energy in the power sector increases from 20.4 to 28.3% from 2011 to 2021, especially solar and wind power (Figure 1.2). The international energy agency (IEA) forecasts a 60% growth in renewable energy from 2020’s levels by 2026,

equivalent to the combined current power output of fossil fuels and nuclear energy (Secretariat, 2022). Unfortunately, the production of electrical energy from natural sources depends on environmental conditions, e.g., solar and wind power. Therefore, the energy storage system (ESS) is required for integrating renewable power sources into the grid.

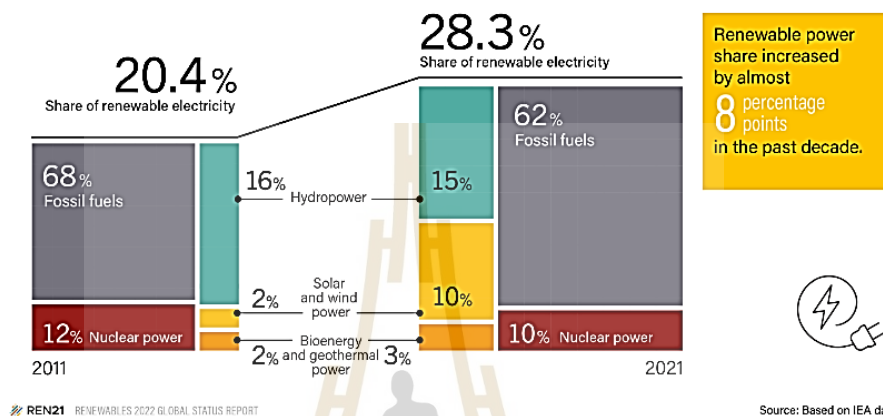


Figure 1.2 Share of renewable energy in power sector in 2011 and 2021 (Secretariat, 2022).

ESS refers to a process of converting electrical energy from power systems into a form that can be stored and converted back to electrical energy (Chen et al., 2009). Energy can be harvested and stored in various forms, such as electrical, thermal, electrochemical, mechanical, and hydrogen-based storages (Figure 1.3) (Taylor, Bolton, Stone, and Upham, 2013). The use of ESS depends on specific requirements related to discharge duration and system size. For example, super capacitors and batteries can be applied in response services, transportation, and distribution due to their high discharging rates and compact module size. Furthermore, the required power can also be delivered by the combination of ESSs, such as battery and ultracapacitor (Aktaş and Kirçiçek, 2021). Our current research is focusing on ESS-based hydrogen and electrochemical methods.

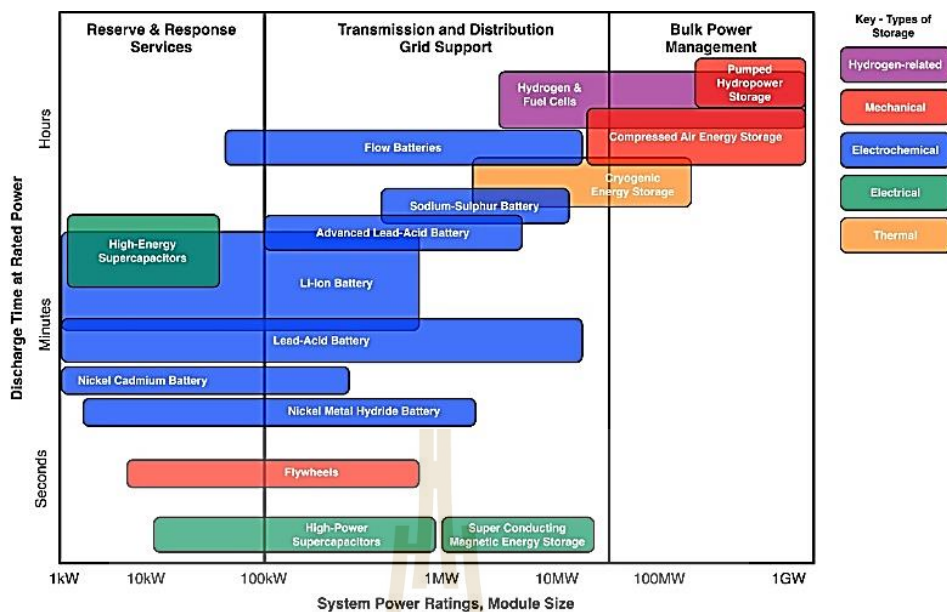


Figure 1.3 Electrical storage technologies and their appropriate applications. Reprinted with permission from Taylor et al., 2013. Copyright 2013 Elsevier Ltd.

1.2 Hydrogen-related energy storages

Among various ESSs, hydrogen storage emerges as a particularly promising technique for long-term energy storage due to its notably high energy density (142 MJ/kg), 2.8 times greater than conventional fossil fuels and its environmentally friendly characteristics (Kumar, Vikrant, Younis, and Kim, 2023). Figure 1.4 shows the anticipated infrastructure for harvesting hydrogen energy, wherein hydrogen is produced through water electrolysis utilizing renewable energy sources (e.g., solar and wind power). This hydrogen is then stored in tanks, ensuring a steady supply of high-purity hydrogen gas for generating electricity via fuel cells (Ren et al., 2023). In the process, hydrogen undergoes oxidation at the anode to yield two protons and two electrons. The protons move through a membrane, while the electrons travel through an external circuit to generate electricity. On the cathode side, the protons and electrons combine with oxygen to create water (Figure 1.5). To achieve the commercial development of hydrogen energy, several key objectives must be addressed, i.e., lowering the cost of hydrogen production, improving the efficiency and safety of hydrogen storage systems, finding an appropriate transportation method for hydrogen, and wide spreading the advance of hydrogen technology.

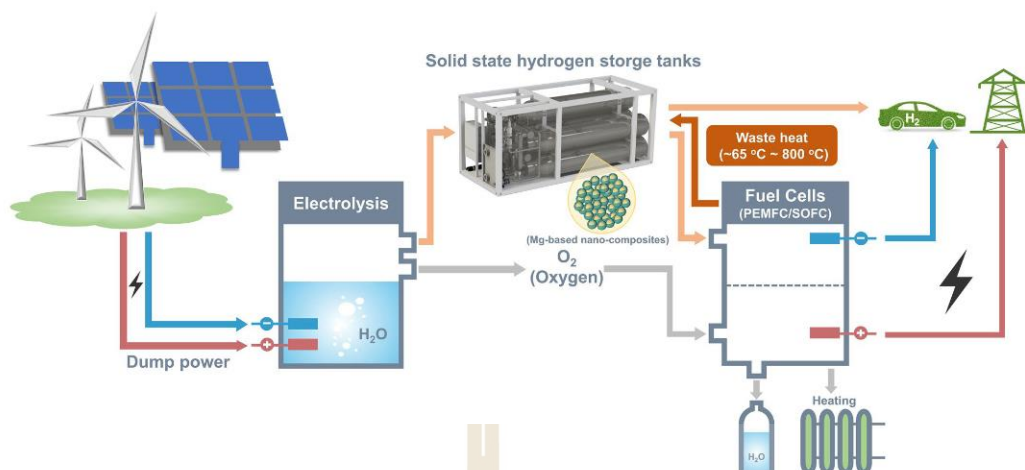


Figure 1.4 The envisioned infrastructure for harvesting hydrogen energy. Reprinted with permission from Ren et al., 2023. Copyright 2023 The Author(s).

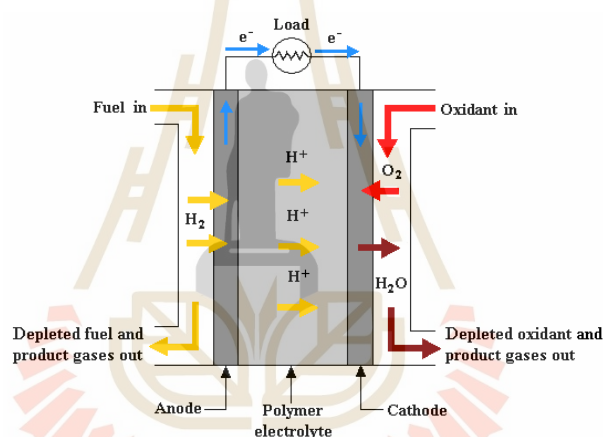


Figure 1.5 A schematic diagram of a proton exchange membrane fuel cell. Reprinted with permission from Wang et al., 2011. Copyright 2010 Elsevier Ltd.

Hydrogen can be stored in three different forms of compressed gas, cryogenic liquid, and solid-state materials (Lee et al., 2022). The only commercialized hydrogen storage technique for mobile applications is the compressed hydrogen tanks, which safety issues due to high pressure are concerned. Moreover, compressed hydrogen storage method does not reach the targets by the US DOE (6.5 wt.% H_2 and 50 g H_2/L , Table 1.1). For examples, storage capacities of compressed gas tank are 4.5 wt.% H_2 and 40 g H_2/L at 700 bar H_2 . For liquefied hydrogen, not only the energy cost for liquefaction at $-253\text{ }^\circ\text{C}$ is high but also there are hydrogen losses due to vaporization at room temperature. Thus, double-walled cylinders with good thermal insulation

systems are required. Alternatively, hydrogen can be stored in solid forms either physisorption in porous materials or chemisorption in hydrides. For physisorption, H₂ is physically bonded with adsorbents via Van der Waals interactions. Highly porous materials, such as metal organic frameworks (MOFs) are of high interest as they can store up to 6 wt.% H₂ and 30 g H₂/L (Wong-Foy, Matzger, and Yaghi, 2006). According to weak Van der Waals interactions, cooling to liquid nitrogen temperature is required (T = -196 °C) to obtain reasonable hydrogen capacity (Panella, Hirscher, Pütter, and Müller, 2006). Chemisorption is when hydrogen is chemically bonded to another element to form hydrides (e.g., NaAlH₄, LiAlH₄, LiBH₄, NaBH₄, and AlH₃). This technique has gained a lot of attention due to its high storage density and remarkable stability. The ideal materials for hydrogen storage are considered to have high hydrogen density, rapid hydrogen uptake and release characteristics, and excellent cyclic stability (Xinglin, Xiaohui, Jiaqi, Quanhui, and Junhu, 2023). In this thesis, solid state hydrogen storage based on hydride materials are focused.

Table 1.1 U.S. Department of Energy targets for onboard hydrogen storage systems for light-duty vehicles (“DOE Technical Targets for Onboard Hydrogen Storage for Light-Duty Vehicles,” n.d.).

Parameters for the hydrogen storage system	Ultimate DOE targets
Gravimetric storage capacity, (wt.% H ₂)	6.5
Volumetric storage capacity (g H ₂ /L)	50
Operating temperature (°C)	-40/60
Cycle life (number of cycles)	1,500
Min/max delivery pressure to FC, (bar)	5-12
Refueling time for 5 kg H ₂ (min)	3-5

1.3 Batteries

Battery is one of various methods to store energy electrochemically. From Figure 1.6(A) and (B), battery consists of anode and cathode, where oxidation and reduction take place, respectively. In commercial Li-ion batteries, graphite often serves as the anode and metal oxide or phosphate, such as LiMO₂ (where M = Co,

Mn, Ni) or LiFePO_4 are the cathode (Nitta, Wu, Lee, and Yushin, 2015). The electrolyte, which are in form of liquid or gel containing appropriate salts or acids, facilitates the flow of ions between anode and cathode (Figure 1.6(A)). During discharge, ions obtained from oxidation at anode move to cathode through electrolyte and external circuit, respectively. The latter converts chemical reaction into electricity. Conversely, electricity transforms into chemical reaction during charging. Ions and electrons are compelled in the opposite direction by an applied current (Hayner, Zhao, and Kung, 2012). Additionally, an electrical insulating separator is required to avoid short circuits due to the direct contact between the electrodes. At the same time, this separator is permeable to ions for charge transfer between the electrodes (Detka and Górecki, 2023).

Solid-state batteries composing of a solid electrolyte, such as crystalline solid, glass, or polymer, do not need liquid electrolytes and separators, leading to a compacted cell design (Figure 1.6(B)). Furthermore, solid-state batteries enable the use of metal anodes and high-voltage cathodes, potentially enhancing the energy density. Recently, rapid advancements have been made in the development of multivalent ion batteries, such as Mg^{2+} , Zn^{2+} , and Al^{3+} due to their high energy densities, the growth of energy storage demand, and limited resource for lithium-ion batteries (Zhan, Zhang, Lei, Liu, and Li, 2020). In this thesis, Mg-based batteries and Mg^{2+} conductors are of significant interest.

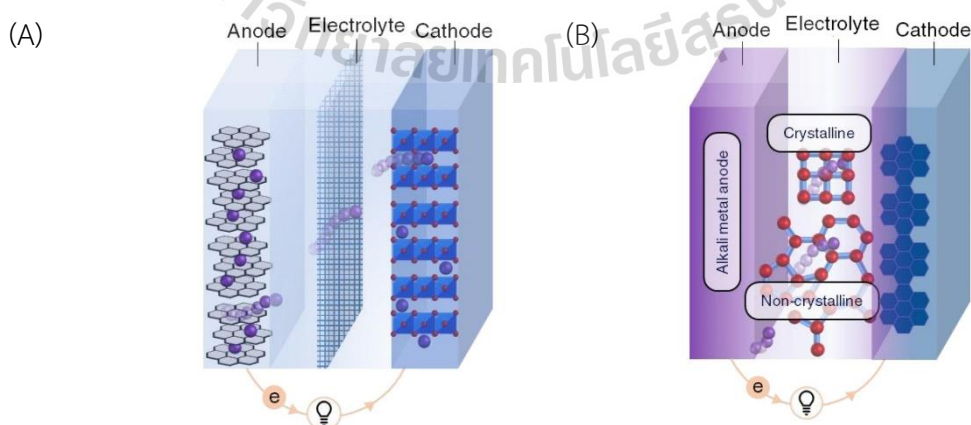


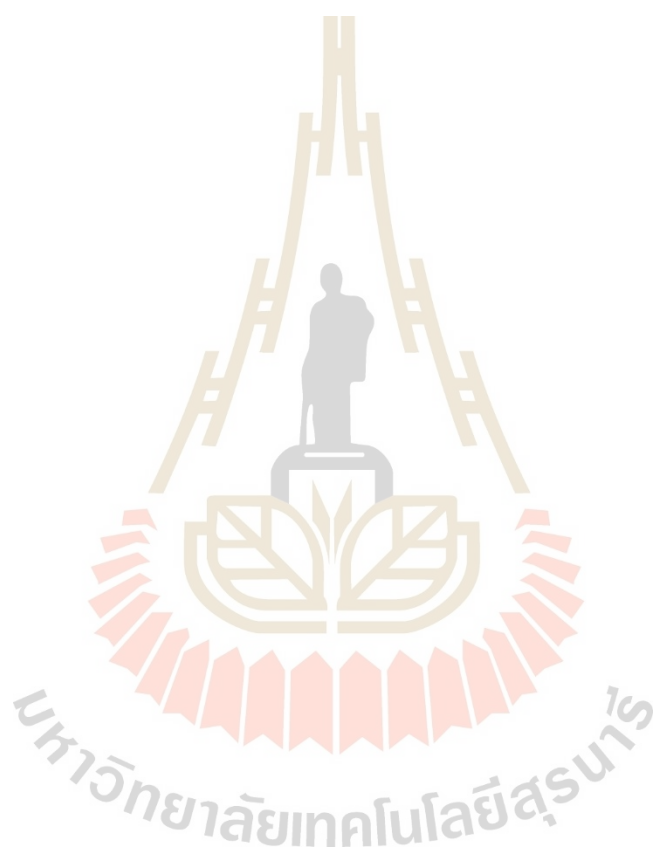
Figure 1.6 A schematic diagram of current ion batteries (A) and conventional solid-state batteries (B). Reprinted with permission from Grady et al., 2020.

1.4 References

- Aktaş, A., and Kirçiçek, Y. (2021). Chapter 7—Hybrid Energy Storage and Innovative Storage Technologies. In A. Aktaş and Y. Kirçiçek (Eds.), *Solar Hybrid Systems* (pp. 139–152). Academic Press. <https://doi.org/10.1016/B978-0-323-88499-0.00007-0>
- Annual CO₂ emissions by world region. (n.d.). Retrieved October 16, 2023, from Our World in Data website: <https://ourworldindata.org/grapher/annual-co-emissions-by-region>
- Chen, H., Cong, T. N., Yang, W., Tan, C., Li, Y., and Ding, Y. (2009). Progress in electrical energy storage system: A critical review. *Progress in Natural Science*, 19(3), 291–312. <https://doi.org/10.1016/j.pnsc.2008.07.014>
- Detka, K., and Górecki, K. (2023). Selected Technologies of Electrochemical Energy Storage—A Review. *Energies*, 16(13), 5034. <https://doi.org/10.3390/en16135034>
- DOE Technical Targets for Onboard Hydrogen Storage for Light-Duty Vehicles. (n.d.). Retrieved October 16, 2023, from Energy.gov website: <https://www.energy.gov/eere/fuelcells/doe-technical-targets-onboard-hydrogen-storage-light-duty-vehicles>
- Grady, Z. A., Wilkinson, C. J., Randall, C. A., and Mauro, J. C. (2020). Emerging Role of Non-crystalline Electrolytes in Solid-State Battery Research. *Frontiers in Energy Research*, 8, 218. <https://doi.org/10.3389/fenrg.2020.00218>
- Greenhouse gases continued to increase rapidly in 2022. (2023, April 5). Retrieved October 16, 2023, from <https://www.noaa.gov/news-release/greenhouse-gases-continued-to-increase-rapidly-in-2022>
- Hayner, C. M., Zhao, X., and Kung, H. H. (2012). Materials for Rechargeable Lithium-Ion Batteries. *Annual Review of Chemical and Biomolecular Engineering*, 3(1), 445–471. <https://doi.org/10.1146/annurev-chembioeng-062011-081024>
- Kumar, A., Vikrant, K., Younis, S. A., and Kim, K.-H. (2023). Tuning of active nickel species in MOF-derived nickel catalysts for the control on acetic acid steam reforming and hydrogen production. *International Journal of Hydrogen Energy*, 48(40), 14964–14977. <https://doi.org/10.1016/j.ijhydene.2023.01.036>

- Lee, S.-Y., Lee, J.-H., Kim, Y.-H., Kim, J.-W., Lee, K.-J., and Park, S.-J. (2022). Recent Progress Using Solid-State Materials for Hydrogen Storage: A Short Review. *Processes*, *10*(2), 304. <https://doi.org/10.3390/pr10020304>
- Nitta, N., Wu, F., Lee, J. T., and Yushin, G. (2015). Li-ion battery materials: Present and future. *Materials Today*, *18*(5), 252–264. <https://doi.org/10.1016/j.mattod.2014.10.040>
- Panella, B., Hirscher, M., Pütter, H., and Müller, U. (2006). Hydrogen Adsorption in Metal–Organic Frameworks: Cu-MOFs and Zn-MOFs Compared. *Advanced Functional Materials*, *16*(4), 520–524. <https://doi.org/10.1002/adfm.200500561>
- Ren, L., Li, Y., Zhang, N., Li, Z., Lin, X., Zhu, W., ... Zou, J. (2023). Nanostructuring of Mg-Based Hydrogen Storage Materials: Recent Advances for Promoting Key Applications. *Nano-Micro Letters*, *15*(1), 93. <https://doi.org/10.1007/s40820-023-01041-5>
- Secretariat, R. (2022, June 15). The Renewables 2022 Global Status Report in 150 words. Retrieved October 16, 2023, from REN21 website: <https://www.ren21.net/the-renewables-2022-global-status-report-in-150-words/>
- Taylor, P. G., Bolton, R., Stone, D., and Upham, P. (2013). Developing pathways for energy storage in the UK using a coevolutionary framework. *Energy Policy*, *63*, 230–243. <https://doi.org/10.1016/j.enpol.2013.08.070>
- Wang, Y., Chen, K. S., Mishler, J., Cho, S. C., and Adroher, X. C. (2011). A review of polymer electrolyte membrane fuel cells: Technology, applications, and needs on fundamental research. *Applied Energy*, *88*(4), 981–1007. <https://doi.org/10.1016/j.apenergy.2010.09.030>
- Wong-Foy, A. G., Matzger, A. J., and Yaghi, O. M. (2006). Exceptional H₂ Saturation Uptake in Microporous Metal–Organic Frameworks. *Journal of the American Chemical Society*, *128*(11), 3494–3495. <https://doi.org/10.1021/ja058213h>
- Xinglin, Y., Xiaohui, L., Jiaqi, Z., Quanhui, H., and Junhu, Z. (2023). Progress in improving hydrogen storage properties of Mg-based materials. *Materials Today Advances*, *19*, 100387. <https://doi.org/10.1016/j.mtadv.2023.100387>

Zhan, Y., Zhang, W., Lei, B., Liu, H., and Li, W. (2020). Recent Development of Mg Ion Solid Electrolyte. *Frontiers in Chemistry*, 8, 125. <https://doi.org/10.3389/fchem.2020.00125>



CHAPTER II

LITERATURE REVIEWS

In this chapter, the fundamental principles and types of solid-state hydrides, especially Mg-based hydrides, for hydrogen storage and solid-state batteries will be discussed.

2.1 Fundamental principle of solid-state hydrides for hydrogen storage

As the demand for clean and sustainable energy sources continues to rise, hydrogen is gaining significant attention due to its potential as a versatile and eco-friendly fuel. However, the efficient and safe storage of hydrogen remains a critical barrier for its widespread implementation. Solid-state hydrogen storage materials offer an innovative approach to overcome these challenges as well as to provide enhanced safety, improved storage capacity, and greater ease of handling as compared to traditional storage methods.

To assess the hydrogen storage properties of materials, the Pressure-Composition-Isotherm (PCI) curve is considered (Figure 2.1(B)). The investigation involves measuring the hydrogen absorption behavior under increasing hydrogen pressure at a specific temperature. As the hydrogen pressure rises, represented by a slope on the left side of the plateau, the hydrogen concentration (C_H) also increases until reaching the plateau pressure. At low hydrogen concentration, hydrogen atoms participate into the sublattice of the metal/alloy, forming a solid solution phase (α -phase) (Figure 2.1(A)). As the hydrogen pressure continues to increase, the formation of the hydride phase (β -phase) is initiated. In the plateau region, hydrogen concentration continues to rise, causing the saturated α -phase to β -phase with an increase in concentration (Figure 2.1(C)) (Z. Chen et al., 2021). The Gibbs free energy depends on temperature, represented by the following equations, called Van't Hoff equations (Dornheim, 2011).

$$\Delta G = \frac{1}{2} RT \ln \left(\frac{P_T}{P_0} \right) \quad (2.1)$$

$$\frac{1}{2} \ln \left(\frac{P_T}{P_0} \right) = \frac{\Delta H}{RT} - \frac{\Delta S}{R} \quad (2.2)$$

Where P_T is the plateau pressure, P_0 is the standard pressure, R is the gas constant, T is the temperature, ΔH and ΔS are the enthalpy and entropy changes, respectively.

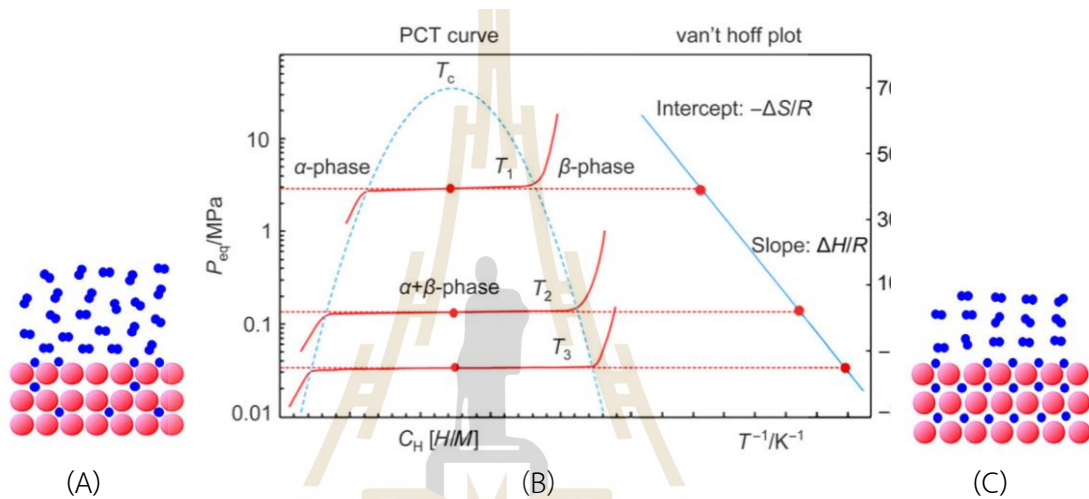


Figure 2.1 Schematic illustration of solid solution phase (α -phase) (A), Pressure-Composition-Isotherm (PCI) and the deduced Van't Hoff plot (B), and hydride phase (β -phase) (C). Reprinted with permission from Chen et al., 2021. Copyright 2020 The Chemical Industry and Engineering Society of China, and Chemical Industry Press Co., Ltd.

Moreover, the temperature-dependent plateau pressure serves as the equilibrium dissociation pressure of the hydride (β -phase), indicating the stability of hydride (Dornheim, 2011; Züttel, 2003). In simpler terms, raising the plateau pressure at a given temperature can reduce the thermodynamic stability of the hydride. Additionally, the width of the plateau region determines the maximum quantity of reversible hydrogen capacities of hydride materials. Many systems exhibit hysteresis in their absorption and desorption processes, indicating that a higher H_2 pressure is required for absorption than for desorption. Ideally, hydrides should exhibit formation/decomposition characteristics at atmospheric temperature and pressure for practical applications.

Nevertheless, only a limited number of systems possess these desirable properties. Some AB_5 compounds, e.g., $LaNi_5$, $MmNi_5$, and $TiFe$, can be employed under ambient conditions but they still suffer from low hydrogen capacities.

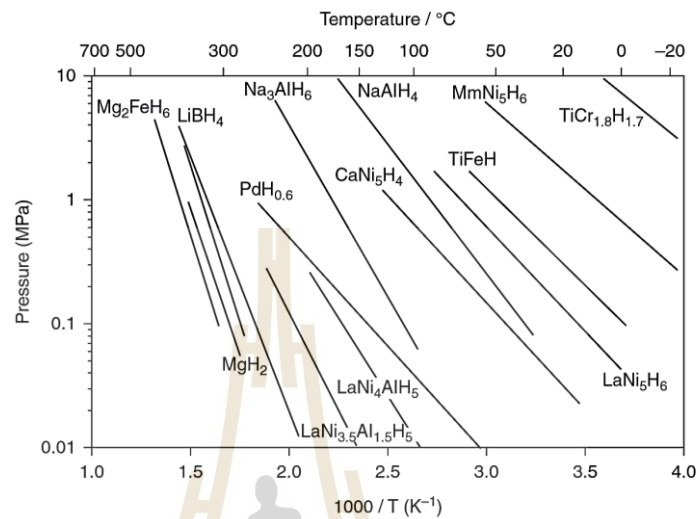


Figure 2.2 Van't Hoff plot of various hydride materials. Reprinted with permission from Millet, 2014. Copyright 2014 Elsevier Ltd.

2.2 Solid-state hydrogen storage materials

Solid-state hydrides can be classified into two groups based on the nature of chemical bonding, including interstitial hydrides and non-interstitial hydrides. Hydrogen forms a metallic bond with metal atoms by occupying the interstitial spaces in the tetrahedral and/or octahedral sites within the sublattice of interstitial hydrides. On the other hand, in non-interstitial hydrides, hydrogen establishes covalent and/or ionic bonds with adjacent elements (Figure 2.3).

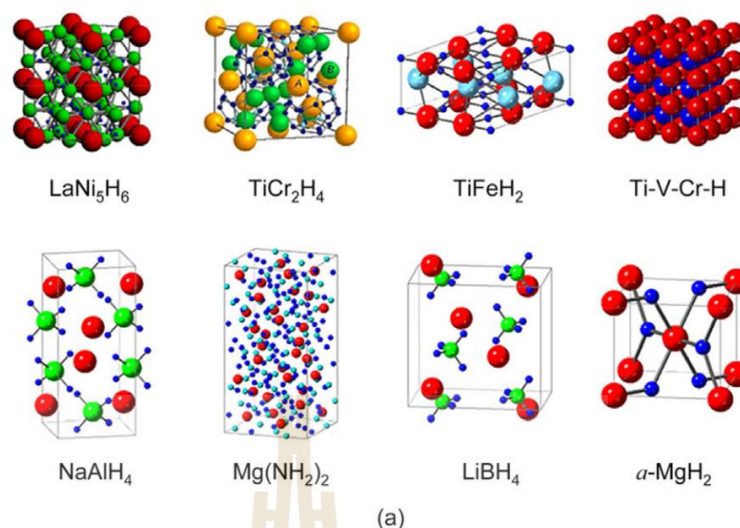


Figure 2.3 Interstitial hydrides (upper) and non-interstitial hydrides (bottom). Reprinted with permission from Chen et al., 2021. Copyright 2020 The Chemical Industry and Engineering Society of China, and Chemical Industry Press Co., Ltd.

Interstitial hydrides primarily consisting of transition metals (e.g., LaNi_5H_6 , TiCr_2H_4 , TiFeH_2 , and Ti-V-Cr-H) have lower hydrogen capacities than non-interstitial hydrides predominantly composed of light elements (e.g., NaAlH_4 , $\text{Mg}(\text{NH}_2)_2$, LiBH_4 , and Ti-V-Cr-H). Conversely, the metallic bond present in interstitial hydrides is notably weaker than the covalent and/or ionic bonds in non-interstitial hydrides. This leads to a lower temperature required for hydrogen release from interstitial hydrides. Furthermore, the hydrogen absorption and desorption in interstitial hydrides are influenced by dissociation and recombination of hydrogen atoms on the metal surface along with diffusion within the metal bulk of hydrogen atoms. In this case, the metallic structure undergoes minimal change (Figure 2.4(A)). On the contrary, the hydrogen desorption in non-interstitial hydrides involves the decomposition of the hydrides, and hydrogen absorption occurs through the recombination of the decomposed product (Figure 2.4(B)). The difference in characteristics between interstitial and non-interstitial hydrides results in distinctive operational conditions, such as temperature and pressure requirements, as well as diverse applications. Specifically, interstitial hydrides demonstrate promise for stationary applications, presenting lower reaction

temperatures, faster reaction kinetics, and superior cycling behavior when compared to non-interstitial hydrides. Conversely, for mobile applications, non-interstitial hydrides are better suited due to their elevated storage capacity, despite needing higher reaction temperatures and exhibiting slower kinetics. The following content extends significant insights into hydrogen storage materials for both interstitial and non-interstitial hydrides. In this thesis, the non-interstitial hydrides are of interest.

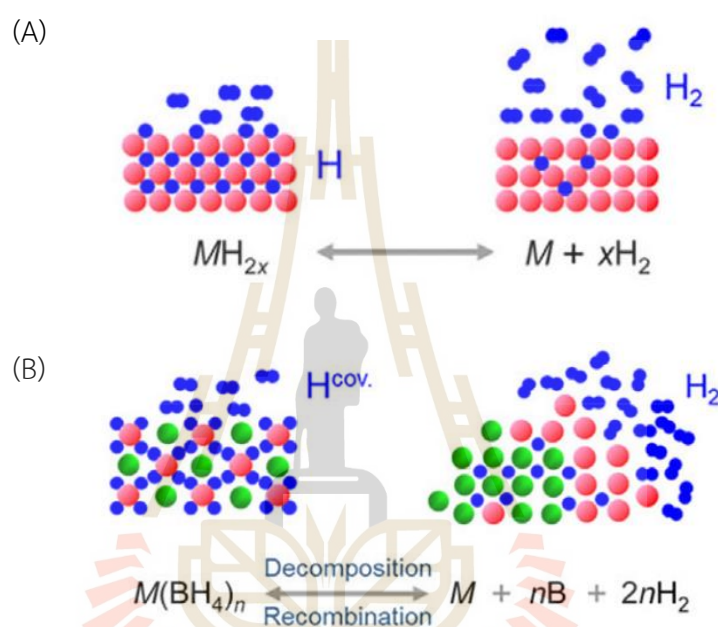


Figure 2.4 The reaction mechanisms of interstitial (A) and non-interstitial (B) hydrides. Reprinted with permission from Chen et al., 2021. Copyright 2020 The Chemical Industry and Engineering Society of China, and Chemical Industry Press Co., Ltd.

Non-interstitial hydrides include various material groups, including complex hydrides e.g., metal alanates ($M(AlH_4)_n$), metal amides ($M(NH_2)_n$), metal borohydrides ($M(BH_4)_n$), as well as Mg-based hydrides (Table 2.1). A significant characteristic of non-interstitial hydrides is their compositions primarily involving light elements, with high hydrogen capacities exceeding 5 wt.%. Non-interstitial hydrides are thus anticipated to serve as high-density hydrogen storage materials, prompting extensive research efforts in this area.

Table 2.1 Examples of non-interstitial hydrides. Reprinted (Adapted) with permission from Chen et al., 2021. Copyright 2020 The Chemical Industry and Engineering Society of China, and Chemical Industry Press Co., Ltd.

Type	Hydride	ρ_m /wt.%	ρ_v /kg·m ⁻³	ΔH /kJ·mol ⁻¹
Alanate	$3\text{NaAlH}_4 \rightarrow \text{Na}_3\text{AlH}_6 + 2\text{Al} + 3\text{H}_2$	3.7	48	-37
Amide	$\text{Mg}(\text{NH}_2)_2 + 2\text{LiH} \rightarrow \text{Li}_2\text{Mg}(\text{NH})_2 + 2\text{H}_2$	6.5	68	-45.5
	$\text{LiNH}_2 + \text{LiH} \rightarrow \text{Li}_2\text{NH} + \text{H}_2$	5.5	66	-46.1
Borohydride	$\text{LiBH}_4 \rightarrow \text{LiH} + \text{B} + 3/2\text{H}_2$	13.9	91	-74
	$\text{Mg}(\text{BH}_4)_2 \rightarrow \text{MgH}_2 + 2\text{B} + 3\text{H}_2$	11.1	110	-57
	$2\text{LiBH}_4 + \text{MgH}_2 \rightarrow 2\text{LiH} + \text{MgB}_2 + 4\text{H}_2$	11.5	96	-40.5
Mg-based hydride	$\text{MgH}_2 \rightarrow \text{Mg} + \text{H}_2$	7.6	109	-75.3
	$\text{Mg}_2\text{NiH}_4 \rightarrow \text{Mg}_2\text{Ni} + 2\text{H}_2$	3.6	97	-64

2.2.1 Metal alanates

Among various several metal alanates, for example LiAlH_4 , KAlH_4 , $\text{Mg}(\text{AlH}_4)_2$, $\text{Ca}(\text{AlH}_4)_2$, and $\text{Y}(\text{AlH}_4)_3$, NaAlH_4 represents a significant class of complex hydride with the potential for hydrogen storage. This material releases 5.5 wt.% H_2 through two steps via an intermediate phase of Na_3AlH_6 at 483 - 523 K. Despite initial challenges of irreversibility under moderate conditions, the introduction of Ti-based catalysts marked a crucial advancement of achieving reversible hydrogen storage in NaAlH_4 (Borislav Bogdanović and Schwickardi, 1997). Further research has expanded to include not only Ti-based catalysts but also more advantageous Sc- or Ce-based catalysts, particularly at lower hydrogenation pressures (B. Bogdanović, Felderhoff, Pommerin, Schüth, and Spielkamp, 2006). The practical application of Ti-doped NaAlH_4 has demonstrated a substantial reversible hydrogen storage capacities (3.5–4 wt.%) (Srinivasan, Brinks, Hauback, Sun, and Jensen, 2004).

2.2.2 Metal amides

Metal amides ($M(\text{NH}_2)_n$, where M^{n+} is primarily derived from alkali and alkaline-earth metals do not effectively liberate hydrogen, but rather release ammonia gas, poisoning for fuel cells. $\text{LiNH}_2\text{-LiH}$ composite was initially reported for hydrogen storage material in 2002 with a significant release of hydrogen up to 10.4 wt.%. (P. Chen, Xiong, Luo, Lin, and Tan, 2002). Modifying the chemical composition is identified as a viable strategy to adjust thermodynamics of this amide-hydride system. Moreover, $\text{Mg}(\text{NH}_2)_2\text{-2LiH}$ composite exhibits relatively high reversible hydrogen capacity of 5.6 wt.% at around 423 K. Additionally, the three-component system of $2\text{Mg}(\text{NH}_2)_2\text{-3LiH-4LiBH}_4$ displayed reversible capacity up to 6 wt.% H_2 at $T < 373$ K (H. Wang et al., 2017). Extensive efforts have been dedicated to enhancing dehydrogenation/rehydrogenation kinetics based on the interface reactions, nucleation/nuclei growth, and diffusion processes in solid–solid reactions. A notable improvement was achieved by introducing a small amount of KH to the $\text{Mg}(\text{NH}_2)_2\text{-2LiH}$, weakening both the amide N-H and imide Li-N bonds (J. Wang et al., 2009).

2.2.3 Metal borohydrides

Metal borohydrides ($M(\text{BH}_4)_n$) consist of a metal cation M^{n+} and $[\text{BH}_4]^-$. Various metal borohydrides, e.g., LiBH_4 , $\text{Mg}(\text{BH}_4)_2$, and $\text{Ca}(\text{BH}_4)_2$, are known for their high hydrogen capacities (>10 wt.%). They have been extensively studied as potential candidates for onboard hydrogen storage (H.-W. Li, Yan, Orimo, Züttel, and Jensen, 2011). The dehydrogenation process of $M(\text{BH}_4)_n$ is more complicated with respect to alanates and amides. For example, LiBH_4 releases approximately 18 wt.% H_2 through multiple steps accompanied with the formation of intermediate compounds, such as B_2H_6 , BH_3 , and $\text{Li}_2\text{B}_{12}\text{H}_{12}$ (Yan et al., 2012). The presence of $[\text{B}_{12}\text{H}_{12}]^{2-}$ has been widely considered as a major factor, causing rehydrogenation degradation because rehydrogenation of $[\text{B}_{12}\text{H}_{12}]^{2-}$ into $[\text{BH}_4]^-$ required high temperatures to break the strong B-B bond (Paskevicius et al., 2017). To mitigate the formation of $[\text{B}_{12}\text{H}_{12}]^{2-}$, two approaches are employed. The first one is reducing dehydrogenation temperature to generate smaller anions e.g., $[\text{B}_3\text{H}_8]^{2-}$ (Chong, Matsuo, Orimo, Autrey, and Jensen, 2015; Grinderslev et al., 2019). The second one is creating composites to alter the

dehydrogenation process, for example, by the well-known $\text{LiBH}_4\text{-MgH}_2$ system (Figure 2.5).

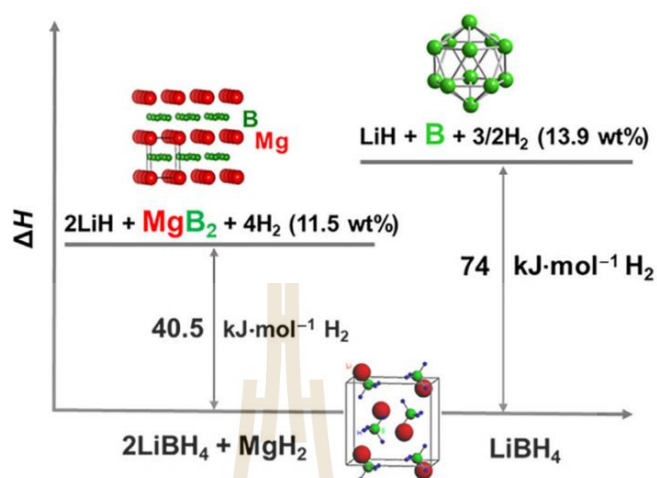


Figure 2.5 Dehydrogenation enthalpies of $2\text{LiBH}_4 + \text{MgH}_2$ composite and the single phase of LiBH_4 . Reprinted with permission from Chen et al., 2021. Copyright 2020 The Chemical Industry and Engineering Society of China, and Chemical Industry Press Co., Ltd.

In the single-phase form, LiBH_4 releases 13.9 wt.% of hydrogen upon heating to 873 K, with a dehydrogenation enthalpy of $74 \text{ kJ}\cdot\text{mol}^{-1} \text{ H}_2$. However, the dehydrogenation enthalpy is reduced to $40.5 \text{ kJ}\cdot\text{mol}^{-1} \text{ H}_2$ in the $2\text{LiBH}_4 + \text{MgH}_2$ composite. The dehydrogenation product of MgB_2 led to the reduced thermodynamics and remarkable reversibility at 673 K as well as high gravimetric and volumetric hydrogen capacities (11.4 wt.% H_2 and $94.7 \text{ gH}_2/\text{L}$, respectively) (Ulrike Bösenberg et al., 2007; Vajo, Skeith, and Mertens, 2005). However, the process faces challenges due to slow kinetics and long incubation periods for MgB_2 formation, leading to over 18 h to complete dehydrogenation at $400 \text{ }^\circ\text{C}$ (Ulrike Bösenberg et al., 2007; Zhong, Kang, Wang, and Wang, 2014).

To overcome these challenges, numerous strategies have been explored, including catalytic and additive doping, particle size reduction via mechanical milling, and confinement into inert porous materials. Various substances, such as metals (Pd, Al, Fe), compounds (Ti-isopropoxide, Nb_2O_5 , Nb_2O_5 , Pd, Ti-isopropoxide, Al, TiCl_3 , HfCl_4 , ZrCl_4 , VCl_3 , MoCl_3 , Fe, NbC, and NbF_5) (U. Bösenberg et al., 2010; Deprez et al., 2010; Fan et al., 2008; Fernández, Deprez, and Friedrichs, 2011; Y. Li, Izuhara, and Takeshita,

2011; Puzkiel et al., 2015; Sridechprasat, Suttisawat, Rangsunvigit, Kitiyanan, and Kulprathipanja, 2011; Weng et al., 2010; Zhou et al., 2017), carbon materials (activated carbon, SWNTs) (Cho et al., 2016; K. Wang, Kang, Luo, Hu, and Wang, 2013; P.-J. Wang, Fang, Ma, Kang, and Wang, 2008), and combinations of transition metal-based catalysts and carbon materials (Ru nanoparticles on MWCNTs and Ni nanoparticles on $g\text{-C}_3\text{N}_4$ (Huang et al., 2018; Mao, Guo, Yu, and Liu, 2011)), have been introduced to $2\text{LiBH}_4\text{-MgH}_2$ to improve kinetics and reversibility. For instance, doping with 5 wt.% Ti-isopropoxide reduced incubation periods and enhanced dehydrogenation (Ulrike Bösenberg et al., 2007). TiB_2 formed during dehydrogenation migrated to the $\text{LiBH}_4\text{-Mg}$ interface and acted as nucleation sites for MgB_2 formation (Fernández et al., 2011). Carbon material doping not only improved thermal conductivity and hydrogen diffusion but also prevented particle agglomeration, consequently enhancing dehydrogenation kinetics and reversibility (Chaise et al., 2009; Plerdsranoy, Chanthee, and Utke, 2017; Sitthiwet et al., 2017). Nanoparticle-based catalytic strategies, such as $2\text{LiBH}_4\text{-MgH}_2$ doped with Ni nanoparticles on $g\text{-C}_3\text{N}_4$, displayed accelerated kinetics and eliminated the incubation period of MgB_2 formation (Huang et al., 2018; Mao et al., 2011). Nanoscaling methods using ball milling increased the reactive surface area but faced challenges of particle agglomeration upon cycling, degrading sorption kinetics and reversibility (Nielsen et al., 2010). The concept of nanoconfinement within nanoporous structures of TiO_2 , SiO_2 , carbon, and polymers has emerged to prevent particle growth, promote dispersion, and provide high active surface, thereby improving sorption kinetics and reversibility. The study of nanoconfined samples has predominantly occurred in laboratory settings (Gosalawit-Utke et al., 2014, 2013; L. Guo et al., 2013; Jia and Yao, 2017; Ngene, Adelhelm, Beale, de Jong, and de Jongh, 2010; Plerdsranoy et al., 2015; Surrey et al., 2016; Wahab, Jia, Yang, Zhao, and Yao, 2013; L. Wang, Rawal, Quadir, and Aguey-Zinsou, 2017; Yan Zhao et al., 2017; Yanping Zhao et al., 2014). With regards to this, the evaluation of the de/rehydrogenation characteristics of nanoconfined $2\text{LiBH}_4\text{-MgH}_2$ within activated carbon (AC) in a small hydrogen storage tank is proposed for the first time. The results and discussions will be presented in Chapter IV, Section 4.1.1.

2.2.4 Mg-based hydrides

MgH₂ stands out as a highly promising candidate for hydrogen storages and displays notable gravimetric and volumetric capacities (7.6 wt.% H₂ and 110 g H₂/L, respectively). Mg is the earth's second most abundant element, and it is economically friendly (priced at \$3/kg for Mg) (Yang et al., 2023) (Yartys et al., 2019). However, its practical applications face challenges attributed to its considerable thermodynamic stability ($\Delta H = 70\text{-}75$ kJ/mol H₂) (Paskevicius, Sheppard, and Buckley, 2010; Shao, Wang, Xu, and Li, 2004; Vigeholm, Kj ller, Larsen, and Pedersen, 1983) and sluggish sorption kinetics ($E_A = 160$ kJ/mol (Crivello et al., 2016; Peng, Liang, Tao, and Chen, 2009)). Various strategies have been explored to address these limitations, including doping with catalysts and additives. These methods involve (i) incorporating transition metals and alloys, such as Fe, Co, Ni, V nanosheets, TiMn₂, and Ti-Cr-Mn-Fe-V (M.S. EL-Eskandarany et al., 2017; Gattia, Jangir, and Jain, 2019; Haghparast and Rajabi, 2015; Hanada, Ichikawa, and Fujii, 2005; Lu et al., 2021; Song, Kwon, Park, and Hong, 2011; Xie et al., 2009), (ii) utilizing oxides, halides, and halides such as Nb₂O₅, TiO₂, CeO₂, ZrCl₄, TiF₄, and MnCl₂ (Gattia et al., 2019; Jangir et al., 2016; Kim et al., 2008; Mustafa and Ismail, 2017; Nielsen and Jensen, 2012; Pukazhselvan et al., 2017; Rangsunvigit, Sridechprasat, Kitiyanan, and Kulprathipanja, 2014; Sherif EL-Eskandarany et al., 2018; Sun et al., 2020; Yahya and Ismail, 2019; J. Zhang et al., 2018; X. Zhang et al., 2018), and (iii) combining transition metal catalysts with carbon (Ni₃Fe/reduced graphene oxide) (Liu et al., 2020). Transition metals have displayed catalytic effects, aiding in the dissociation and recombination of hydrogen during de/rehydrogenation, while transition metal halides and oxides have shown favorable impacts on kinetics by promoting the creation of new active phases (Pukazhselvan et al., 2017; Xie et al., 2009; J. Zhang et al., 2018).

Expanding the scope of experimental research on MgH₂-based storage materials in the tank scale involves the considerations beyond de/rehydrogenation kinetics. It includes considerations of thermal conductivity, hydrogen diffusion, and effective heat management within the hydride beds (Garrier et al., 2011; Thiangviriya et al., 2019). The enhancement of thermal conductivity in MgH₂-based tanks has been achieved through compaction and the incorporation of thermally conductive materials, such as

expanded natural graphite (ENG) (Chaise, de Rango, Marty, and Fruchart, 2010; Chaise et al., 2009) and metal powder like aluminum (Capurso et al., 2011). Strategies involving the combination of transition metal catalysts with carbon materials (Ti-V-Cr-ENG (Delhomme et al., 2013; Garrier et al., 2011), TiH₂-graphite (Nyallang Nyamsi et al., 2021), and TiF₄-MWCNTs (Thiangviriyā et al., 2019)) have been implemented to simultaneously improve kinetics and thermal conductivity at the tank scale. Furthermore, the use of carbon materials, such as graphite and MWCNTs has been effective in preventing grain growth in MgH₂ during cycling, maintaining a consistent hydrogen diffusion rate within the hydride beds (Lotoskyy et al., 2018; Ouyang et al., 2013). In addition to the utilization of these additives, the integration of heat pipes (Chung, Yang, Yang, Hsu, and Chiu, 2013) and diverse heat exchanger designs (including double tubes (Garrier et al., 2011; Thiangviriyā et al., 2019), central cooling tubes coupled with copper fins (Chaise et al., 2010; Garrier et al., 2011), and perforated copper fins (Nyallang Nyamsi et al., 2021)) has been explored to optimize heat management during the de/rehydrogenation process in MgH₂-based tanks. Another critical consideration for the practical application of hydrogen storage tanks involves ensuring a consistent mass flow rate of hydrogen supply over an extended period to achieve the most efficient electrical output from fuel cells (M. Sherif El-Eskandarany, Al-Nasrallah, Banyan, and Al-Ajmi, 2018).

In our earlier research, a cylindrical hydrogen storage tank (with a packing volume of 96.2 mL) tailored with a central tube heat exchanger and loaded with approximately 45 g of MgH₂ doped with TiF₄ and MWCNTs (Figure 2.6(A)) exhibited exceptional de/rehydrogenation kinetics and reversibility, i.e., 5.40 wt.% H₂ after 20 cycles at 250-300 °C at under 15 bar H₂ (Figure 2.6(B)). Subsequent investigations involved coupling this MgH₂-based tank with a polymer electrolyte membrane fuel cell (PEMFC) stack. By maintaining a constant hydrogen mass flow rate of 0.1 SLM from the MgH₂-based tank to the PEMFC stack, a sustained electrical power output of 5.6 W was maintained for 3 h. However, only 57.4% of the hydrogen capacity (3.10 wt.% H₂) was utilized for electrical power generation, possibly due to inadequate dehydrogenation kinetics arising from the mismatched temperature and hydrogen mass flow rates employed during the experiments (Thiangviriyā et al., 2019).

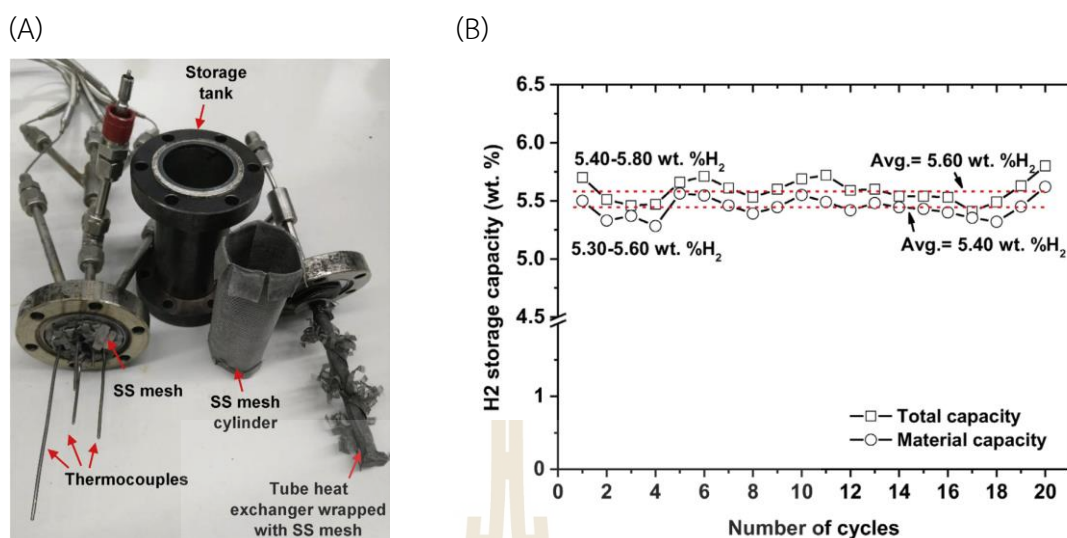


Figure 2.6 The components (A) and cycling performance (B) of MgH₂-TiF₄-MWCNTs tank. Reprinted with permission from Thiangviriyaa et al., 2019. Copyright 2019 Hydrogen Energy Publications LLC. Published by Elsevier Ltd.

In this present study, we aim to explore how operating temperatures and hydrogen mass flow rates (H₂-FR) impact the kinetic properties and behaviors of MgH₂-based tanks. The dehydrogenation performance of the MgH₂-based tank (operating temperatures ranging from 300 to 340 °C under H₂-FR of 0.6 to 1.0 SLM) is being assessed using temperature and pressure sensors as well as a mass flow controller. Additionally, the dehydrogenation characteristics in both the axial and radial directions within the tank are examined. The kinetic behaviors of MgH₂-based materials at both laboratory and tank scales using solid-gas kinetic models are also evaluated. The results and discussions will be presented in Chapter IV, Section 4.1.2.

2.3 Mg-based solid-state batteries

Another application of hydride materials is to be used as an ionic conductor in solid-state batteries (SSBs), where the convenient liquid electrolytes and membrane is replaced by solid ion conductors (Figure 1.6 in Chapter I). To drive the required redox reaction and facilitate the flow of electrons through the external circuit, the ideal electrolyte must possess high ionic conductivity ($\sigma_{\text{ion}} > 10^{-3}$ S/cm) and negligible electronic conductivity ($\sigma_{\text{electron}} < 10^{-12}$ S/cm) (Grady, Wilkinson, Randall, and Mauro,

2020). The well-known lithium-ion battery has lately faced limited advancements for the improvement of energy density and safety. Furthermore, this technology is based on several critical raw materials, which may become limited in the near future. As an alternative, significant research efforts within utilization of multivalent metals such as Mg^{2+} , Zn^{2+} , and Al^{3+} are on-going (Zhan, Zhang, Lei, Liu, and Li, 2020). Among them, magnesium is considered a promising anode material for the next-generation batteries due to its high volumetric energy density (3833 mAh cm^{-3}), high elemental abundance, low cost, and a large negative potential (-2.4 V vs. SHE). Unfortunately, divalent metals such as Mg^{2+} often have slow ionic migration through solid materials (Jaschin, Gao, Li, and Bo, 2020; Patel et al., 2023; Zhan et al., 2020). Several materials has been proposed as Mg-ion conductors, such as oxides (particularly phosphates), metal–organic frameworks (MOFs), chalcogenides, polymers, and hydrides (M. Guo, Yuan, Zhang, and Yu, 2022).

2.3.1 Oxides

The first-generation oxide as solid-state electrolytes (SSEs) for magnesium-ion batteries (MIBs) is the ceramic-oxides with general formular $A_xM_y(XO_4)_3$. These oxides possess two different three-dimensional (3D) structures of β - $Fe_2(SO_4)_3$ -type and sodium-super-ionic-conductor (NASICON)-type (Figure 2.7). Ther are suitable for Mg^{2+} ion transport (M. Guo et al., 2022). Nevertheless, the monoclinic symmetry of NASICON with higher symmetry and larger channel size ranging from 4.5 to 4.7 Å, facilitates efficient ion migration, leading to high ionic conductivity. The NASICON-type structure of $Mg_{0.5}Zr_2(PO_4)_3$ (MZP) demonstrates notable ionic conductivities at elevated temperatures up to 2.9×10^{-5} and $6.1 \times 10^{-3} \text{ S cm}^{-1}$ at 400 °C and 800 °C, respectively (Ikeda, Takahashi, Ishikawa, and Ito, 1987).

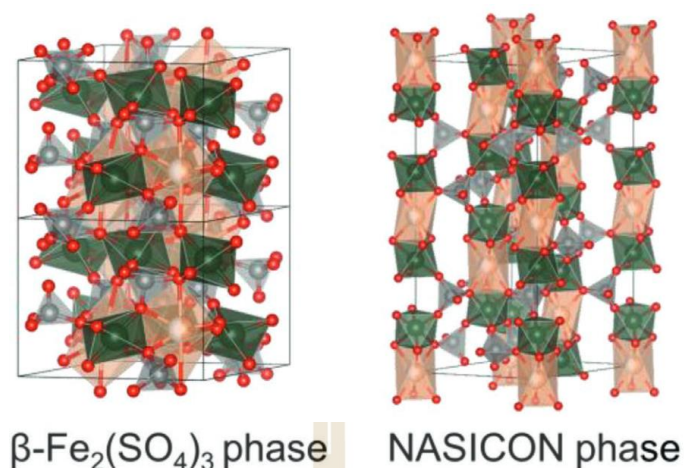


Figure 2.7 Crystal structure of $\beta\text{-Fe}_2(\text{SO}_4)_3$ -type and NASICON-type of $\text{A}_x\text{M}_y(\text{XO}_4)_3$. Reprinted with permission from Guo et al., 2022. Copyright 2022 Wiley-VCH GmbH.

Besides phosphate-based oxides, other oxide electrolytes have been investigated. The composite of 30% MgI_2 –70% $\text{Mg}_3(\text{PO}_4)_2$ showed high conductivity of $7.0 \times 10^{-4} \text{ S cm}^{-1}$ at room temperature (Ahmad and Ghani, 2009). $\text{Mg}(\text{NO}_3)_2$ - $x\text{Al}_2\text{O}_3$ and $\text{Mg}(\text{NO}_3)_2$ - $x\text{MgO}$ composites revealed high Mg^{2+} conductivities of 4×10^{-4} and $10^{-6} \text{ S cm}^{-1}$, respectively, at room temperature (M. Sulaiman, Che Su, and Mohamed, 2017; Mazdida Sulaiman, Rahman, and Mohamed, 2013). The enhanced conductivity is likely due to the weakened strength in the Mg–O bonds, leading to an increase in the Mg^{2+} ion conduction path (M. Guo et al., 2022). Despite making progress, several challenges of the necessity for high-temperature synthesis techniques and the limited conductivity observed at moderate temperatures remain. There has been an ongoing emphasis on enhancing preparation processes, conductivity, and exploring alternative materials capable of effective operation at lower temperatures for practical applications.

2.3.2 Metal–organic frameworks (MOFs)

Metal-organic frameworks (MOFs) have attracted considerable attention due to their high specific surface area and outstanding adjustability in pore dimension without impacting the fundamental network structure. Capability for single-ion conductivity makes them promising candidates for SSEs, particularly in facilitating the transport of multivalent ions like Mg^{2+} and Al^{3+} (R. Zhao et al., 2020). Expanding the pore size results in a reduction in the polarity of the MOF surface due to the presence of a larger organic

linker. Hence, the Mg^{2+} ionic conductivity was significantly increased to 0.25 mS cm^{-1} (Aubrey, Ameloot, Wiers, and Long, 2014). Mg^{2+} -loaded Cu(II)-azolate MOF with tubular pores demonstrated noteworthy ionic conductivity of $8.8 \times 10^{-7} \text{ S cm}^{-1}$ at room temperature (S. S. Park, Tulchinsky, and Dincă, 2017). The host MOF, $\text{Cu}_4(\text{ttpm})_2$ (H_4ttpm = tetrakis(4-tetrazolylphenyl)methane) (Figure 2.8), was found to significantly accelerate Mg^{2+} ionic conductivity due to its multiple binding sites for capturing anions. This resulted in a high density of independent cations, significantly enhancing conductivity (Dincă, Dailly, and Long, 2008). In the case of $\text{Cu}_4(\text{ttpm})_2 \cdot 0.6\text{CuCl}_2$ as a solid-state electrolyte, bromide salts exhibited higher Mg^{2+} ionic conductivity ($1.3 \times 10^{-4} \text{ S cm}^{-1}$) than chlorides at room temperature (Miner, Park, and Dincă, 2019).

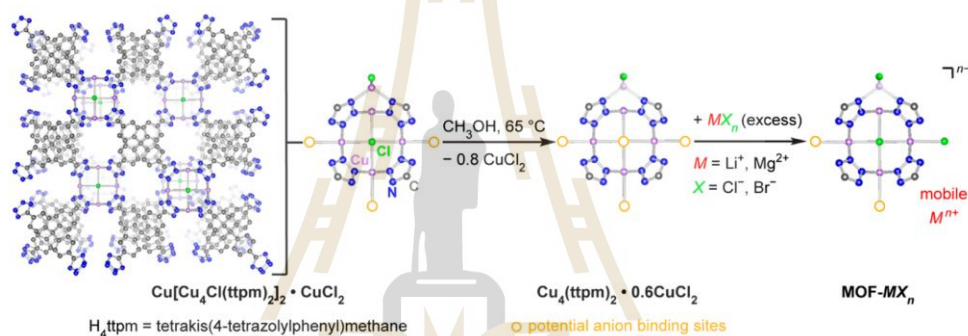


Figure 2.8 Synthesis procedure of $\text{Cu}[(\text{Cu}_4\text{Cl})(\text{ttpm})_2]_2 \cdot \text{CuCl}_2$, $\text{Cu}_4(\text{ttpm})_2 \cdot 0.6\text{CuCl}_2$, and the Target MOF-MX_n . Reprinted with permission from Miner et al., 2019. Copyright 2019 American Chemical Society.

Although these emerging MOFs are potential alternatives to current polymer/ceramic electrolytes, the study of MOF-based electrolytes is still in its early stages, and concerns arise about the complexity of the synthesis process.

2.3.3 Chalcogenides

The substitution of sulfur ions for oxygen ions in Mg^{2+} SSEs enables lower-temperature synthesis and yielding materials with weaker Mg-S bonding strength, increased flexibility, and wider ion migration tunnels. The structural frameworks with high Mg mobility, such as MgX_2Z_4 spinel structures (where $Z = \text{S}$ and Se and $X = \text{In}$, Y , and Sc) (Canepa et al., 2017), has been a key strategy to decrease migration energy barriers. Notably, MgSc_2Se_4 has shown fast Mg^{2+} mobility of $10^{-4} \text{ S cm}^{-1}$ at room

temperature with a low migration barrier ($\sim 370 \pm 90$ meV). Nevertheless, 0.04% of the overall conductivity was ascribed to electronic conductivity, greater than that of existing solid-state electrolytes, which typically range from 10^{-4} to 10^{-6} S cm⁻¹ at room temperature (Canepa et al., 2017). The proposed strategies to lower electronic conductivity through Se-rich phases and aliovalent doping (Ti⁴⁺ and Ce⁴⁺) have proven ineffective in neutralizing electronic conductivity (L.-P. Wang et al., 2019). Nevertheless, due to its combined fast ionic and electronic conduction properties, spinel MgSc₂Se₄ could effectively insert/extract Mg²⁺ ions reversibly as cathode materials (M. Guo et al., 2022).

2.3.4 Polymers

Polymers have emerged as promising materials for SSEs due to their flexibility, light weight, and easy processing. Solid polymer electrolytes (SPEs) are typically formed by complexing a polymer matrix with magnesium salts (B. Park and Schaefer, 2020). The ionic conductivity of SPEs depends on the dissociation ability of the salt within the polymer matrix, providing Mg²⁺ ions for conduction. However, ionic conductivity is also influenced by ion transport associated with the segmental motion of the polymer. Therefore, notable conductivity of SPE is evident only above the glass transition temperature. Polyethylene oxide (PEO) is the common polymer host due to its high solubility and low vitrification temperature. By complexing of PEO with the magnesium salts (Mg(TFSI)₂, Mg(NO₃)₂, and Mg(Tf)₂), Mg²⁺ ionic conductivity in the range of 3.21×10^{-8} – 10^{-5} S cm⁻¹ at room temperature could be obtained (Ab Aziz and Tominaga, 2018; Acosta and Morales, 1998; Bakker, Gejji, Lindgren, Hermansson, and Probst, 1995; Ramalingaiah, Reddy, Reddy, Laxminarsaiah, and Rao, 1996). However, findings from direct current (DC) analysis revealed that the primary conductive ions in these electrolytes were anions, causing by the strong electrostatic interaction between the Mg ion and the ether chain oxygens (Shi and Vincent, 1993; Vincent, 1995). In conclusion, polymers and their composites present a promising avenue for advancing the field of SSEs, addressing challenges related to conductivity, stability, and mechanical properties.

2.3.5 Hydrides

The interest in complex metal borohydrides as SSEs has greatly increased since the discovery of super ionic conductivity ($\sigma \sim 10^{-3} \text{ S cm}^{-1}$) in a high-temperature polymorph of lithium borohydride in 2007 (Matsuo, Nakamori, Orimo, Maekawa, and Takamura, 2007). Since then, research into magnesium borohydride ($\text{Mg}(\text{BH}_4)_2$) systems have brought fast solid-state magnesium ionic conductors from high temperature to ambient conditions. Pure α - $\text{Mg}(\text{BH}_4)_2$ exhibits a low solid-state ionic conductivity of $1 \times 10^{-9} \text{ S cm}^{-1}$ at $150 \text{ }^\circ\text{C}$, reflecting that Mg^{2+} is confined in tetrahedral sites surrounded by four edge-sharing $[\text{BH}_4]^-$ anions.

Anion substitution in $\text{Mg}(\text{BH}_4)_2$ and inclusion of neutral molecules as ligands for magnesium has been used as methods for enhancing the Mg^{2+} conductivity (Amdisen, Grinderslev, Skov, and Jensen, 2023; Cuevas et al., 2022; Grinderslev et al., 2021; Kisu et al., 2020; Kristensen, Amdisen, Skov, and Jensen, 2022; Matsuo et al., 2013; Roedern, Kühnel, Remhof, and Battaglia, 2017; Skov, Grinderslev, Rosenkranz, Lee, and Jensen, 2022; Yan, Dononelli, et al., 2020; Yan, Grinderslev, et al., 2020). One of the best performing systems was $(\text{Mg}(\text{BH}_4)_2 \cdot \text{NH}_3)_x (\text{Mg}(\text{BH}_4)_2 \cdot 2\text{NH}_3)_{1-x}$ composite, which an optimal composition for conductivity was at $x = 0.4$ forming an eutectic melt at $T = 55 \text{ }^\circ\text{C}$ for $x = 0.5$ (Yan, Grinderslev, et al., 2020). Above $55 \text{ }^\circ\text{C}$, the composite melts, which significantly lowers the activation energy to $E_a = 0.38 \text{ eV}$, as ascribed to the increase of dynamics of the material. Recent results showed that the addition of insulating oxide nanoparticles, e.g. 75 wt.% MgO or 67 wt.% Al_2O_3 , stabilized the molten state and provided ionic conductivities in the order of $10^{-5} \text{ S cm}^{-1}$ at room temperature with E_a of $0.55 - 0.96 \text{ eV}$ (Yan et al., 2022; Yan, Grinderslev, et al., 2020). The applicability of $\text{Mg}(\text{BH}_4)_2 \cdot 1.6\text{NH}_3$ with 75 wt.% MgO has also been demonstrated in an all-solid-state battery using a magnesium-metal anode and layered TiS_2 as cathode (Skov et al., 2022). Meanwhile nanocomposites with $\text{Mg}(\text{BH}_4)_2 \cdot 1.6\text{NH}_3$ have been investigated, which the effect of confinement inside a nanoporous scaffold was explored. Nanoconfinement has successfully been used to stabilize the high dynamic phase of other complex hydrides (Blanchard et al., 2015; Choi et al., 2017; Choi, Lee, Oh, and Cho, 2016; Lambregts et al., 2019; Suwarno et al., 2017). For example, by confining LiBH_4 in a

mesoporous silica scaffold (MCM-41), the ionic conductivity increased from $\sigma(\text{Li}^+) \sim 10^{-8}$ to $\sim 10^{-4} \text{ S cm}^{-1}$ at room temperature. This was attributed to the stabilization of a highly dynamic state of LiBH_4 by the silica pore walls (Blanchard et al., 2015; Suwarno et al., 2017; Zettl et al., 2020). In this thesis, the effect of nanoconfined $\text{Mg}(\text{BH}_4)_2 \cdot 1.47\text{NH}_3$ in the pores of mesoporous silica SBA-15 via melt infiltration is discussed, along with the effects of the pore filling degrees on the Mg^{2+} ionic conductivity. Finally, the thermal stabilities of the nanocomposites are investigated. The results and discussions will be presented in Chapter IV, Section 4.2.1.

2.4 References

- Ab Aziz, A., and Tominaga, Y. (2018). Magnesium ion-conductive poly(ethylene carbonate) electrolytes. *Ionics*, 24(11), 3475–3481. <https://doi.org/10.1007/s11581-018-2482-x>
- Acosta, J. L., and Morales, E. (1998). Synthesis and characterization of polymeric electrolytes for solid state magnesium batteries. *Electrochimica Acta*, 43(7), 791–797. [https://doi.org/10.1016/S0013-4686\(97\)00123-0](https://doi.org/10.1016/S0013-4686(97)00123-0)
- Ahmad, A. H., and Ghani, F. S. A. (2009). Conductivity and Structural Studies of Magnesium Based Solid Electrolytes. *AIP Conference Proceedings*, 1136(1), 31–35. <https://doi.org/10.1063/1.3160156>
- Amdisen, M. B., Grinderslev, J. B., Skov, L. N., and Jensen, T. R. (2023). Methylamine Magnesium Borohydrides as Electrolytes for All-Solid-State Magnesium Batteries. *Chemistry of Materials*, 35(3), 1440–1448. <https://doi.org/10.1021/acs.chemmater.2c03641>
- Aubrey, M. L., Ameloot, R., Wiers, B. M., and Long, J. R. (2014). Metal–organic frameworks as solid magnesium electrolytes. *Energy & Environmental Science*, 7(2), 667–671. <https://doi.org/10.1039/C3EE43143F>
- Bakker, A., Gejji, S., Lindgren, J., Hermansson, K., and Probst, M. M. (1995). Contact ion pair formation and ether oxygen coordination in the polymer electrolytes $\text{M}[\text{N}(\text{CF}_3\text{SO}_2)_2]_2\text{PEO}_n$ for $\text{M} = \text{Mg}, \text{Ca}, \text{Sr}$ and Ba . *Polymer*, 36(23), 4371–4378. [https://doi.org/10.1016/0032-3861\(95\)96841-U](https://doi.org/10.1016/0032-3861(95)96841-U)

- Blanchard, D., Nale, A., Sveinbjörnsson, D., Eggenhuisen, T. M., Verkuijlen, M. H. W., Suwarno, ... De Jongh, P. E. (2015). Nanoconfined LiBH_4 as a Fast Lithium Ion Conductor. *Advanced Functional Materials*, 25(2), 184–192. <https://doi.org/10.1002/adfm.201402538>
- Bogdanović, B., Felderhoff, M., Pommerin, A., Schüth, F., and Spielkamp, N. (2006). Advanced Hydrogen-Storage Materials Based on Sc-, Ce-, and Pr-Doped NaAlH_4 . *Advanced Materials*, 18(9), 1198–1201. <https://doi.org/10.1002/adma.200501367>
- Bogdanović, Borislav, and Schwickardi, M. (1997). Ti-doped alkali metal aluminium hydrides as potential novel reversible hydrogen storage materials1Invited paper presented at the International Symposium on Metal–Hydrogen Systems, Les Diablerets, August 25–30, 1996, Switzerland.1. *Journal of Alloys and Compounds*, 253–254, 1–9. [https://doi.org/10.1016/S0925-8388\(96\)03049-6](https://doi.org/10.1016/S0925-8388(96)03049-6)
- Bösenberg, U., Kim, J. W., Gosslar, D., Eigen, N., Jensen, T. R., von Colbe, J. M. B., ... Dornheim, M. (2010). Role of additives in LiBH_4 – MgH_2 reactive hydride composites for sorption kinetics. *Acta Materialia*, 58(9), 3381–3389. <https://doi.org/10.1016/j.actamat.2010.02.012>
- Bösenberg, Ulrike, Doppiu, S., Mosegaard, L., Barkhordarian, G., Eigen, N., Borgschulte, A., ... Bormann, R. (2007). Hydrogen sorption properties of MgH_2 – LiBH_4 composites. *Acta Materialia*, 55(11), 3951–3958. <https://doi.org/10.1016/j.actamat.2007.03.010>
- Canepa, P., Bo, S.-H., Sai Gautam, G., Key, B., Richards, W. D., Shi, T., ... Ceder, G. (2017). High magnesium mobility in ternary spinel chalcogenides. *Nature Communications*, 8(1), 1759. <https://doi.org/10.1038/s41467-017-01772-1>
- Capurso, G., Agresti, F., Russo, S. L., Maddalena, A., Principi, G., Cavallari, A., and Guardamagna, C. (2011). Performance tests of a small hydrogen reactor based on Mg–Al pellets. *Journal of Alloys and Compounds*, 509, S646–S649. <https://doi.org/10.1016/j.jallcom.2010.11.104>
- Chaise, A., de Rango, P., Marty, Ph., and Fruchart, D. (2010). Experimental and numerical study of a magnesium hydride tank. *International Journal of Hydrogen Energy*, 35(12), 6311–6322. <https://doi.org/10.1016/j.ijhydene.2010.03.057>

- Chaise, A., De Rango, P., Marty, Ph., Fruchart, D., Miraglia, S., Olivès, R., and Garrier, S. (2009). Enhancement of hydrogen sorption in magnesium hydride using expanded natural graphite. *International Journal of Hydrogen Energy*, *34*(20), 8589–8596. <https://doi.org/10.1016/j.ijhydene.2009.07.112>
- Chen, P., Xiong, Z., Luo, J., Lin, J., and Tan, K. L. (2002). Interaction of hydrogen with metal nitrides and imides. *Nature*, *420*(6913), 302–304. <https://doi.org/10.1038/nature01210>
- Chen, Z., Ma, Z., Zheng, J., Li, X., Akiba, E., and Li, H.-W. (2021). Perspectives and challenges of hydrogen storage in solid-state hydrides. *Chinese Journal of Chemical Engineering*, *29*, 1–12. <https://doi.org/10.1016/j.cjche.2020.08.024>
- Cho, I. H., Gang, S., Lee, H., Shim, J.-H., Park, M., and Choi, Y. N. (2016). Kinetic enhancement of $\text{LiBH}_4\text{-MgH}_2$ composite by pre-milled MWCNTs observed by in situ X-ray diffraction measurements. *International Journal of Hydrogen Energy*, *41*(47), 22090–22096. <https://doi.org/10.1016/j.ijhydene.2016.09.141>
- Choi, Y. S., Lee, Y.-S., Choi, D.-J., Chae, K. H., Oh, K. H., and Cho, Y. W. (2017). Enhanced Li Ion Conductivity in $\text{LiBH}_4\text{-Al}_2\text{O}_3$ Mixture via Interface Engineering. *The Journal of Physical Chemistry C*, *121*(47), 26209–26215. <https://doi.org/10.1021/acs.jpcc.7b08862>
- Choi, Y. S., Lee, Y.-S., Oh, K. H., and Cho, Y. W. (2016). Interface-enhanced Li ion conduction in a $\text{LiBH}_4\text{-SiO}_2$ solid electrolyte. *Physical Chemistry Chemical Physics*, *18*(32), 22540–22547. <https://doi.org/10.1039/C6CP03563A>
- Chong, M., Matsuo, M., Orimo, S., Autrey, T., and Jensen, C. M. (2015). Selective Reversible Hydrogenation of $\text{Mg}(\text{B}_3\text{H}_8)_2/\text{MgH}_2$ to $\text{Mg}(\text{BH}_4)_2$: Pathway to Reversible Borane-Based Hydrogen Storage? *Inorganic Chemistry*, *54*(8), 4120–4125. <https://doi.org/10.1021/acs.inorgchem.5b00373>
- Chung, C. A., Yang, S.-W., Yang, C.-Y., Hsu, C.-W., and Chiu, P.-Y. (2013). Experimental study on the hydrogen charge and discharge rates of metal hydride tanks using heat pipes to enhance heat transfer. *Applied Energy*, *103*, 581–587. <https://doi.org/10.1016/j.apenergy.2012.10.024>
- Crivello, J.-C., Dam, B., Denys, R. V., Dornheim, M., Grant, D. M., Huot, J., ... Yartys, V. A. (2016). Review of magnesium hydride-based materials: Development and

- optimisation. *Applied Physics A*, 122(2), 97. <https://doi.org/10.1007/s00339-016-9602-0>
- Cuevas, F., Amdisen, M. B., Baricco, M., Buckley, C. E., Cho, Y. W., Jongh, P. de, ... Latroche, M. (2022). Metallic and complex hydride-based electrochemical storage of energy. *Progress in Energy*, 4(3), 032001. <https://doi.org/10.1088/2516-1083/ac665b>
- Delhomme, B., Lanzini, A., Ortigoza-Villalba, G. A., Nachev, S., de Rango, P., Santarelli, M., ... Leone, P. (2013). Coupling and thermal integration of a solid oxide fuel cell with a magnesium hydride tank. *International Journal of Hydrogen Energy*, 38(11), 4740–4747. <https://doi.org/10.1016/j.ijhydene.2013.01.140>
- Deprez, E., Justo, A., Rojas, T. C., López-Cartés, C., Bonatto Minella, C., Bösenberg, U., ... Fernández, A. (2010). Microstructural study of the LiBH₄-MgH₂ reactive hydride composite with and without Ti-isopropoxide additive. *Acta Materialia*, 58(17), 5683–5694. <https://doi.org/10.1016/j.actamat.2010.06.043>
- Dincă, M., Dailly, A., and Long, J. R. (2008). Structure and Charge Control in Metal–Organic Frameworks Based on the Tetrahedral Ligand Tetrakis(4-tetrazolylphenyl)methane. *Chemistry – A European Journal*, 14(33), 10280–10285. <https://doi.org/10.1002/chem.200801336>
- Dornheim, M. (2011). Thermodynamics of Metal Hydrides: Tailoring Reaction Enthalpies of Hydrogen Storage Materials. In *Thermodynamics—Interaction Studies—Solids, Liquids and Gases*. IntechOpen. <https://doi.org/10.5772/21662>
- El-Eskandarany, M. Sherif, Al-Nasrallah, E., Banyan, M., and Al-Ajmi, F. (2018). Bulk nanocomposite MgH₂/10 wt% (8Nb₂O₅/2Ni) solid-hydrogen storage system for fuel cell applications. *International Journal of Hydrogen Energy*, 43(52), 23382–23396. <https://doi.org/10.1016/j.ijhydene.2018.10.189>
- El-Eskandarany, M.S., Shaban, E., Aldakheel, F., Alkandary, A., Behbehani, M., and Al-Saidi, M. (2017). Synthetic nanocomposite MgH₂/5wt. % TiMn₂ powders for solid-hydrogen storage tank integrated with PEM fuel cell. *Scientific Reports*, 7(1). Scopus. <https://doi.org/10.1038/s41598-017-13483-0>
- Fan, M.-Q., Sun, L.-X., Zhang, Y., Xu, F., Zhang, J., and Chu, H. (2008). The catalytic effect of additive Nb₂O₅ on the reversible hydrogen storage performances of LiBH₄-

- MgH₂ composite. *International Journal of Hydrogen Energy*, 33(1), 74–80. <https://doi.org/10.1016/j.ijhydene.2007.09.012>
- Fernández, A., Deprez, E., and Friedrichs, O. (2011). A comparative study of the role of additive in the MgH₂ vs. The LiBH₄-MgH₂ hydrogen storage system. *International Journal of Hydrogen Energy*, 36(6), 3932–3940. <https://doi.org/10.1016/j.ijhydene.2010.12.112>
- Garrier, S., Chaise, A., De Rango, P., Marty, P., Delhomme, B., Fruchart, D., and Miraglia, S. (2011). MgH₂ intermediate scale tank tests under various experimental conditions. *International Journal of Hydrogen Energy*, 36(16), 9719–9726. <https://doi.org/10.1016/j.ijhydene.2011.05.017>
- Gattia, D. M., Jangir, M., and Jain, I. P. (2019). Study on nanostructured MgH₂ with Fe and its oxides for hydrogen storage applications. *Journal of Alloys and Compounds*, 801, 188–191. <https://doi.org/10.1016/j.jallcom.2019.06.067>
- Gosalawit-Utke, R., Meethom, S., Pistidda, C., Milanese, C., Laipple, D., Saisopa, T., ... Dornheim, M. (2014). Destabilization of LiBH₄ by nanoconfinement in PMMA-co-BM polymer matrix for reversible hydrogen storage. *International Journal of Hydrogen Energy*, 39(10), 5019–5029. <https://doi.org/10.1016/j.ijhydene.2014.01.078>
- Gosalawit-Utke, R., Milanese, C., Nielsen, T. K., Karimi, F., Saldan, I., Pranzas, K., ... Dornheim, M. (2013). Nanoconfined 2LiBH₄-MgH₂ for reversible hydrogen storages: Reaction mechanisms, kinetics, and thermodynamics. *International Journal of Hydrogen Energy*, 38(4), 1932–1942. <https://doi.org/10.1016/j.ijhydene.2012.11.064>
- Grady, Z. A., Wilkinson, C. J., Randall, C. A., and Mauro, J. C. (2020). Emerging Role of Non-crystalline Electrolytes in Solid-State Battery Research. *Frontiers in Energy Research*, 8, 218. <https://doi.org/10.3389/fenrg.2020.00218>
- Grinderslev, J. B., Amdisen, M. B., Skov, L. N., Møller, K. T., Kristensen, L. G., Polanski, M., ... Jensen, T. R. (2021). New Perspectives of Functional Metal Borohydrides. *Journal of Alloys and Compounds*, 163014. <https://doi.org/10.1016/j.jallcom.2021.163014>

- Grinderslev, J. B., Møller, K. T., Yan, Y., Chen, X.-M., Li, Y., Li, H.-W., ... Jensen, T. R. (2019). Potassium octahydridotriborate: Diverse polymorphism in a potential hydrogen storage material and potassium ion conductor. *Dalton Transactions*, 48(24), 8872–8881. <https://doi.org/10.1039/C9DT00742C>
- Guo, L., Jiao, L., Li, L., Wang, Q., Liu, G., Du, H., ... Yuan, H. (2013). Enhanced desorption properties of LiBH₄ incorporated into mesoporous TiO₂. *International Journal of Hydrogen Energy*, 38(1), 162–168. <https://doi.org/10.1016/j.ijhydene.2012.10.038>
- Guo, M., Yuan, C., Zhang, T., and Yu, X. (2022). Solid-State Electrolytes for Rechargeable Magnesium-Ion Batteries: From Structure to Mechanism. *Small*, 18(43), 2106981. <https://doi.org/10.1002/sml.202106981>
- Haghparsat, M. R., and Rajabi, M. (2015). Hydrogen Desorption Properties of MgH₂-5 at% Ti-Cr-Mn-Fe-V Composite Via Combined Vacuum Arc Remelting and Mechanical Alloying. *Procedia Materials Science*, 11, 605–610. <https://doi.org/10.1016/j.mspro.2015.11.091>
- Hanada, N., Ichikawa, T., and Fujii, H. (2005). Catalytic Effect of Nanoparticle 3d-Transition Metals on Hydrogen Storage Properties in Magnesium Hydride MgH₂ Prepared by Mechanical Milling. *The Journal of Physical Chemistry B*, 109(15), 7188–7194. <https://doi.org/10.1021/jp044576c>
- Huang, X., Xiao, X., Wang, X., Yao, Z., Wang, C., Fan, X., and Chen, L. (2018). Highly synergetic catalytic mechanism of Ni@C₃N₄ on the superior hydrogen storage performance of Li-Mg-B-H system. *Energy Storage Materials*, 13, 199–206. <https://doi.org/10.1016/j.ensm.2018.01.012>
- Ikeda, S., Takahashi, M., Ishikawa, J., and Ito, K. (1987). Solid electrolytes with multivalent cation conduction. 1. Conducting species in Mg-Zr-PO₄ system. *Solid State Ionics*, 23(1–2), 125–129. [https://doi.org/10.1016/0167-2738\(87\)90091-9](https://doi.org/10.1016/0167-2738(87)90091-9)
- Jangir, M., Jain, A., Yamaguchi, S., Ichikawa, T., Lal, C., and Jain, I. P. (2016). Catalytic effect of TiF₄ in improving hydrogen storage properties of MgH₂. *International Journal of Hydrogen Energy*, 41(32), 14178–14183. <https://doi.org/10.1016/j.ijhydene.2016.06.238>

- Jaschin, P. W., Gao, Y., Li, Y., and Bo, S.-H. (2020). A materials perspective on magnesium-ion-based solid-state electrolytes. *Journal of Materials Chemistry A*, 8(6), 2875–2897. <https://doi.org/10.1039/C9TA11729F>
- Jia, Y., and Yao, X. (2017). Carbon scaffold modified by metal (Ni) or non-metal (N) to enhance hydrogen storage of MgH₂ through nanoconfinement. *International Journal of Hydrogen Energy*, 42(36), 22933–22941. <https://doi.org/10.1016/j.ijhydene.2017.07.106>
- Kim, J. W., Ahn, J.-P., Jin, S.-A., Lee, S. H., Chung, H.-S., Shim, J.-H., ... Oh, K. H. (2008). Microstructural evolution of NbF₅-doped MgH₂ exhibiting fast hydrogen sorption kinetics. *Journal of Power Sources*, 178(1), 373–378. <https://doi.org/10.1016/j.jpowsour.2007.12.005>
- Kisu, K., Kim, S., Inukai, M., Oguchi, H., Takagi, S., and Orimo, S. (2020). Magnesium Borohydride Ammonia Borane as a Magnesium Ionic Conductor. *ACS Applied Energy Materials*, 3(4), 3174–3179. <https://doi.org/10.1021/acsaem.0c00113>
- Kristensen, L. G., Amdisen, M. B., Skov, L. N., and Jensen, T. R. (2022). Fast magnesium ion conducting isopropylamine magnesium borohydride enhanced by hydrophobic interactions. *Physical Chemistry Chemical Physics*, 24(30), 18185–18197. <https://doi.org/10.1039/D1CP05063J>
- Lambregts, S. F. H., Van Eck, E. R. H., Suwarno, Ngene, P., De Jongh, P. E., and Kentgens, A. P. M. (2019). Phase Behavior and Ion Dynamics of Nanoconfined LiBH₄ in Silica. *The Journal of Physical Chemistry C*, 123(42), 25559–25569. <https://doi.org/10.1021/acs.jpcc.9b06477>
- Li, H.-W., Yan, Y., Orimo, S., Züttel, A., and Jensen, C. M. (2011). Recent Progress in Metal Borohydrides for Hydrogen Storage. *Energies*, 4(1), 185–214. <https://doi.org/10.3390/en4010185>
- Li, Y., Izuhara, T., and Takeshita, H. T. (2011). Promotional Effect of Aluminum on MgH₂+LiBH₄ Hydrogen Storage Materials. *Materials Transactions*, 52(4), 641–646. <https://doi.org/10.2320/matertrans.MA201005>
- Liu, J., Ma, Z., Liu, Z., Tang, Q., Zhu, Y., Lin, H., ... Li, L. (2020). Synergistic effect of rGO supported Ni₃Fe on hydrogen storage performance of MgH₂. *International*

Journal of Hydrogen Energy, 45(33), 16622–16633.
<https://doi.org/10.1016/j.ijhydene.2020.04.104>

Lotosky, M., Denys, R., Yartys, V. A., Eriksen, J., Goh, J., Nyamsi, S. N., ... Cummings, F. (2018). An outstanding effect of graphite in nano-MgH₂-TiH₂ on hydrogen storage performance. *Journal of Materials Chemistry A*, 6(23), 10740–10754. Scopus.
<https://doi.org/10.1039/c8ta02969e>

Lu, Z.-Y., Yu, H.-J., Lu, X., Song, M.-C., Wu, F.-Y., Zheng, J.-G., ... Zhang, L.-T. (2021). Two-dimensional vanadium nanosheets as a remarkably effective catalyst for hydrogen storage in MgH₂. *Rare Metals*, 40(11), 3195–3204.
<https://doi.org/10.1007/s12598-021-01764-7>

Mao, J., Guo, Z., Yu, X., and Liu, H. (2011). Enhanced hydrogen sorption properties in the LiBH₄-MgH₂ system catalysed by Ru nanoparticles supported on multiwalled carbon nanotubes. *Journal of Alloys and Compounds*, 509(15), 5012–5016. <https://doi.org/10.1016/j.jallcom.2011.02.004>

Matsuo, M., Nakamori, Y., Orimo, S., Maekawa, H., and Takamura, H. (2007). Lithium superionic conduction in lithium borohydride accompanied by structural transition. *Applied Physics Letters*, 91(22), 224103.
<https://doi.org/10.1063/1.2817934>

Matsuo, M., Oguchi, H., Sato, T., Takamura, H., Tsuchida, E., Ikeshoji, T., and Orimo, S. (2013). Sodium and magnesium ionic conduction in complex hydrides. *Journal of Alloys and Compounds*, 580, S98–S101.
<https://doi.org/10.1016/j.jallcom.2013.01.058>

Millet, P. (2014). 14—Hydrogen storage in hydride-forming materials. In A. Basile and A. Iulianelli (Eds.), *Advances in Hydrogen Production, Storage and Distribution* (pp. 368–409). Woodhead Publishing. <https://doi.org/10.1533/9780857097736.3.368>

Miner, E. M., Park, S. S., and Dincă, M. (2019). High Li⁺ and Mg²⁺ Conductivity in a Cu-Azolate Metal–Organic Framework. *Journal of the American Chemical Society*, 141(10), 4422–4427. <https://doi.org/10.1021/jacs.8b13418>

Mustafa, N. S., and Ismail, M. (2017). Hydrogen sorption improvement of MgH₂ catalyzed by CeO₂ nanopowder. *Journal of Alloys and Compounds*, 695, 2532–2538.
<https://doi.org/10.1016/j.jallcom.2016.11.158>

- Na Ranong, C., Höhne, M., Franzen, J., Hapke, J., Fieg, G., Dornheim, M., ... Metz, O. (2009). Concept, Design and Manufacture of a Prototype Hydrogen Storage Tank Based on Sodium Alanate. *Chemical Engineering & Technology*, *32*(8), 1154–1163. <https://doi.org/10.1002/ceat.200900095>
- Ngene, P., Adelhelm, P., Beale, A. M., de Jong, K. P., and de Jongh, P. E. (2010). LiBH₄/SBA-15 Nanocomposites Prepared by Melt Infiltration under Hydrogen Pressure: Synthesis and Hydrogen Sorption Properties. *The Journal of Physical Chemistry C*, *114*(13), 6163–6168. <https://doi.org/10.1021/jp9065949>
- Nielsen, T. K., Bösenberg, U., Gosalawit, R., Dornheim, M., Cerenius, Y., Besenbacher, F., and Jensen, T. R. (2010). A Reversible Nanoconfined Chemical Reaction. *ACS Nano*, *4*(7), 3903–3908. <https://doi.org/10.1021/nn1006946>
- Nielsen, T. K., and Jensen, T. R. (2012). MgH₂–Nb₂O₅ investigated by in situ synchrotron X-ray diffraction. *International Journal of Hydrogen Energy*, *37*(18), 13409–13416. <https://doi.org/10.1016/j.ijhydene.2012.06.082>
- Nyallang Nyamsi, S., Lototsky, M. V., Yartys, V. A., Capurso, G., Davids, M. W., and Pasupathi, S. (2021). 200 NL H₂ hydrogen storage tank using MgH₂–TiH₂–C nanocomposite as H storage material. *International Journal of Hydrogen Energy*, *46*(36), 19046–19059. <https://doi.org/10.1016/j.ijhydene.2021.03.055>
- Ouyang, L. Z., Cao, Z. J., Wang, H., Liu, J. W., Sun, D. L., Zhang, Q. A., and Zhu, M. (2013). Dual-tuning effect of In on the thermodynamic and kinetic properties of Mg₂Ni dehydrogenation. *International Journal of Hydrogen Energy*, *38*(21), 8881–8887. <https://doi.org/10.1016/j.ijhydene.2013.05.027>
- Park, B., and Schaefer, J. L. (2020). Review—Polymer Electrolytes for Magnesium Batteries: Forging Away from Analogs of Lithium Polymer Electrolytes and Towards the Rechargeable Magnesium Metal Polymer Battery. *Journal of The Electrochemical Society*, *167*(7), 070545. <https://doi.org/10.1149/1945-7111/ab7c71>
- Park, S. S., Tulchinsky, Y., and Dincă, M. (2017). Single-Ion Li⁺, Na⁺, and Mg²⁺ Solid Electrolytes Supported by a Mesoporous Anionic Cu–Azolate Metal–Organic Framework. *Journal of the American Chemical Society*, *139*(38), 13260–13263. <https://doi.org/10.1021/jacs.7b06197>

- Paskevicius, M., Jepsen, L. H., Schouwink, P., Černý, R., Ravnsbæk, D. B., Filinchuk, Y., ... Jensen, T. R. (2017). Metal borohydrides and derivatives – synthesis, structure and properties. *Chemical Society Reviews*, 46(5), 1565–1634. <https://doi.org/10.1039/C6CS00705H>
- Paskevicius, M., Sheppard, D. A., and Buckley, C. E. (2010). Thermodynamic Changes in Mechanochemically Synthesized Magnesium Hydride Nanoparticles. *Journal of the American Chemical Society*, 132(14), 5077–5083. <https://doi.org/10.1021/ja908398u>
- Patel, M., Mishra, K., Banerjee, R., Chaudhari, J., Kanchan, D. K., and Kumar, D. (2023). Fundamentals, recent developments and prospects of lithium and non-lithium electrochemical rechargeable battery systems. *Journal of Energy Chemistry*, 81, 221–259. <https://doi.org/10.1016/j.jechem.2023.02.023>
- Peng, B., Liang, J., Tao, Z., and Chen, J. (2009). Magnesium nanostructures for energy storage and conversion. *Journal of Materials Chemistry*, 19(19), 2877–2883. <https://doi.org/10.1039/B816478A>
- Plerdsranoy, P., Chanthee, S., and Utke, R. (2017). Compaction of LiBH₄-MgH₂ doped with MWCNTs-TiO₂ for reversible hydrogen storage. *International Journal of Hydrogen Energy*, 42(2), 978–986. <https://doi.org/10.1016/j.ijhydene.2016.11.066>
- Plerdsranoy, P., Wiset, N., Milanese, C., Laipple, D., Marini, A., Klassen, T., ... Gosalawit-Utke, R. (2015). Improvement of thermal stability and reduction of LiBH₄/polymer host interaction of nanoconfined LiBH₄ for reversible hydrogen storage. *International Journal of Hydrogen Energy*, 40(1), 392–402. <https://doi.org/10.1016/j.ijhydene.2014.10.090>
- Pukazhselvan, D., Nasani, N., Sandhya, K. S., Singh, B., Bdikin, I., Koga, N., and Fagg, D. P. (2017). Role of chemical interaction between MgH₂ and TiO₂ additive on the hydrogen storage behavior of MgH₂. *Applied Surface Science*, 420, 740–745. <https://doi.org/10.1016/j.apsusc.2017.05.182>
- Puszkil, J. A., Gennari, F. C., Larochette, P. A., Ramallo-López, J. M., Vainio, U., Karimi, F., ... Dornheim, M. (2015). Effect of Fe additive on the hydrogenation-

- dehydrogenation properties of $2\text{LiH} + \text{MgB}_2/2\text{LiBH}_4 + \text{MgH}_2$ system. *Journal of Power Sources*, 284, 606–616. <https://doi.org/10.1016/j.jpowsour.2015.02.153>
- Ramalingaiah, S., Reddy, D. S., Reddy, M. J., Laxminarsaiah, E., and Rao, U. V. S. (1996). Conductivity and discharge characteristic studies of novel polymer electrolyte based on PEO complexed with $\text{Mg}(\text{NO}_3)_2$ salt. *Materials Letters*, 29(4), 285–289. [https://doi.org/10.1016/S0167-577X\(96\)00161-9](https://doi.org/10.1016/S0167-577X(96)00161-9)
- Rangsunvigit, P., Sridechprasat, P., Kitiyanan, B., and Kulprathipanja, S. (2014). Effects of TiCl_3 , TiO_2 , ZrCl_4 , and ZrO_2 on hydrogen desorption of MgH_2 and its reversibility. *Chemical Engineering Transactions*, 39(Special Issue), 1201–1206. Scopus. <https://doi.org/10.3303/CET1439201>
- Roedern, E., Kühnel, R.-S., Remhof, A., and Battaglia, C. (2017). Magnesium Ethylenediamine Borohydride as Solid-State Electrolyte for Magnesium Batteries. *Scientific Reports*, 7(1), 46189. <https://doi.org/10.1038/srep46189>
- Shao, H., Wang, Y., Xu, H., and Li, X. (2004). Hydrogen storage properties of magnesium ultrafine particles prepared by hydrogen plasma-metal reaction. *Materials Science and Engineering: B*, 110(2), 221–226. <https://doi.org/10.1016/j.mseb.2004.03.013>
- Sherif El-Eskandarany, M., Alkandary, A., Aldakheel, F., Al-Saidi, M., Al-Ajmi, F., and Banyan, M. (2018). Performance and fuel cell applications of reacted ball-milled $\text{MgH}_2/5.3$ wt% TiH_2 nanocomposite powders. *RSC Advances*, 8(67), 38175–38185. <https://doi.org/10.1039/C8RA06570E>
- Shi, J., and Vincent, C. A. (1993). The effect of molecular weight on cation mobility in polymer electrolytes. *Solid State Ionics*, 60(1), 11–17. [https://doi.org/10.1016/0167-2738\(93\)90268-8](https://doi.org/10.1016/0167-2738(93)90268-8)
- Sitthiwet, C., Thiangviriya, S., Thaweelap, N., Meethom, S., Kaewsuwan, D., Chanlek, N., and Utke, R. (2017). Hydrogen sorption and permeability of compacted LiBH_4 nanoconfined into activated carbon nanofibers impregnated with TiO_2 . *Journal of Physics and Chemistry of Solids*, 110, 344–353. <https://doi.org/10.1016/j.jpics.2017.06.035>

- Skov, L. N., Grinderslev, J. B., Rosenkranz, A., Lee, Y.-S., and Jensen, T. R. (2022). Towards Solid-State Magnesium Batteries: Ligand-Assisted Superionic Conductivity. *Batteries Supercaps*, 5(9), e202200163. <https://doi.org/10.1002/batt.202200163>
- Song, M. Y., Kwon, S. N., Park, H. R., and Hong, S.-H. (2011). Improvement in the hydrogen storage properties of Mg by mechanical grinding with Ni, Fe and V under H₂ atmosphere. *International Journal of Hydrogen Energy*, 36(21), 13587–13594. <https://doi.org/10.1016/j.ijhydene.2011.07.107>
- Sridechprasat, P., Suttisawat, Y., Rangsunvigit, P., Kitiyanan, B., and Kulprathipanja, S. (2011). Catalyzed LiBH₄ and MgH₂ mixture for hydrogen storage. *International Journal of Hydrogen Energy*, 36(1), 1200–1205. <https://doi.org/10.1016/j.ijhydene.2010.07.003>
- Srinivasan, S. S., Brinks, H. W., Hauback, B. C., Sun, D., and Jensen, C. M. (2004). Long term cycling behavior of titanium doped NaAlH₄ prepared through solvent mediated milling of NaH and Al with titanium dopant precursors. *Journal of Alloys and Compounds*, 377(1), 283–289. <https://doi.org/10.1016/j.jallcom.2004.01.044>
- Sulaiman, M., Che Su, N., and Mohamed, N. S. (2017). Sol-gel synthesis and characterization of β -MgSO₄:Mg(NO₃)-MgO composite solid electrolyte. *Ionics*, 23(2), 443–452. <https://doi.org/10.1007/s11581-016-1854-3>
- Sulaiman, Mazdida, Rahman, A. A., and Mohamed, N. S. (2013). Structural, Thermal and Conductivity Studies of Magnesium Nitrate – Alumina Composite Solid Electrolytes Prepared via Sol-Gel Method. *International Journal of Electrochemical Science*, 8(5), 6647–6655. [https://doi.org/10.1016/S1452-3981\(23\)14792-4](https://doi.org/10.1016/S1452-3981(23)14792-4)
- Sun, Z., Zhang, L., Yan, N., Zheng, J., Bian, T., Yang, Z., and Su, S. (2020). Realizing Hydrogen De/Absorption Under Low Temperature for MgH₂ by Doping Mn-Based Catalysts. *Nanomaterials*, 10(9), 1745. <https://doi.org/10.3390/nano10091745>
- Surrey, A., Bonatto Minella, C., Fechler, N., Antonietti, M., Grafe, H.-J., Schultz, L., and Rellinghaus, B. (2016). Improved hydrogen storage properties of LiBH₄ via nanoconfinement in micro- and mesoporous aerogel-like carbon. *International*

- Journal of Hydrogen Energy*, 41(12), 5540–5548.
<https://doi.org/10.1016/j.ijhydene.2016.01.163>
- Suwarno, Ngene, P., Nale, A., Eggenhuisen, T. M., Oschatz, M., Embs, J. P., ... De Jongh, P. E. (2017). Confinement Effects for Lithium Borohydride: Comparing Silica and Carbon Scaffolds. *The Journal of Physical Chemistry C*, 121(8), 4197–4205.
<https://doi.org/10.1021/acs.jpcc.6b13094>
- Thiangviriyaya, S., Plerdsranoy, P., Sitthiwet, C., Dansirima, P., Thongtan, P., Eiamlamai, P., ... Utke, R. (2019). MgH₂-TiF₄-MWCNTs based hydrogen storage tank with central tube heat exchanger. *International Journal of Hydrogen Energy*, 44(36), 20173–20182. <https://doi.org/10.1016/j.ijhydene.2019.06.002>
- Vajo, J. J., Skeith, S. L., and Mertens, F. (2005). Reversible storage of hydrogen in destabilized LiBH₄. *The Journal of Physical Chemistry. B*, 109(9), 3719–3722.
<https://doi.org/10.1021/jp040769o>
- Vigeholm, B., Kjøller, J., Larsen, B., and Pedersen, A. S. (1983). Formation and decomposition of magnesium hydride. *Journal of the Less Common Metals*, 89(1), 135–144. [https://doi.org/10.1016/0022-5088\(83\)90259-X](https://doi.org/10.1016/0022-5088(83)90259-X)
- Vincent, C. A. (1995). Ion transport in polymer electrolytes. *Electrochimica Acta*, 40(13), 2035–2040. [https://doi.org/10.1016/0013-4686\(95\)00138-5](https://doi.org/10.1016/0013-4686(95)00138-5)
- Wahab, M. A., Jia, Y. (Alec), Yang, D., Zhao, H., and Yao, X. (2013). Enhanced hydrogen desorption from Mg(BH₄)₂ by combining nanoconfinement and a Ni catalyst. *Journal of Materials Chemistry A*, 1(10), 3471–3478.
<https://doi.org/10.1039/C2TA00899H>
- Wang, H., Wu, G., Cao, H., Pistidda, C., Chaudhary, A.-L., Garroni, S., ... Chen, P. (2017). Near Ambient Condition Hydrogen Storage in a Synergized Tricomponent Hydride System. *Advanced Energy Materials*, 7(13), 1602456.
<https://doi.org/10.1002/aenm.201602456>
- Wang, J., Liu, T., Wu, G., Li, W., Liu, Y., Araújo, C. M., ... Chen, P. (2009). Potassium-Modified Mg(NH₂)₂/2LiH System for Hydrogen Storage. *Angewandte Chemie International Edition*, 48(32), 5828–5832.
<https://doi.org/10.1002/anie.200805264>

- Wang, K., Kang, X., Luo, J., Hu, C., and Wang, P. (2013). Improved reversible dehydrogenation properties of $\text{LiBH}_4\text{-MgH}_2$ composite by tailoring nanophase structure using activated carbon. *International Journal of Hydrogen Energy*, 38(9), 3710–3716. <https://doi.org/10.1016/j.ijhydene.2013.01.034>
- Wang, L., Rawal, A., Quadir, M. Z., and Aguey-Zinsou, K.-F. (2017). Nanoconfined lithium aluminium hydride (LiAlH_4) and hydrogen reversibility. *International Journal of Hydrogen Energy*, 42(20), 14144–14153. <https://doi.org/10.1016/j.ijhydene.2017.04.104>
- Wang, L.-P., Zhao-Karger, Z., Klein, F., Chable, J., Braun, T., Schür, A. R., ... Fichtner, M. (2019). MgSc_2Se_4 —A Magnesium Solid Ionic Conductor for All-Solid-State Mg Batteries? *ChemSusChem*, 12(10), 2286–2293. <https://doi.org/10.1002/cssc.201900225>
- Wang, P.-J., Fang, Z.-Z., Ma, L.-P., Kang, X.-D., and Wang, P. (2008). Effect of SWNTs on the reversible hydrogen storage properties of $\text{LiBH}_4\text{-MgH}_2$ composite. *International Journal of Hydrogen Energy*, 33(20), 5611–5616. <https://doi.org/10.1016/j.ijhydene.2008.07.045>
- Weng, B. C., Yu, X. B., Wu, Z., Li, Z. L., Huang, T. S., Xu, N. X., and Ni, J. (2010). Improved dehydrogenation performance of $\text{LiBH}_4/\text{MgH}_2$ composite with Pd nanoparticles addition. *Journal of Alloys and Compounds*, 503(2), 345–349. <https://doi.org/10.1016/j.jallcom.2009.11.059>
- Xie, L., Liu, Y., Zhang, X., Qu, J., Wang, Y., and Li, X. (2009). Catalytic effect of Ni nanoparticles on the desorption kinetics of MgH_2 nanoparticles. *Journal of Alloys and Compounds*, 482(1), 388–392. <https://doi.org/10.1016/j.jallcom.2009.04.028>
- Yahya, M. S., and Ismail, M. (2019). Catalytic effect of SrTiO_3 on the hydrogen storage behaviour of MgH_2 . *Journal of Energy Chemistry*, 28, 46–53. <https://doi.org/10.1016/j.jechem.2017.10.020>
- Yan, Y., Dononelli, W., Jørgensen, M., Grinderslev, J. B., Lee, Y.-S., Cho, Y. W., ... Jensen, T. R. (2020). The mechanism of Mg^{2+} conduction in ammine magnesium borohydride promoted by a neutral molecule. *Physical Chemistry Chemical Physics*, 22(17), 9204–9209. <https://doi.org/10.1039/D0CP00158A>

- Yan, Y., Grinderslev, J. B., Burankova, T., Wei, S., Embs, J. P., Skibsted, J., and Jensen, T. R. (2022). Fast Room-Temperature Mg^{2+} Conductivity in $\text{Mg}(\text{BH}_4)_2 \cdot 1.6\text{NH}_3 - \text{Al}_2\text{O}_3$ Nanocomposites. *The Journal of Physical Chemistry Letters*, 13(9), 2211–2216. <https://doi.org/10.1021/acs.jpcllett.2c00136>
- Yan, Y., Grinderslev, J. B., Jørgensen, M., Skov, L. N., Skibsted, J., and Jensen, T. R. (2020). Ammine Magnesium Borohydride Nanocomposites for All-Solid-State Magnesium Batteries. *ACS Applied Energy Materials*, 3(9), 9264–9270. <https://doi.org/10.1021/acsaem.0c01599>
- Yan, Y., Remhof, A., Hwang, S.-J., Li, H.-W., Mauron, P., Orimo, S., and Züttel, A. (2012). Pressure and temperature dependence of the decomposition pathway of LiBH_4 . *Physical Chemistry Chemical Physics*, 14(18), 6514–6519. <https://doi.org/10.1039/C2CP40131B>
- Yang, Y., Zhang, X., Zhang, L., Zhang, W., Liu, H., Huang, Z., ... Pan, H. (2023). Recent advances in catalyst-modified Mg-based hydrogen storage materials. *Journal of Materials Science & Technology*, 163, 182–211. <https://doi.org/10.1016/j.jmst.2023.03.063>
- Yartys, V. A., Lototsky, M. V., Akiba, E., Albert, R., Antonov, V. E., Ares, J. R., ... Zhu, M. (2019). Magnesium based materials for hydrogen based energy storage: Past, present and future. *International Journal of Hydrogen Energy*, 44(15), 7809–7859. <https://doi.org/10.1016/j.ijhydene.2018.12.212>
- Zettl, R., De Kort, L., Gombotz, M., Wilkening, H. M. R., De Jongh, P. E., and Ngene, P. (2020). Combined Effects of Anion Substitution and Nanoconfinement on the Ionic Conductivity of Li-Based Complex Hydrides. *The Journal of Physical Chemistry C*, 124(5), 2806–2816. <https://doi.org/10.1021/acs.jpcc.9b10607>
- Zhan, Y., Zhang, W., Lei, B., Liu, H., and Li, W. (2020). Recent Development of Mg Ion Solid Electrolyte. *Frontiers in Chemistry*, 8, 125. <https://doi.org/10.3389/fchem.2020.00125>
- Zhang, J., Shi, R., Zhu, Y., Liu, Y., Zhang, Y., Li, S., and Li, L. (2018). Remarkable Synergistic Catalysis of Ni-Doped Ultrafine TiO_2 on Hydrogen Sorption Kinetics of MgH_2 . *ACS Applied Materials & Interfaces*, 10(30), 24975–24980. <https://doi.org/10.1021/acsami.8b06865>

- Zhang, X., Shen, Z., Jian, N., Hu, J., Du, F., Yao, J., ... Pan, H. (2018). A novel complex oxide $TiVO_{3.5}$ as a highly active catalytic precursor for improving the hydrogen storage properties of MgH_2 . *International Journal of Hydrogen Energy*, 43(52), 23327–23335. <https://doi.org/10.1016/j.ijhydene.2018.10.216>
- Zhao, R., Wu, Y., Liang, Z., Gao, L., Xia, W., Zhao, Y., and Zou, R. (2020). Metal–organic frameworks for solid-state electrolytes. *Energy & Environmental Science*, 13(8), 2386–2403. <https://doi.org/10.1039/D0EE00153H>
- Zhao, Yan, Liu, H., Liu, Y., Wang, Y., Yuan, H., and Jiao, L. (2017). Synergistic effects of des tabilization, catalysis and nanoconfinement on dehydrogenation of $LiBH_4$. *International Journal of Hydrogen Energy*, 42(2), 1354–1360. <https://doi.org/10.1016/j.ijhydene.2016.03.102>
- Zhao, Yanping, Jiao, L., Liu, Y., Guo, L., Li, L., Liu, H., ... Yuan, H. (2014). A synergistic effect between nanoconfinement of carbon aerogels and catalysis of CoNiB nanoparticles on dehydrogenation of $LiBH_4$. *International Journal of Hydrogen Energy*, 39(2), 917–926. <https://doi.org/10.1016/j.ijhydene.2013.10.137>
- Zhong, Y., Kang, X., Wang, K., and Wang, P. (2014). Improved reversible dehydrogenation of $LiBH_4$ – MgH_2 composite by the synergistic effects of Al and MgO. *International Journal of Hydrogen Energy*, 39(5), 2187–2193. <https://doi.org/10.1016/j.ijhydene.2013.11.119>
- Zhou, H., Liu, H.-Z., Xu, L., Gao, S.-C., Wang, X., and Yan, M. (2017). Hydrogen storage properties of Nb-compounds-catalyzed $LiBH_4$ – MgH_2 . *Rare Metals*, 36(9), 723–728. <https://doi.org/10.1007/s12598-017-0929-2>
- Züttel, A. (2003). Materials for hydrogen storage. *Materials Today*, 6(9), 24–33. [https://doi.org/10.1016/S1369-7021\(03\)00922-2](https://doi.org/10.1016/S1369-7021(03)00922-2)

CHAPTER III

EXPERIMENTAL SECTION

3.1 Sample preparation

3.1.1 Solid-state hydrogen storage

3.1.1.1 Nanoconfined $2\text{LiBH}_4\text{-MgH}_2$ in activated carbon

The powder samples of LiBH_4 (90%, hydrogen storage grade, Sigma Aldrich) and Mg (99%, Sigma Aldrich) were milled in a stainless-steel vial at a 2:1 mole ratio ($\text{LiBH}_4\text{:Mg}$) using a QM0.4L Planetary Ball Mill, Nanjing Chistan Chishun Science & Technology. The ball-to-powder weight ratio (BPR), milling time, and rotational speed were set at 20:1, 10 h, and 580 rpm, respectively. Activated carbon (AC) obtained from a biomass power generation process (The Center of Excellence in Biomass, Suranaree University of Technology, Thailand (“The Center of Excellence in Biomass: BIOMASS SUT,” n.d.)) was treated at 500 °C for 3 h under vacuum. As-milled $\text{LiBH}_4\text{-Mg}$ was mixed with treated AC under 1:1 weight ratio using a mortar. The $\text{LiBH}_4\text{-Mg-AC}$ mixture was heated to 400 °C (5 °C/min) under 40-50 bar H_2 for 10 h to achieve the nanoconfined $2\text{LiBH}_4\text{-MgH}_2$ in AC, denoted as nano LB-MH-AC(1). However, due to incomplete hydrogenation, nano LB-MH-AC(1) was hydrogenated under 40-50 bar H_2 at 350 °C for 10 h to accomplish the final nanoconfined sample, denoted as nano LB-MH-AC(2).

Nano LB-MH-AC(2) was filled into a small cylindrical tank with a packing volume of 21.7 mL (Figure 3.1(A)). The stainless-steel (SS) mesh sheets and a tube (SS304, No.120) were placed within the powder sample to enhance hydrogen diffusion in the tank. The tank comprised three K-type thermocouples (-250 °C to 1300 °C, SL heater), positioned at different depths of the storage tank at 3, 2, and 1 cm, denoted as TC1, TC2, and TC3, respectively (Figure 3.1(B)).

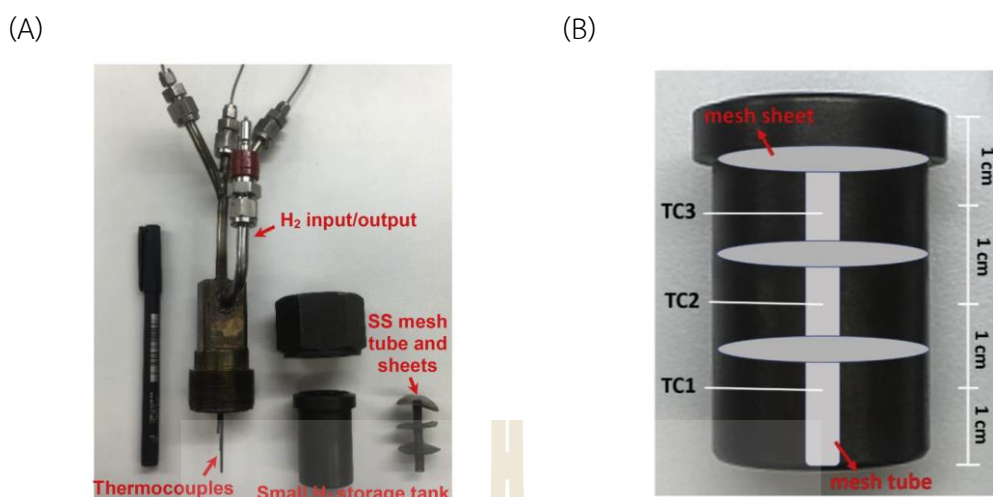


Figure 3.1 Components of small hydrogen storage tank with packing volume of 21.7 mL (A) and the positions of thermocouples (TC1-TC3) in the tank (B).

3.1.1.2 MgH₂ doped with TiF₄ and MWCNTs

Magnesium powder ($\geq 99.0\%$, Aldrich) was hydrogenated at 320 °C under 15-20 bar H₂ for 12 h to obtain as-prepared MgH₂. As-received TiF₄(99%, Acros Organics) and as-prepared MgH₂ were pre-milled for 3 and 5 h, respectively, using a QM 0.4 L Planetary Ball Mill, Nanjing Chishun Science & Technology. As-prepared MgH₂ was doped with 5 wt.% TiF₄ by milling for 3 h and the mixture was hydrogenated at 250 °C under 10-15 bar H₂ for 2 h. Multi-walled carbon nanotubes (MWCNTs, Nano Generation Co., Ltd. Thailand) was treated at 500 °C under vacuum for 3 h. TiF₄-doped MgH₂ was doped with 5 wt.% treated MWCNTs by ball milling for 30 min to achieve TiF₄-MWCNT-doped MgH₂, denoted as TiF₄-CNT-MH. A ball-to-powder weight ratio (BPR) and the rotational speed of 10:1 and 580 rpm, respectively, were applied.

Kinetic properties of MgH₂-TiF₄-CNT were studied in laboratory and tank scales. Dehydrogenation kinetics in laboratory scale was investigated by packing TiF₄-CNT-MH (1.8320 g) into the sample holder with the packing volume of 21.7 mL (Figure 3.2(A)). K-type thermocouple (-250-1300 °C, SL heater) was placed on the sample (Figure 3.2(B)).

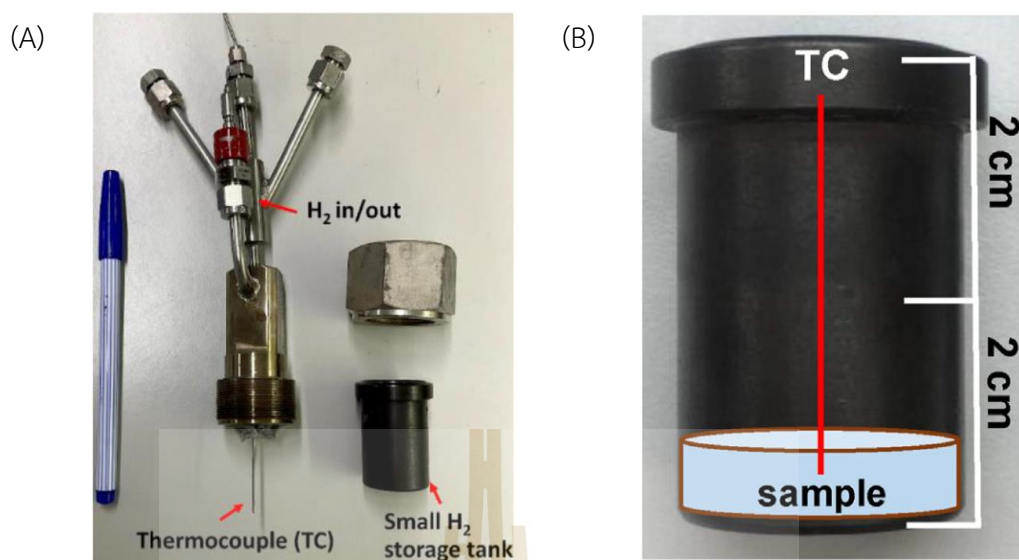


Figure 3.2 The components of the sample container (A) and the position of thermocouple inside the sample container (B) used for kinetic studies in laboratory scale.

For the tank scale, $\text{TiF}_4\text{-CNT-MH}$ (45.2252 g) was packed into the cylindrical hydrogen storage tank with the packing volume of 96.2 mL (Figure 3.3(A)). A porous SS cylinder and four porous SS tubes were inserted into the powder sample to enhance hydrogen diffusion upon de/rehydrogenation. Temperature profiles during dehydrogenation were detected using five K-type thermocouples placed in the axial (TC1-TC3) and the radial (TC2 and TC4-TC5) directions (Figure 3.3(B)). Heat released during exothermic hydrogenation was removed using a central tube heat exchanger filled with 3-5 L/min compressed air at room temperature.

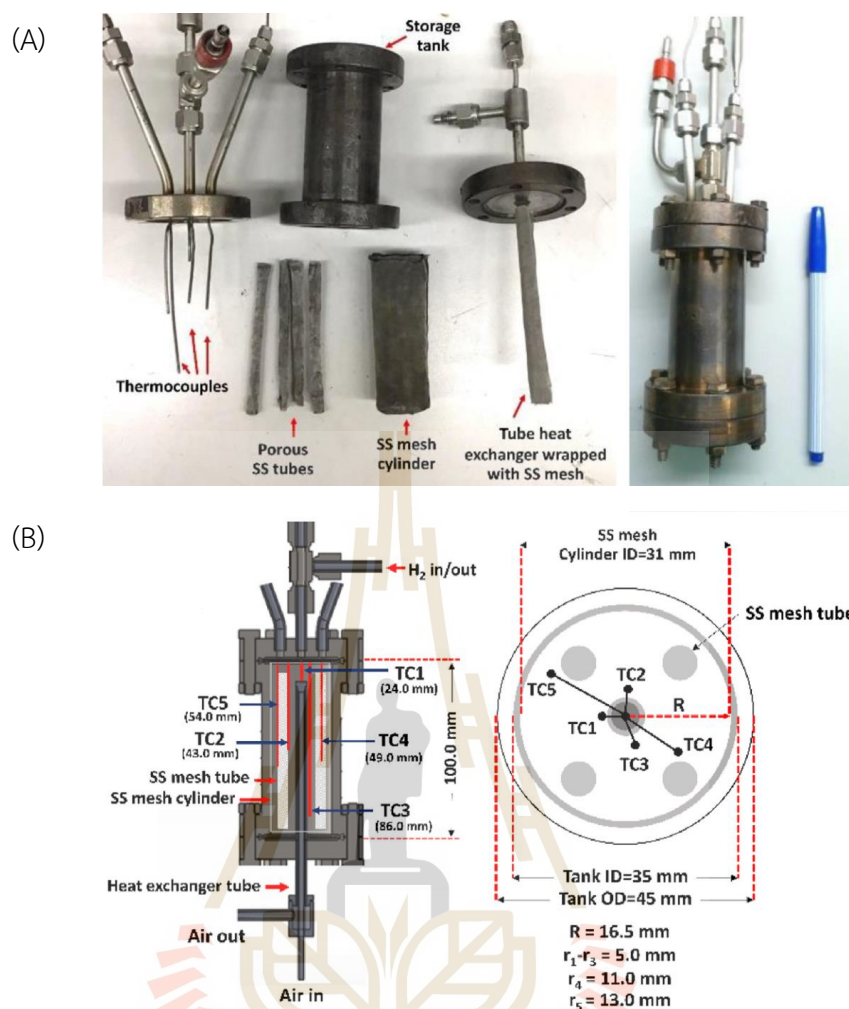


Figure 3.3 The components (A) and the positions of thermocouples inside the sample container (B) used for kinetic study in hydrogen storage tank scale (packing volume of 96.2 mL).

3.1.2 Mg-based solid-state batteries

3.1.2.1 Nanoconfined Mg(BH₄)₂ in mesoporous silica

The synthesis of Mg(BH₄)₂ and Mg(BH₄)₂·1.47NH₃ composite followed the procedure described in the literature (Yan et al., 2020)(Filinchuk et al., 2011). Mg(BH₄)₂·6NH₃ was synthesized by gas-solid reaction between Mg(BH₄)₂ and dry ammonia gas. The Mg(BH₄)₂ powder was exposed to 1 bar NH₃ for 2 h at room temperature. The Mg(BH₄)₂·1.47NH₃ composite was obtained by ball milling of Mg(BH₄)₂ and Mg(BH₄)₂·6NH₃ with 3:1 mole ratio using a Fritz pulverisette 6 with tungsten carbide (WC) vial and balls. Ball-to-powder weight ratio (BPR), milling time, and rotational speed

of 30:1, 7 h, and 200 rpm, respectively, were applied. As-received mesoporous silica SBA-15 (99.9%, Sigma Aldrich) was dried at 300 °C under dynamic vacuum overnight. As-prepared $\text{Mg}(\text{BH}_4)_2 \cdot 1.47\text{NH}_3$ composite and dried SBA-15 were mixed under different pore filling degrees (Table 3.1) in mortar for 10 min. The $\text{Mg}(\text{BH}_4)_2 \cdot 1.47\text{NH}_3$ composite was confined into the pores of SBA-15 by heating to 110 °C (5 °C/min) under 50 bar H_2 for 30 min to obtain nanoconfined samples, denoted as MI100, MI200 and MI300 (Table 3.1).

Table 3.1 Composition and degree of pore filling of samples.

Samples	Mass %		Pore filling (%)
	$\text{Mg}(\text{BH}_4)_2 \cdot 1.47\text{NH}_3$	SBA-15	
MI100	38	62	100
MI200	55	45	200
MI300	65	35	300

3.2 Characterizations

3.2.1 Powder x-ray diffraction

Phase compositions of the samples for hydrogen storage were characterized by powder x-ray diffraction (PXD) utilizing a Bruker D2 PHASER equipped with a $\text{Cu K}\alpha$ source ($\lambda = 1.54056 \text{ \AA}$). The powder sample was placed in a sealed sample holder, covered with a poly(methyl methacrylate) (PMMA) dome under nitrogen (N_2) atmosphere in a glove box. The analysis involved a 2θ range and scanning step of 10-80° and 0.02°/s, respectively.

For the samples for solid-state batteries, diffraction patterns were investigated using a Rigaku SMARTLAB diffractometer equipped with a rotating Cu anode ($\text{Cu K}\alpha$ radiation, 2 kW, $\lambda = 1.54056 \text{ \AA}$). The powder sample was packed in 0.5 mm o.d. borosilicate capillaries in an argon filled glove box, sealed with glue, and transferred to the instrument without air exposure. The structural refinement of the sample was conducted using Fullprof software. The background was described by linear

interpolation between selected points, while Pseudo-Voigt profile functions were used to fit the diffraction peaks.

3.2.2 Fourier-transform infrared spectroscopy

Fourier-transform infrared spectroscopy (FTIR) was used to characterize the functional groups of compounds using a Bruker T27/Hyp 2000 instrument. The powder sample was ground with anhydrous KBr in a mortar. This mixture was compressed to form a pellet for FTIR experiments. The analysis covered a wavenumber range of 4000 - 400 cm^{-1} with 64 scans.

3.2.3 Solid-state nuclear magnetic resonance spectroscopy

The solid-state ^{11}B magic angle spinning (MAS) nuclear magnetic resonance (NMR) spectra were recorded on a Varian Direct-Drive VNMRS-600 spectrometer (14.09 T) using a home-built CP/MAS NMR probe for 4 mm outer-diameter zirconia (PSZ) rotors. The spectra employed a spinning frequency of $\nu_{\text{R}} = 12.0$ kHz, a $0.5 \mu\text{s}$ excitation pulse for a ^{11}B rf field strength of $\gamma B_1/2\pi = 68$ kHz, ^1H decoupling during acquisition ($\gamma B_2/2\pi = 45$ kHz), and a relaxation delay of 4 s. The experiments were performed at ambient temperature using the airtight end-capped PSZ rotors packed with the samples in an argon-filled glovebox. Isotropic ^{11}B chemical shifts are relative to neat $\text{F}_3\text{B}\cdot\text{O}(\text{CH}_2\text{CH}_3)$. The spectra were acquired five months after the melt infiltration was conducted.

3.2.4 N_2 adsorption-desorption

Texture parameters of porous materials were characterized by N_2 adsorption-desorption technique using a BELSORP-mini II surface area and pore size analyzer and a Quantachrome autosorb NOVA 2000 automated gas sorption system. Prior to the measurement, the powder sample was degassed at 200 °C under vacuum for 12 h. Adsorption-desorption isotherms were studied in the pressure range of 0-1 p/p_0 at liquid nitrogen temperature. Data were analyzed by t-plot method (de Boer, Linsen, van der Plas, and Zondervan, 1965; Halsey, 2004), the Brunner Emmet Teller (BET) method (Brunauer, Emmett, and Teller, 1938), and the Barrett Joyner Halenda (BJH)

method (Barrett, Joyner, and Halenda, 1951). The highest point of the isotherm measurement (where $p/p_0 \sim 1$) was used to calculate the total volume of the sample.

3.2.5 Thermal analysis

Thermal behavior of hydrogen storage materials was evaluated by differential scanning calorimetry (DSC) using a Netzsch STA449F3 Jupiter apparatus. A powder sample (5 - 10 mg) was packed in Al_2O_3 crucible in the glovebox and transferred to the instrument with minimal exposure to air. The sample was gradually heated from room temperature to 500 °C (5 °C/min) under N_2 flow of 50 mL/min.

Thermal decomposition behaviors of the materials for solid-state batteries were characterized by thermogravimetric analysis (TGA) and DSC using a PerkinElmer STA 6000. The powder sample (~3.5 mg) was loaded into Al_2O_3 crucible and heated to 200 °C (2 °C/min) under 30 mL/min Ar flow. The gases released from the sample were analyzed by mass spectroscopy (MS) using a Hiden Analytical HPR-20 QMS sampling system.

3.2.6 Sievert type apparatus

De/rehydrogenation properties of hydrogen storage materials was studied using a test station automatically controlled by the program developed in a LabVIEW® environment (Thiangviriyā et al., 2019; Thongtan et al., 2018). Hydrogen release and supply during de/rehydrogenation were controlled by the direct-acting plunger solenoid valves (Type 0255, Bürkert) and the system pressures were detected by pressure transducers with the operating ranges of 0-1500 and 0-3000 Psig (an OMEGA Engineering PX409-1.5KGI and PX309-3KGI). For the nano LB-MH-AC(2), a mass flow controller (MFC, a Bronkhorst ELFLOW select F-221 M) with the operating flow rate of 0-0.1 standard L/min (SLM), which standard temperature (T_s) and pressure (P_s) were 295.0 K and 1.0167 bar, respectively, was used to measure hydrogen content released upon the dehydrogenation. In the case of the TiF_4 -CNT-MH, the MFC (a Bronkhorst ELFLOW selected F-201CV) with the operating range of 0-2 SLM, which T_s and P_s of 294.15 K and 1.0085 bar, respectively, was used. The signals of temperature, pressure, and mass flow rate were transferred to the computer using the module data loggers

(a NI USB-6009, National Instruments and an AI210, Wisco). Hydrogenation of the TiF₄-CNT-MH was done under isothermal condition at the setting temperature (T_{set}) of 250 °C and under 10-15 bar H₂. Dehydrogenation was carried out at different T_{set} (300-340 °C) and H₂-FR (0.6-1.0 SLM), started at the initial pressure ~15 bar H₂, remaining after hydrogenation. The volume of hydrogen desorbed (SL) was calculated by integrating the peak area of the H₂-FR (SLM) versus time (min) plots. Total hydrogen storage capacity, i.e., the combination of material capacity and hydrogen content remaining after hydrogenation were calculated by the following equations.

$$V_{STP} = \frac{P_s V_s T_{STP}}{T_s P_{STP}} \quad (3.1)$$

$$V_{H_2} = \frac{V_{STP}}{22.4 \text{ L/mol}} \quad (3.2)$$

$$H_2 \text{ capacity (wt \%)} = \frac{n_{H_2} \times 2.016 \text{ g/mol}}{\text{sample weight}} \times 100 \quad (3.3)$$

Where V_{STP} (L) and V_s (SL) are volumes of hydrogen gas at the standard temperature and pressure condition (STP, $T_{STP} = 273.15 \text{ K}$ and $P_{STP} = 1.0133 \text{ bar}$) and at the standard condition of MFC, respectively. n_{H_2} (mol) is hydrogen moles and standard molar volume is 22.4 L/mol.

3.2.7 Rate-limiting step determination

Rate-limiting step and kinetic behaviors during dehydrogenation of TiF₄-CNT-MH in laboratory and tank scales were investigated using a reduced time method proposed by Sharp and Jones (Jones, Dollimore, and Nicklin, 1975; Sharp, Brindley, and Achar, 1966). The results were revealed by the plots of the theoretical reduced time ($(t/t_{0.5})_{theoretical}$) versus the experimental reduced time ($(t/t_{0.5})_{experimental}$). The $(t/t_{0.5})_{theoretical}$ was derived from the integral form of kinetic models (**Error! Reference source not found.**), which $t_{0.5}$ was the time at the hydrogen fraction (α) = 0.5. For example, $(t/t_{0.5})_{theoretical}$ of the D1 model ($\alpha^2 = kt$) was expressed as $\alpha^2/0.5^2$. The $(t/t_{0.5})_{experimental}$ was achieved from the experiments by dividing the measurement time

(t) over the time at $\alpha = 0.5$ (Atilio Puszkiel, 2019). The best fitted model was confirmed by three parameters of fitting quality, slope, and y-intercept.

Table 3.2 Gas-solid kinetic models for fitting the experimental data during dehydrogenation.

Models	Description	$g(\alpha)=kt$
Diffusion models		
D1 (1-D diffusion)	Surface control (Chemisorption)	α^2
D2 (2-D diffusion)	Two-dimensional diffusion-controlled growth with decreasing interface rate	$[(1-\alpha)\ln(1-\alpha)]+\alpha$
D3 (3-D diffusion)	Three-dimensional diffusion-controlled growth with decreasing interface rate (Jander equation)	$[1-(1-\alpha)^{1/3}]^2$
D4 (3-D diffusion)	Three-dimensional diffusion-controlled growth with decreasing interface rate (Ginstling-Braunstein equation)	$1-(2/3)\alpha - (1-\alpha)^{2/3}$
Geometrical contraction models		
R2 (Contracting area, CA, n=2)	Two-dimensional growth of contracting volume with constant interface rate	$1-(1-\alpha)^{1/n}$
R3 (Contracting volume, CV, n=3)	Three-dimensional growth of contracting volume with constant interface rate	
Nucleation and growth models		
A2 (JMA, n=2)	Two-dimensional growth of existing nuclei at constant interface rate	$[-\ln(1-\alpha)]^{1/n}$
A3 (JMA, n=3)	Three-dimensional growth of existing nuclei at constant interface rate	

3.2.8 Electrochemical impedance spectroscopy

Electrochemical impedance spectroscopy (EIS) data of materials for solid-state batteries were collected using a BioLogic MTZ-35 impedance analyzer equipped with a high-temperature sample holder. The powder sample was compacted at a pressure

of 0.75 GPa for 5 min using a die set with 5 mm diameter in the glovebox. Impedance data were measured in a frequency range from 10 MHz to 1 Hz with an amplitude of 10 mV in the temperature range from RT to 80 °C. EIS data were analyzed with the MT-Lab software, and all activation energies were extracted from $\ln(\sigma T)$ vs $T^{-1}(K^{-1})$ plots of the data collected during the second heating cycle.

3.3 References

- Atilio Puzkiel, J. (2019). Tailoring the Kinetic Behavior of Hydride Forming Materials for Hydrogen Storage. In M. Rahman and A. Mohammed Asiri (Eds.), *Gold Nanoparticles—Reaching New Heights*. IntechOpen. <https://doi.org/10.5772/intechopen.82433>
- Barrett, E. P., Joyner, L. G., and Halenda, P. P. (1951). The Determination of Pore Volume and Area Distributions in Porous Substances. I. Computations from Nitrogen Isotherms. *Journal of the American Chemical Society*, 73(1), 373–380. <https://doi.org/10.1021/ja01145a126>
- Brunauer, S., Emmett, P. H., and Teller, E. (1938). Adsorption of Gases in Multimolecular Layers. *Journal of the American Chemical Society*, 60(2), 309–319. <https://doi.org/10.1021/ja01269a023>
- de Boer, J. H., Linsen, B. G., van der Plas, Th., and Zondervan, G. J. (1965). Studies on pore systems in catalysts: VII. Description of the pore dimensions of carbon blacks by the t method. *Journal of Catalysis*, 4(6), 649–653. [https://doi.org/10.1016/0021-9517\(65\)90264-2](https://doi.org/10.1016/0021-9517(65)90264-2)
- Filinchuk, Y., Richter, B., Jensen, T. R., Dmitriev, V., Chernyshov, D., and Hagemann, H. (2011). Porous and Dense Magnesium Borohydride Frameworks: Synthesis, Stability, and Reversible Absorption of Guest Species. *Angewandte Chemie International Edition*, 50(47), 11162–11166. <https://doi.org/10.1002/anie.201100675>
- Halsey, G. (2004). Physical Adsorption on Non-Uniform Surfaces. *The Journal of Chemical Physics*, 16(10), 931–937. <https://doi.org/10.1063/1.1746689>
- Jones, L. F., Dollimore, D., and Nicklin, T. (1975). Comparison of experimental kinetic decomposition data with master data using a linear plot method.

Thermochimica Acta, 13(2), 240–245. [https://doi.org/10.1016/0040-6031\(75\)80085-2](https://doi.org/10.1016/0040-6031(75)80085-2)

Sharp, J. H., Brindley, G. W., and Achar, B. N. N. (1966). Numerical Data for Some Commonly Used Solid State Reaction Equations. *Journal of the American Ceramic Society*, 49(7), 379–382. <https://doi.org/10.1111/j.1151-2916.1966.tb13289.x>

Thiangviriyaya, S., Plerdsranoy, P., Sitthiwet, C., Dansirima, P., Thongtan, P., Eiamlamai, P., ... Utke, R. (2019). MgH₂-TiF₄-MWCNTs based hydrogen storage tank with central tube heat exchanger. *International Journal of Hydrogen Energy*, 44(36), 20173–20182. <https://doi.org/10.1016/j.ijhydene.2019.06.002>

Thongtan, P., Dansirima, P., Thiangviriyaya, S., Thaweelap, N., Suthummapiwat, A., Plerdsranoy, P., and Utke, R. (2018). Reversible hydrogen sorption and kinetics of hydrogen storage tank based on MgH₂ modified by TiF₄ and activated carbon. *International Journal of Hydrogen Energy*, 43(27), 12260–12270. <https://doi.org/10.1016/j.ijhydene.2018.04.171>

Yan, Y., Grinderslev, J. B., Jørgensen, M., Skov, L. N., Skibsted, J., and Jensen, T. R. (2020). Ammine Magnesium Borohydride Nanocomposites for All-Solid-State Magnesium Batteries. *ACS Applied Energy Materials*, 3(9), 9264–9270. <https://doi.org/10.1021/acsaem.0c01599>

The Center of Excellence in Biomass: BIOMASS SUT. (n.d.). Retrieved November 6, 2023, from <https://biomass.sut.ac.th/biomass/biomass/>

CHAPTER IV

RESULTS AND DISCUSSION

4.1 Solid-state hydrogen storage

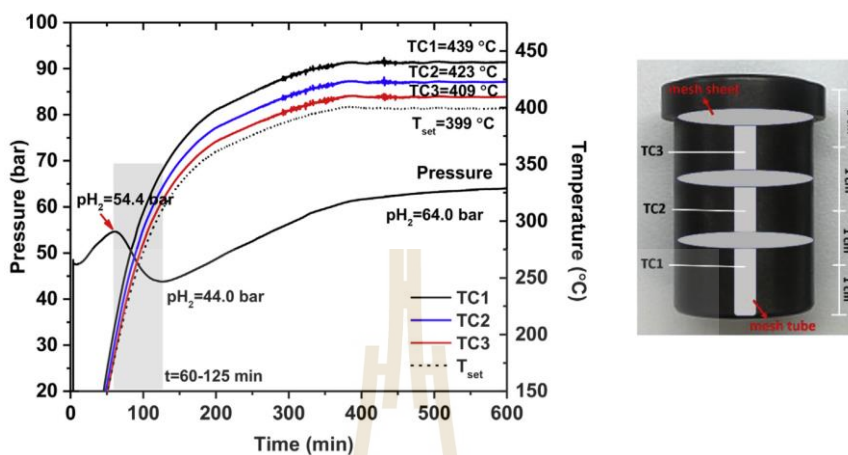
4.1.1 Nano LB-MH-AC-based small hydrogen storage tank

Texture parameters of activated carbon (AC) are investigated by N_2 adsorption-desorption technique. The surface area, pore size, and pore volume of the AC are $690 \text{ m}^2/\text{g}$, 2.80 nm , and 0.50 mL/g , respectively. The synthesis of nano LB-MH-AC(1) involves the simultaneous processes of hydrogenation of Mg to MgH_2 and melt infiltration of $2LiBH_4$ - MgH_2 into the pores of AC. This is achieved by heating a mixture of $LiBH_4$, Mg, and AC in a small cylindrical tank (Figure 3.1) to $T_{\text{set}}=400 \text{ }^\circ\text{C}$ under 40-50 bar H_2 (Figure 4.1(A)). The hydrogen pressure of $\sim 48 \text{ bar } H_2$ is applied to the tank at room temperature to prevent the decomposition of $LiBH_4$. Upon heating, at $t=60 \text{ min}$ and $T \sim 150 \text{ }^\circ\text{C}$, system pressure increases to $54.4 \text{ bar } H_2$ due to thermal expansion. Significant reduction of system pressure to $44 \text{ bar } H_2$ at $186\text{-}342 \text{ }^\circ\text{C}$ ($t=60\text{-}125 \text{ min}$) indicates the hydrogenation of Mg to form MgH_2 (Eq.(4.1)). This is possibly due to the system pressure exceeding the equilibrium pressure of MgH_2 at $186\text{-}342 \text{ }^\circ\text{C}$ ($P_{\text{eq}} < 10 \text{ bar } H_2$) (Bösenberg et al., 2010). The system pressure then increases to $64.0 \text{ bar } H_2$ at $T=409\text{-}439 \text{ }^\circ\text{C}$ (Figure 4.1(A)), attributed to thermal expansion and partial dehydrogenation of $LiBH_4$, confirmed by PXD and FTIR results (Figure 4.1(B) and (C)). Notice that the temperature inside the tank varies with depth due to the low thermal conductivity of the material and differences in positions within the furnace.

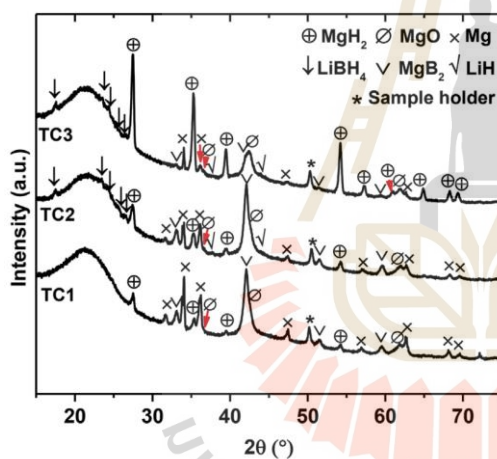
To analyze the chemical compositions of nano LB-MH-AC(1), the powder samples at different depths (TC1-TC3) are characterized using PXD and FTIR techniques. The PXD signals of all samples show comparable phase compositions of MgH_2 , MgB_2 , MgO , Mg, and LiH (Figure 4.1(B)). The disappearance of $LiBH_4$ diffraction suggests the amorphous state and/or nanoparticle formation due to nanoconfinement (Surrey et al., 2016; Zhai et al., 2016). The relative content of MgH_2 to Mg decreases with the tank depth, while that of MgB_2 to Mg increases. These indicate that the hydrogenation of

Mg to MgH_2 (Eq. (4.1)) is favored at relatively low temperature (TC3), while the reaction between LiBH_4 and Mg (Eq. (4.2)) prefers higher temperature (TC1-TC2).

(A)



(B)



(C)

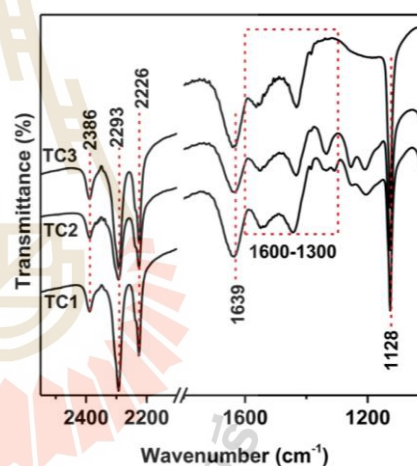
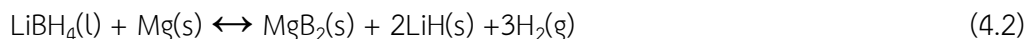


Figure 4.1 Hydrogenation profile ($T_{\text{set}}=400$ °C and $p(\text{H}_2)=40\text{-}50$ bar)(A) and positions of TC1-TC3 in the tank as well as PXD (B) and FTIR (C) spectra of nano LB-MH-AC(1).

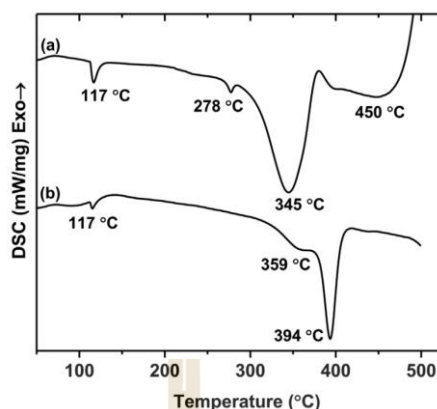
Furthermore, FTIR analysis of nano LB-MH-AC(1) reveals B-H stretching and bending of LiBH_4 at $2386\text{-}2226$ and 1128 cm^{-1} , respectively (Zhai et al., 2016; Zhao et al., 2017), as well as O-H bending at 1639 cm^{-1} from air and/or moisture contamination (Figure 4.1(C)). Asymmetric B-O stretching at $1600\text{-}300$ cm^{-1} , due to oxidation of amorphous boron, one of the dehydrogenation products of LiBH_4 (Eq.(4.3)), is also detected (Bösenberg et al., 2010; Kamitsos, Karakassides, and Chryssikos, 1987).



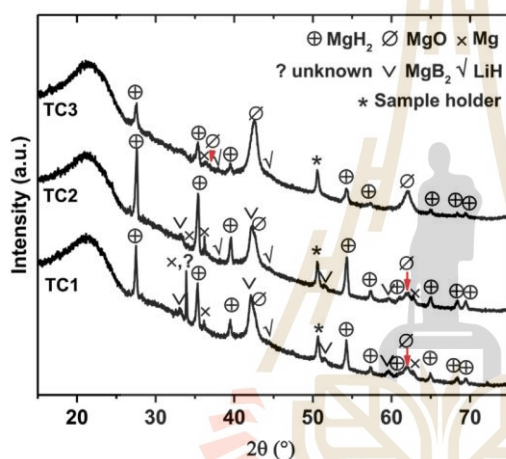


The hydrogenation of Mg and nanoconfinement are further developed by rehydrogenation nano LB-MH-AC(1) under 40-50 bar H₂ at a lower temperature of 350 °C, denoted as nano LB-MH-AC(2). The successful nanoconfinement of 2LiBH₄-MgH₂ into the porous structure of AC is confirmed by DSC analyses of the samples collected at different positions in the tank (Figure 4.2(A)(a)). The endothermic peaks at 117–278 °C indicate *o*-to *h*-LiBH₄ phase transformation and melting of *h*-LiBH₄ along with the two-step dehydrogenation of nanoconfined 2LiBH₄-MgH₂ (and MgH₂) and pristine LiBH₄ at 345 and 450 °C, respectively. The occurrence of LiBH₄ decomposition at high temperature (T=450 °C) indicates incomplete nanoconfinement of LiBH₄ into the AC. In contrast, another sample shown in (Figure 4.2(A)(b)) exhibits the *o*-to *h*-LiBH₄ phase transformation and the dehydrogenation of 2LiBH₄-MgH₂ (and MgH₂) at 117 and 359-394 °C, respectively. The absence of characteristic peaks associated with *h*-LiBH₄ melting and decomposition of pristine LiBH₄ suggests complete nanoconfinement of LiBH₄ (Figure 4.2(A)(b)). Moreover, the phase compositions of nano LB-MH-AC(2) are examined by using PXD and FTIR techniques. Figure 4.2(B) demonstrates comparable diffraction patterns of MgH₂, Mg, and MgO in the samples from all positions (TC1-TC3). The increase of relative content of MgH₂ in all samples suggests the improved hydrogenation. However, the signal of MgB₂ is still observed in the samples at high-temperature positions (TC1-TC2) together with unknown phase at TC1 (Figure 4.2(B)). Regarding FTIR results, nano LB-MH-AC(2) exhibits vibrational peaks associated with B-H stretching and bending of LiBH₄ (2392-2224 and 1124 cm⁻¹, respectively), O-H bending from air and moisture contamination (1634 cm⁻¹), and asymmetric B-O stretching of amorphous boron (**α**-B) (1600-1300 cm⁻¹), which is comparable to nano LB-MH-AC(1) (Figure 4.2(C)).

(A)



(B)



(C)

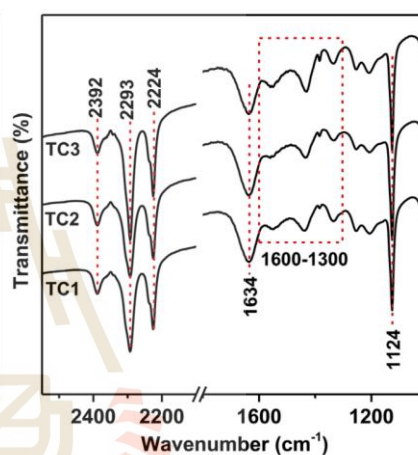


Figure 4.2 DSC curves of the powder samples randomly collected from the tank (A) as well as PXD (B) and FTIR (C) spectra of nano LB-MH-AC(2).

Furthermore, dehydrogenation of LB-MH-AC(2) was conducted under isothermal conditions ($T_{\text{set}}=348\text{ °C}$) with an initial pressure of around 40 bar H_2 , remaining from previous hydrogenation (Figure 4.3). To initiate dehydrogenation, the hydrogen pressure is released through MFC at the constant flow rate of 0.1 SLM. Dehydrogenation, indicated by the endothermic process at TC1-TC3, starts at $t\sim 12$ min under $p(\text{H}_2)=12.5$ bar (Figure 4.3). The hydrogen flow rate remains constant for 30 min and gradually decreases until dehydrogenation completes within ~ 70 min. These align with the elevated temperatures at TC1-TC3. The total hydrogen released content and storage capacity are 4.04 SL and 4.55 wt.% H_2 , respectively. The hydrogen content from the remaining pressure (~ 40 bar H_2) are 1.14 SL and 1.27 wt.% H_2 , respectively. The material storage capacity of the tank is 3.28 wt.% H_2 , corresponding to 58% of the

theoretical storage capacity of material (5.7 wt.% H₂). It is noteworthy that the dehydrogenation rate is enhanced at high temperatures. For instance, suggests effective dehydrogenation at TC1 is found at t=24 min, indicated by a greater peak area of the endothermic event. In contrast, at TC2 and TC3, the events shift to 28-29 min accompanied with reduced peak area (Figure 4.3).

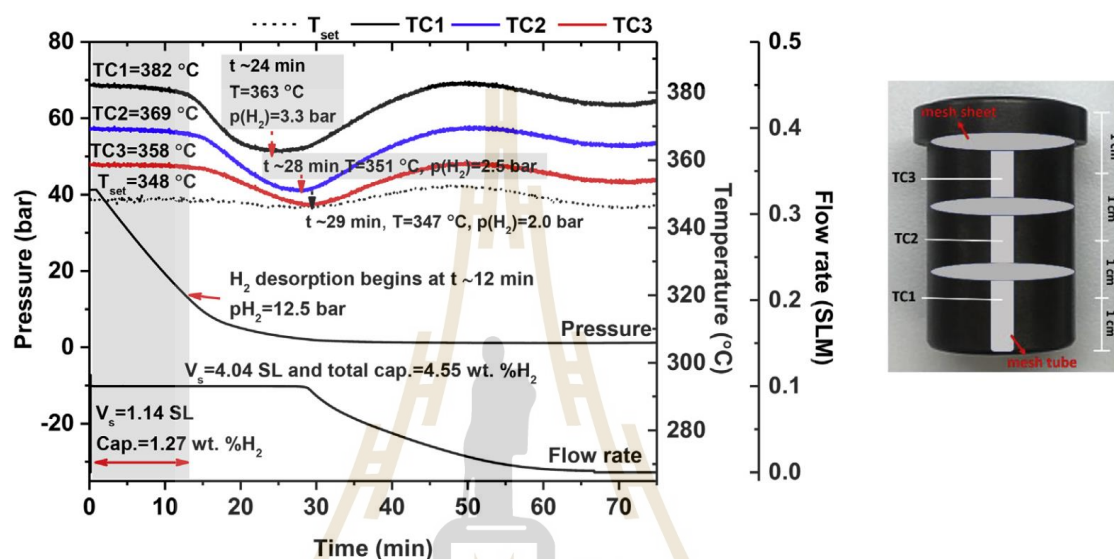


Figure 4.3 The 1st dehydrogenation profile of LB-MH-AC(2) at $T_{\text{set}}=350$ °C.

Furthermore, phase compositions of dehydrogenated LB-MH-AC(2) at TC1-TC3 are examined using PXD and FTIR techniques (Figure 4.4(A) and (B)). Dehydrogenated samples at all positions exhibit comparable diffraction patterns of Mg, MgB₂, LiH, and MgO along with unknown phase at TC3 (Figure 4.4(A)). From FTIR results, all samples display vibrational peaks associated with B-H stretching and bending of LiBH₄ (2388-2224 and 1128 cm⁻¹, respectively), O-H bending from air and moisture contamination (1634 cm⁻¹), asymmetric B-O stretching of amorphous boron (α -B) (1600-1300 cm⁻¹), and [B₁₂H₁₂]²⁻ of Li₂B₁₂H₁₂ (2484 cm⁻¹) (Figure 4.4(B)). The formations of LiH, α -B, and Li₂B₁₂H₁₂ are from individual dehydrogenation of LiBH₄ according to Eq. (4.3) and Eq. (4.4). In agreement with the previous report on de/rehydrogenation pathways and thermodynamic properties of 2LiBH₄-MgH₂ (Cova, Rönnebro, Choi, Gennari, and Larochette, 2015). Two-step decomposition at 360-380 °C following the reverse reactions of Eq. (4.1) and Eq. (4.2) is detected at high and low pressure, respectively.

Thus, at TC1-TC3 (T=358-382 °C), the reaction pathway begins with the dehydrogenation of MgH₂ to produce Mg (reverse Eq. (4.1)), which further reacting with LiBH₄ to form LiH and MgB₂ (Eq. (4.2)). Additionally, it was reported that the decomposition pathway following Eq. (4.2) is effective at high temperature (Cova et al., 2015). Therefore, MgB₂ formation is effective at TC1 (T=382 °C) and reduces at low-temperature positions of TC2 and TC3 (T=369 and 358 °C, respectively) (Figure 4.3). This is consistent with the significant relative content of MgB₂ to Mg at TC1 compared to TC2 and TC3 (Figure 4.4(A)). Moreover, the rapid decrease in system pressure due to the fast hydrogen release rate during dehydrogenation results in improper conditions for MgB₂ formation, which requires hydrogen back pressure of 3-5 bar (Bösenberg et al., 2010). From Figure 4.3, the hydrogen pressure at the main dehydrogenation peak at TC1 (T=363 °C) is 3.3 bar, while those at TC2 (T=351 °C) and TC3 (T=347 °C) are 2.5 and 2.0 bar, respectively. This results in the greater MgB₂ formation at TC1 than TC2-TC3.

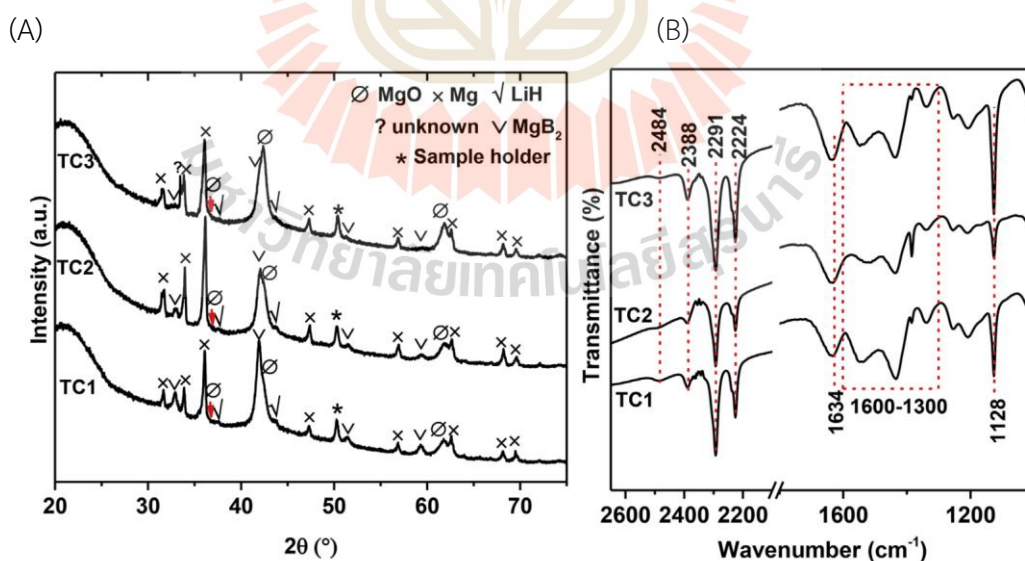
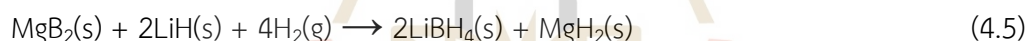


Figure 4.4 The PXD (A) and FTIR (B) spectra of dehydrogenated LB-MH-AC(2) at TC1-TC3.

Afterwards, rehydrogenation is conducted under isothermal conditions ($T_{\text{set}}=350\text{ }^{\circ}\text{C}$) under pressure of 30-40 bar H_2 (Figure 4.5). By initiating the process with an initial hydrogen pressure of 40 bar, temperatures at all positions rapidly rise to equilibrium temperatures (T_{eq}) of 445-414 $^{\circ}\text{C}$ (TC1-TC3), indicating rapid hydrogenation rate with low heat transfer (Thongtan et al., 2018). At $T_{\text{eq}} > 400\text{ }^{\circ}\text{C}$, hydrogenation of the $2\text{LiBH}_4\text{-MgH}_2$ composite, following (4.1) and reverse Eq. (4.2), proceeds at high and low pressures, respectively (Cova et al., 2015). The hydrogenation of Mg to MgH_2 Eq. (4.1) might be represented by peak (a) ($T_{\text{eq}}=445\text{-}414\text{ }^{\circ}\text{C}$) observed at high pressure, while that of $\text{MgB}_2\text{-LiH}$, producing LiBH_4 and Mg (reverse Eq. (4.2)) at lower pressure, belongs to the shoulder peaks (b). It is noteworthy that the reversibility of LiBH_4 (peak (b)) is significant at high temperature (TC1) and reduces with temperature (TC2-TC3). Once the hydrogen pressure reduces to 30 bar, a new hydrogenation cycle is initiated by increasing the system pressure to 40 bar.

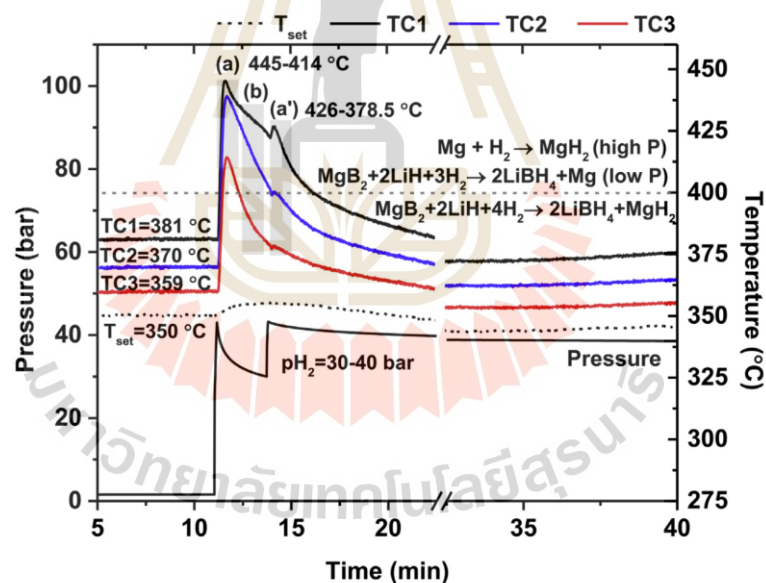


Figure 4.5 Rehydrogenation profile ($T_{\text{set}}=350\text{ }^{\circ}\text{C}$ and $p(\text{H}_2)=30\text{-}40\text{ bar}$) of LB-MH-AC(2).

However, the T_{eq} of the subsequent hydrogen filling cycle decreases to 426-378.5 $^{\circ}\text{C}$ (TC1-TC3) (Figure 4.5). At $T_{\text{eq}} > 400\text{ }^{\circ}\text{C}$ (TC1), the hydrogenation mechanisms follow a comparable reaction pathway as the previous hydrogen filling cycle; however, only the first peak (a'), corresponding to the hydrogenation of Mg (Eq. (4.1)), is achieved. Therefore, Mg formed during the first hydrogen filling cycle (reverse Eq. (4.2)) can be completely hydrogenated in this cycle. For TC2-TC3 ($T_{\text{eq}} < 400\text{ }^{\circ}\text{C}$), hydrogen absorption

of $\text{MgB}_2\text{-LiH}$ according to Eq. (4.5) can be achieved to form LiBH_4 and MgH_2 (Cova et al., 2015). After $t=20$ min, temperatures at all positions decrease to the initial values, indicating the end of the hydrogenation.

Subsequently, the second dehydrogenation is conducted under conditions comparable to the first cycle, $T_{\text{set}}=350$ °C and initial pressure of ~ 40 bar H_2 . The hydrogen mass flow rate is reduced to 0.8 SLM to enhance the hydrogen back pressure during dehydrogenation, promoting MgB_2 formation (Figure 4.6). The system pressure gradually decreases until dehydrogenation initiates at $t \sim 18$ min under 10.1 bar H_2 , marked by the endothermic event at TC1. The hydrogen flow rate remains constant at 0.8 SLM for 32 min and gradually decreases until complete hydrogenation within 65 min. The total hydrogen content released and storage capacity are 3.31 SL and 4.06 wt.% H_2 , respectively, while those remaining after the previous hydrogenation are 1.44 SL and 1.77 wt.% H_2 , respectively. Consequently, the material capacity during the 2nd cycle is 2.29 wt.% H_2 , corresponding to 40% of the theoretical capacity of nano LB-MH-AC(2). The deficiency in reversible hydrogen content may be attributed to the formation of the thermally stable phase of $\text{Li}_2\text{B}_{12}\text{H}_{12}$, further confirmed by FTIR results (Figure 4.8(B)), and incomplete dehydrogenation of LiBH_4 , similar to the first cycle (Figure 4.4(B)). The reaction rate increases with temperature. For instance, the main endothermic peak at TC1 ($T=364$ °C) is detected at $t=28$ min, while those at TC2-TC3 ($T=353\text{-}348$ °C) delay to $t=33\text{-}35$ min. Due to the faster reaction rate, the hydrogen back pressure at the main dehydrogenation peak at TC1 (3.6 bar H_2) is greater than those at TC2-TC3 (1.7-1.4 bar H_2), resulting in effective MgB_2 formation.

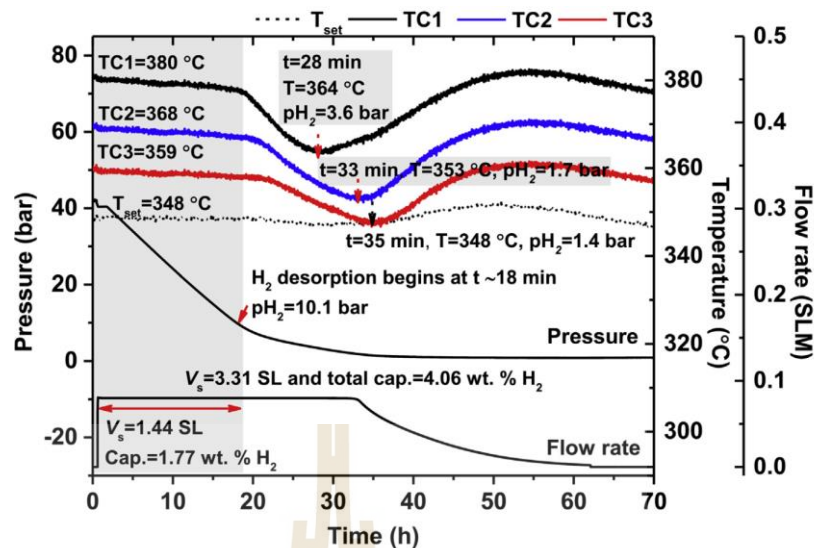


Figure 4.6 The 2nd dehydrogenation ($T_{\text{set}}=350\text{ }^{\circ}\text{C}$) of LB-MH-AC(2).

Additionally, investigation on the total and material hydrogen storage capacities, kinetics, and reversibility of LB-MH-AC(2) are conducted. The total storage capacities of 3.56-4.55 wt.% H_2 is observed upon five de/rehydrogenation cycles (Figure 4.7). Regarding material storage capacity, the hydrogen content of 3.28 wt.% H_2 is released within 50 min during the 1st cycle. While the subsequent 2nd-4th cycles exhibit comparable capacities of 2.03 to 2.29 wt.% H_2 within 30 min.

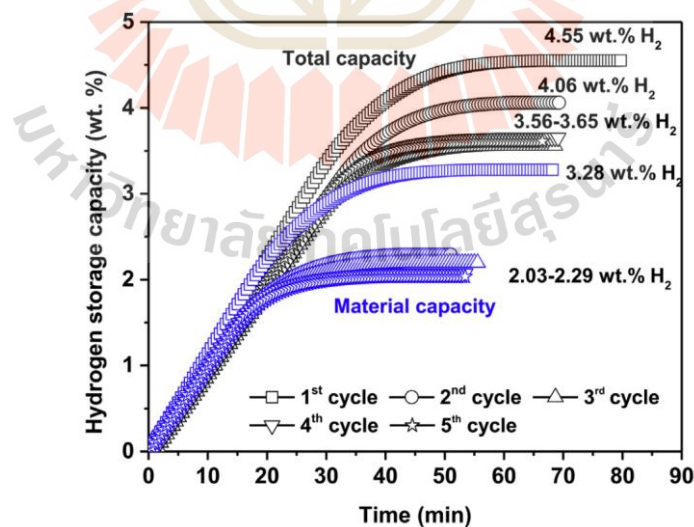


Figure 4.7 Dehydrogenation kinetics and reversibility upon five hydrogen release and uptake cycles of hydrogen storage tank.

The phase compositions of the 5th hydrogenated samples at TC1-TC3 are analyzed using PXD and FTIR techniques. From Figure 4.8(A), all samples exhibit comparable diffractions of MgH₂, Mg, MgO, and LiH. For B-containing phases, FTIR results for all hydrogenated samples show vibrational peaks of B-H stretching and bending of LiBH₄ (2390-2226 and 1128 cm⁻¹, respectively), O-H bending related to oxygen and humidity contamination (1634 cm⁻¹), asymmetric B-O stretching due to the oxidation of a-B (1600-1300 cm⁻¹), and [B₁₂H₁₂]²⁻ vibration of Li₂B₁₂H₁₂ (2488 cm⁻¹) (Figure 4.8(B)). The present of MgH₂ confirms its reversibility upon five de/rehydrogenation cycles, while that of LiBH₄ can be due to both reversibility and incomplete dehydrogenation from the previous cycles. The signals of Mg and LiH suggest partial irreversibility of MgH₂ and LiBH₄, respectively. Notably, the vibrational peak of Li₂B₁₂H₁₂ is more pronounced in the 5th cycle (Figure 4.8(B)) compared to the 1st one (Figure 4.4(B)), explaining the deficient hydrogen content reproduced during the 2nd-4th cycles Figure 4.7. Regarding the various reaction pathways during de/rehydrogenation of the nanoconfined 2LiBH₄-MgH₂ system, the application of a suitable temperature-pressure pair to the tank enables controllable reaction mechanisms, favoring kinetics and reversibility. Additionally, the consideration of good thermal conductivity in materials, advanced temperature control system to suppress temperature gradients inside the tank, and enhanced hydrogen gas permeability through the sample bulk are essential for the further development of a hydrogen storage tank based on nanoconfined 2LiBH₄-MgH₂.

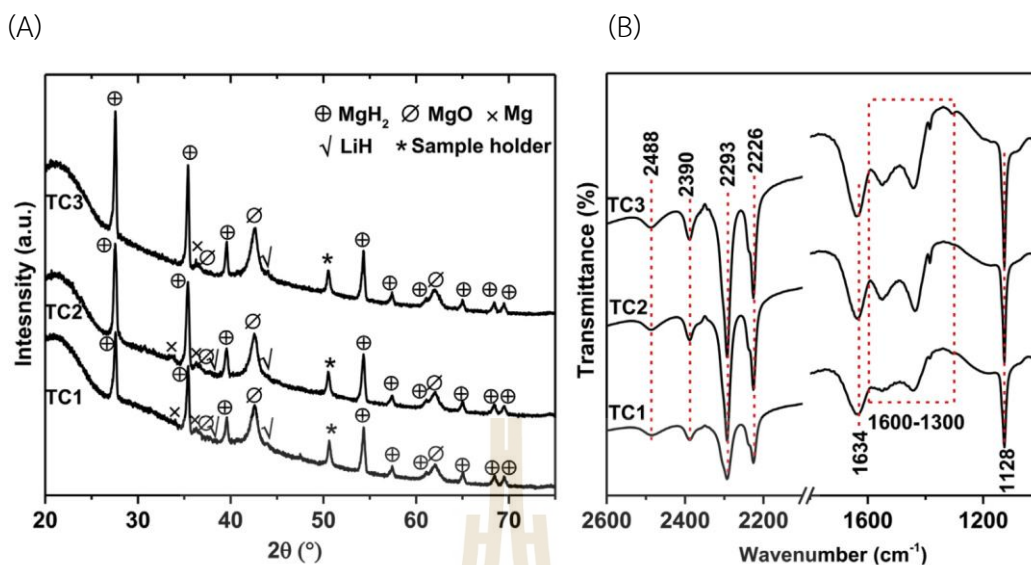


Figure 4.8 PXD (A) and FTIR (B) spectra of the 5th hydrogenated samples at TC1-TC3.

In conclusion, the investigation focuses on examining the pathways and efficiency of nanoconfined $2\text{LiBH}_4\text{-MgH}_2$ within AC in a small hydrogen storage container with a volume of 21.7 mL. Hydrogenation of Mg into MgH_2 and confinement of $2\text{LiBH}_4\text{-MgH}_2$ into AC are achieved by heating the mixture of LiBH_4 , Mg, and AC to $T = 350\text{-}400\text{ }^\circ\text{C}$ under 40 to 50 bar H_2 pressure. Throughout five de/rehydrogenation cycles, the overall hydrogen storage capacities are 3.56 to 4.55 wt.% H_2 . Specifically, the capacities from hydride materials are 2.03 to 3.28 wt.% H_2 , accounting for 36-58% of the theoretical capacity. The deficient observed hydrogen contents are attributed to the partial decomposition of LiBH_4 during sample preparation, incomplete dehydrogenation of LiBH_4 , and the formation of thermally stable $\text{Li}_2\text{B}_{12}\text{H}_{12}$ during cycling.

The de/rehydrogenation processes reveal various reaction pathways under distinct temperature and pressure conditions within the container. During dehydrogenation in the temperature range of $358\text{-}382\text{ }^\circ\text{C}$, the two-step reaction involving $\text{MgH}_2 / \text{Mg} + \text{H}_2$ and $\text{Mg} + \text{LiBH}_4 / \text{MgB}_2 + \text{LiH} + 3\text{H}_2$ occurs at high and low pressure, respectively. The formation of MgB_2 , promoting reversibility, is more effective in regions with high temperatures and appropriate back hydrogen pressure (3.3–3.6 bar H_2). For rehydrogenation, at $T > 400\text{ }^\circ\text{C}$ under 30-40 bar H_2 , the absorption of Mg to form MgH_2 is observed at high pressure, while the conversion of $\text{MgB}_2 + \text{LiH}$ into LiBH_4

+ Mg occurs at lower pressure. At $T < 400\text{ }^{\circ}\text{C}$, the hydrogenation of $\text{MgB}_2 + \text{LiH}$ to produce $\text{LiBH}_4 + \text{MgH}_2$ is achieved.

4.1.2 TiF_4 -CNT-MH-based hydrogen storage tank

Phase compositions of TiF_4 -CNT-MH sample are confirmed by PXD technique. The diffractions of β - and γ - MgH_2 , Mg, MgO , and an unidentified phase are found (Figure 4.9(A)). The significant relative content of MgH_2 to Mg indicates the successful hydrogenation of Mg to MgH_2 . The appearance of MgO suggests the oxidation of Mg-containing phases due to exposure to air and/or moisture during PXD experiments. Before the kinetic studies, TiF_4 -CNT-MH (45.2252 g) is stabilized by subjecting the material packed into the hydrogen storage tank (Figure 3.3 (A)) to nine cycles of hydrogen desorption ($T_{\text{set}}=300\text{ }^{\circ}\text{C}$ at 1.0 SLM) and absorption ($T_{\text{set}}=250\text{ }^{\circ}\text{C}$ under 10-15 bar H_2). As shown in Figure 4.9(B), TiF_4 -CNT-MH exhibits cycling stability over nine de/rehydrogenation cycles, with average total and material hydrogen storage capacities of 5.05 and 4.85 wt.% H_2 , respectively.

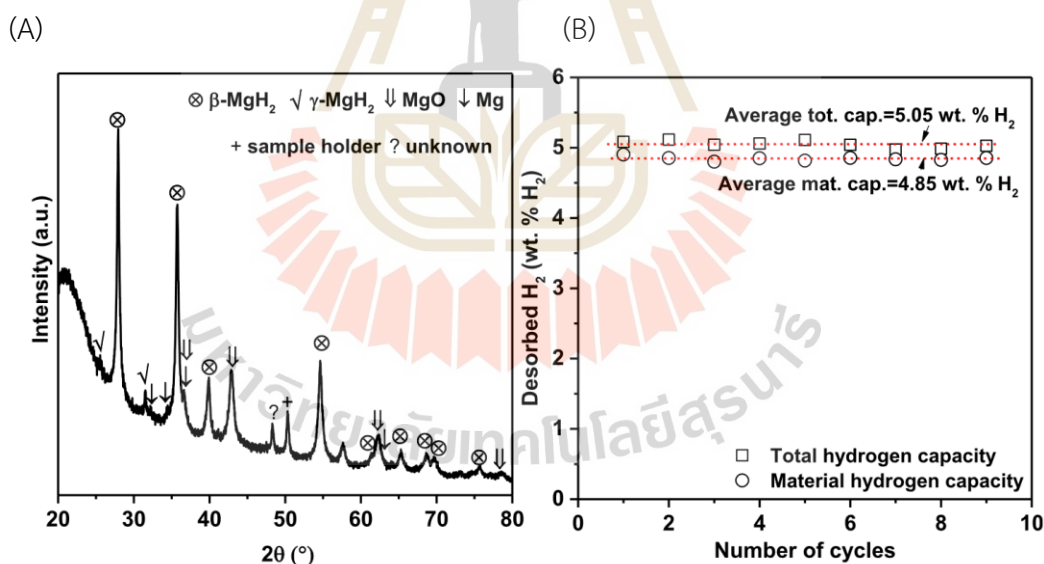


Figure 4.9 PXD pattern (A) and hydrogen capacities upon de/rehydrogenation cycles (B) of as-prepared TiF_4 -CNT-MH.

Dehydrogenation kinetics of the stabilized TiF_4 -CNT-MH is investigated at different operating temperatures and H_2 -FR, both in laboratory and tank scales. In the laboratory scale, 1.8320 g of TiF_4 -CNT-MH is packed into the small tank shown in Figure 3.2. The isothermal dehydrogenation is conducted at $T_{\text{set}}=293\text{-}309\text{ }^{\circ}\text{C}$, reaching

comparable sample temperatures (T_{sample}) at 300 °C and H_2 -FR of 0.6 and 1.0 SLM (Figure 4.10(A)). Initial pressure of ~ 15 bar H_2 is applied to prevent dehydrogenation during the heating process. Upon reaching isothermal conditions, dehydrogenation starts, releasing hydrogen gas through MFC (Figure 4.10(A)). Increasing H_2 -FR from 0.6 to 1.0 SLM leads to the enhanced dehydrogenation rate of $\text{TiF}_4\text{-CNT-MH}$, with comparable hydrogen volumes released (0.99-1.02 SL). This results in a total hydrogen capacity of 4.48 wt.% H_2 within 1.85 and 1.20 min for experiments with 0.6 and 1.0 SLM, respectively (Figure 4.10(B)).

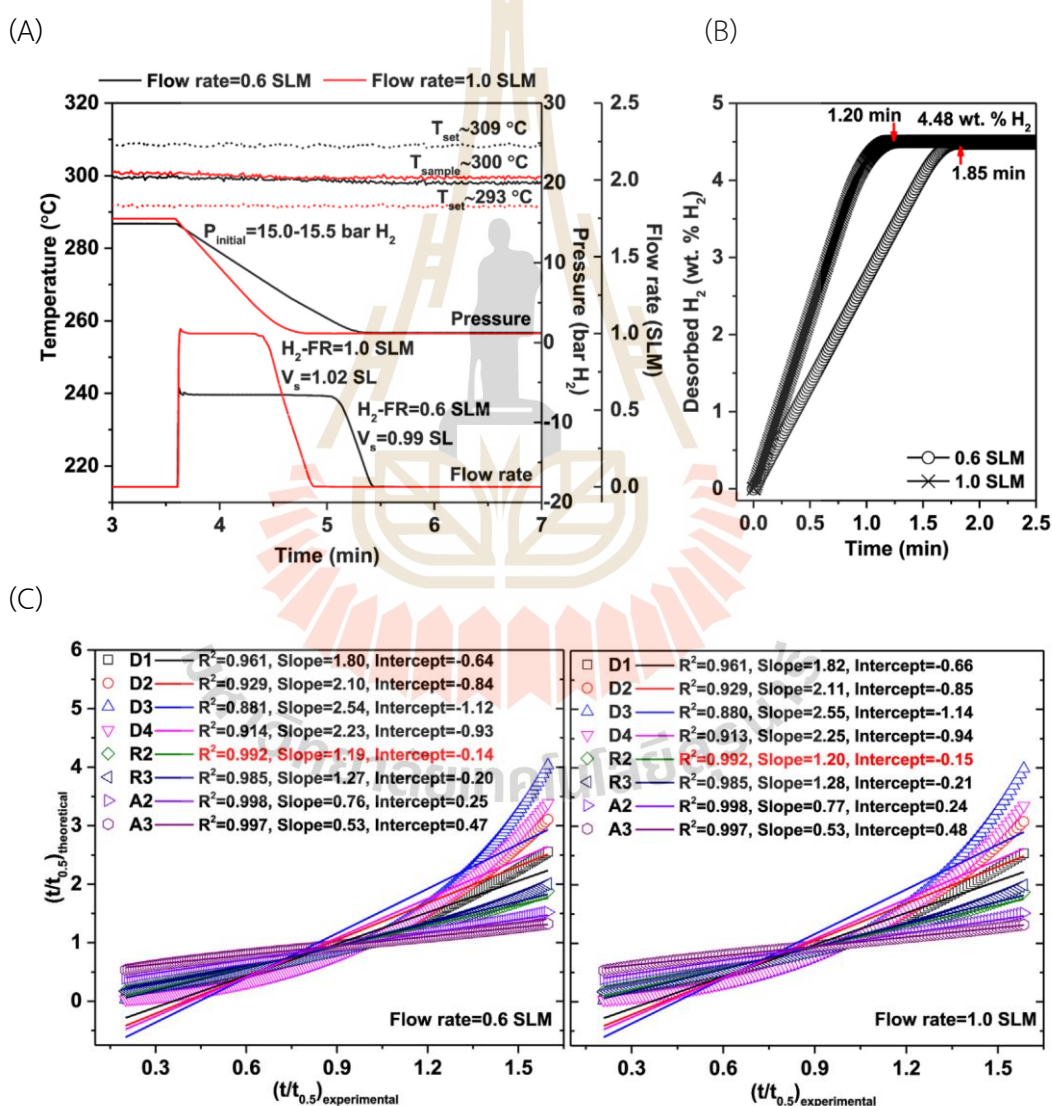


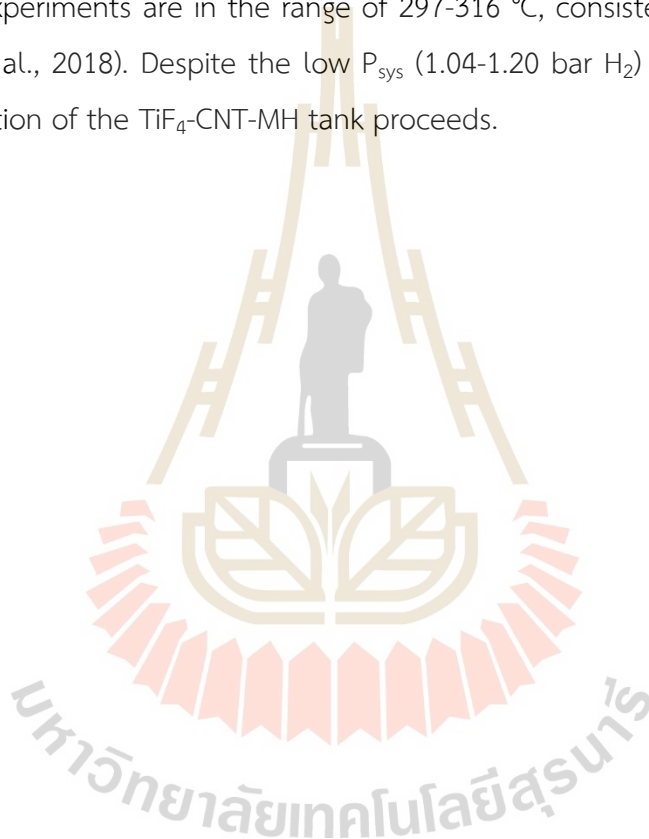
Figure 4.10 Temperature, pressure, and hydrogen mass flow rate profiles (A), kinetics (B), and $(t/t_{0.5})_{\text{theoretical}}$ versus $(t/t_{0.5})_{\text{experimental}}$ plots fitted with different kinetic models

(C) during dehydrogenation with H_2 -FR of 0.6 and 1.0 SLM of TiF_4 -CNT-MH in laboratory scale.

Due to small amount of the powder sample in the laboratory scale (1.8320 g), the endothermic heat is compensated by the external heater, maintaining a constant T_{sample} throughout the dehydrogenation process (Figure 4.10(A)). The rate-limiting step for the dehydrogenation process is investigated using the reduced time method (Jones, Dollimore, and Nicklin, 1975; Sharp, Brindley, and Achar, 1966), plotting $(t/t_{0.5})_{theoretical}$ versus $(t/t_{0.5})_{experimental}$ with the desorbed hydrogen fraction (α) in the range of 0.10-0.80, obtained from the kinetic results in Figure 4.10(B). The best fit ($R^2=0.992$, slope ~ 1.2 , and y-intercept ~ 0.15) suggests that the kinetic behavior of TiF_4 -CNT-MH in laboratory scale during dehydrogenation with H_2 -FR of 0.6 and 1.0 SLM is consistent with the geometrical contraction model, with the rate-limiting step being the two-dimensional growth of the contracting volume with a constant interface rate (Figure 4.10(C)). This corresponds to step (i) of the dehydrogenation process, specifically the decomposition of the hydride phase with metal/hydride interface movement (Atilio Puzkiel, 2019). It is noteworthy that the increase in H_2 -FR during the dehydrogenation of TiF_4 -CNT-MH in laboratory scale enhances the reaction rate while maintaining a consistent kinetic behavior and rate-limiting step.

Moreover, we investigate the impact of H_2 -FR (0.6-1.0 SLM) and temperatures (300-340 °C) on the dehydrogenation kinetics of the TiF_4 -CNT-MH tank. The powder sample of 45.2252 g is packed into the tank equipped with external heater and central heat exchanger (Figure 3.3(A)). Temperature sensors (TC1-TC5) are strategically placed, which TC1-TC3 in the axial direction at 24-86 mm from H_2 inlet/outlet and TC2, TC4, and TC5 are in the radial direction at 5-13 mm from the central heat exchanger (Figure 3.3(B)). Dehydrogenations are conducted at comparable $T_{set}=296-298$ °C and initial pressure of ~ 15.0 bar H_2 under H_2 -FR conditions of 0.6-1.0 SLM. From Figure 4.11(A)-(C), the initial temperatures (T_{in}) for all experiments are within the range of 317-342 °C. TC2 records the lowest T_{in} , while TC1 and TC3-TC5 exhibit comparable and higher values than TC2. This variation can be attributed to the longer distance of TC2 from the external heater and its position surrounded by dense hydride powder with low

thermal conductivity. Since the equilibrium pressures (P_{eq}) corresponding to these T_{in} (3-5 bar H_2 (Zhang et al., 2018)) exceed the system pressure (P_{sys}), dehydrogenation is facilitated. The dehydrogenations initiate at onset pressures ($P_{onset\ des}$) ranging from 2.50-2.70 bar H_2 (Figure 4.11(A)-(C)), which are lower than P_{eq} at T_{in} (3-5 bar H_2). Endothermic dehydrogenation is observed at all positions inside the tank, evidenced by temperature reduction, and complete dehydrogenation is confirmed by the subsequent elevation of temperature to T_{in} . The lowest temperatures recorded at TC1-TC5 for all experiments are in the range of 297-316 °C, consistent with $P_{eq}=1.5-3$ bar H_2 (Zhang et al., 2018). Despite the low P_{sys} (1.04-1.20 bar H_2) in comparison to P_{eq} , dehydrogenation of the TiF_4 -CNT-MH tank proceeds.



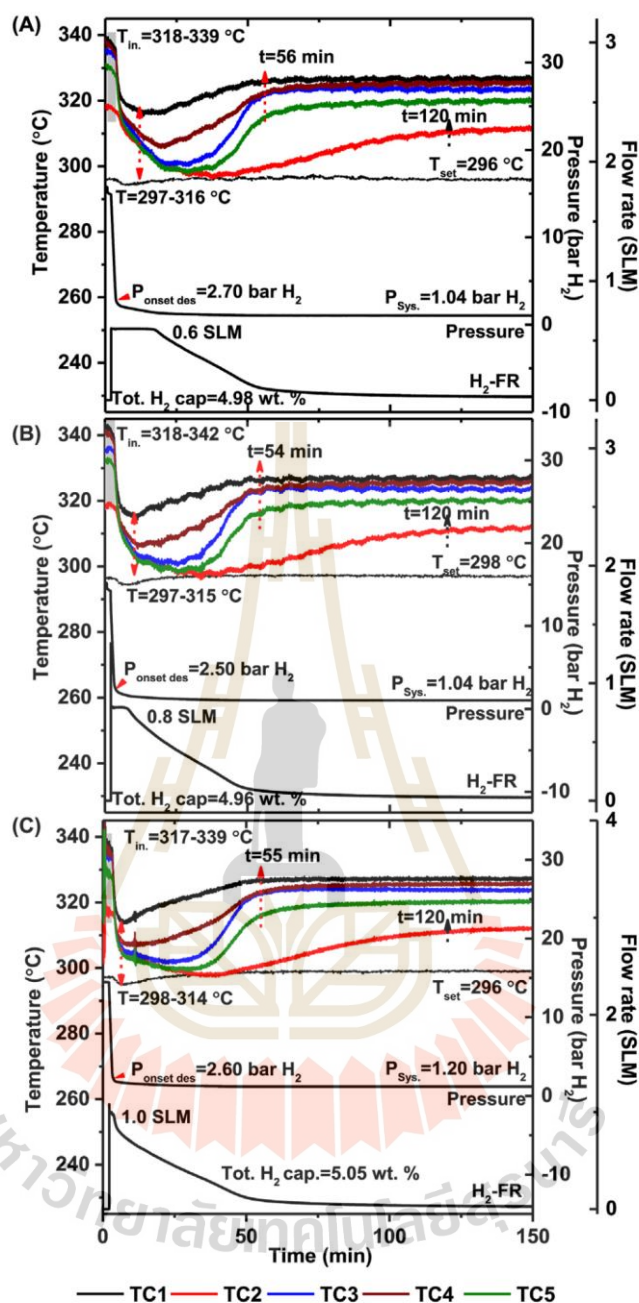


Figure 4.11 Temperature, pressure, and hydrogen mass flow rate profiles during dehydrogenation of TiF₄-CNT-MH at $\sim 300\text{ }^{\circ}\text{C}$ under 0.6 SLM (A), 0.8 SLM (B) and 1.0 SLM (C).

Although H₂-FR varies from 0.6-1.0 SLM, there is no significant change in dehydrogenation kinetics, indicated by comparable dehydrogenation times of ~ 54 -56 min (TC1 and TC3-TC5) and 120 min (TC2) along with total hydrogen capacities of 4.96-5.05 wt.% H₂ (Figure 4.11(A)-(C)). Evaluating dehydrogenation performance at different

tank positions, TC1 and TC3-TC5 exhibit faster dehydrogenation rates than TC2, resulting in a reduction of dehydrogenation time from ~ 120 min (TC2) to ~ 54 -56 min (TC1 and TC3-TC5) (Figure 4.11(A)-(C)). This difference can be attributed to the lower T_{in} at TC2, leading to less favorable dehydrogenation kinetics. Additionally, the significant temperature reduction during the endothermic event (ΔT) indicates effective dehydrogenation.

In the axial direction, the sample at the end opposite to the H_2 inlet/outlet (TC3) shows a substantial temperature reduction ($\Delta T \sim 35$ °C) as compared to the samples at the H_2 inlet/outlet and the middle position (TC1 and TC2, respectively) ($\Delta T \sim 20$ -23 °C) (Figure 4.11(A)-(C)). The superior dehydrogenation at TC3 to that at TC2 is attributed to the higher T_{in} at TC3. The lower ΔT at TC1 is likely due to the small sample size in contact with the temperature sensor. In the radial direction, the sample at the middle position (TC2) exhibits a lower ΔT (~ 20 °C) than the samples adjacent to the tank wall (TC4 and TC5) ($\Delta T \sim 35$ °C) (Figure 4.11(A)-(C)). This difference can be explained by the higher T_{in} of the samples at TC4 and TC5 due to their intimate to the external heater.

Additionally, dehydrogenation experiments are conducted on the TiF_4 -CNT-MH tank under a constant hydrogen flow rate (H_2 -FR) of 0.6 SLM at varying $T_{set}=310$ -340 °C. From Figure 4.12(A)-(C), the T_{in} for all experiments are approximately 10-30 °C higher than T_{set} . For instance, experiments at $T_{set}=309$, 319, and 340 °C show T_{in} values of 320-339, 332-349, and 349-367 °C, respectively. Moreover, both P_{eq} and $P_{onset des}$ increase with T_{in} (or T_{set}), corresponding to 3-4, 3.5-6, and 6-9 bar H_2 for P_{eq} and 2.40, 3.50, and 5.60 bar H_2 for $P_{onset des}$ (Zhang et al., 2018).

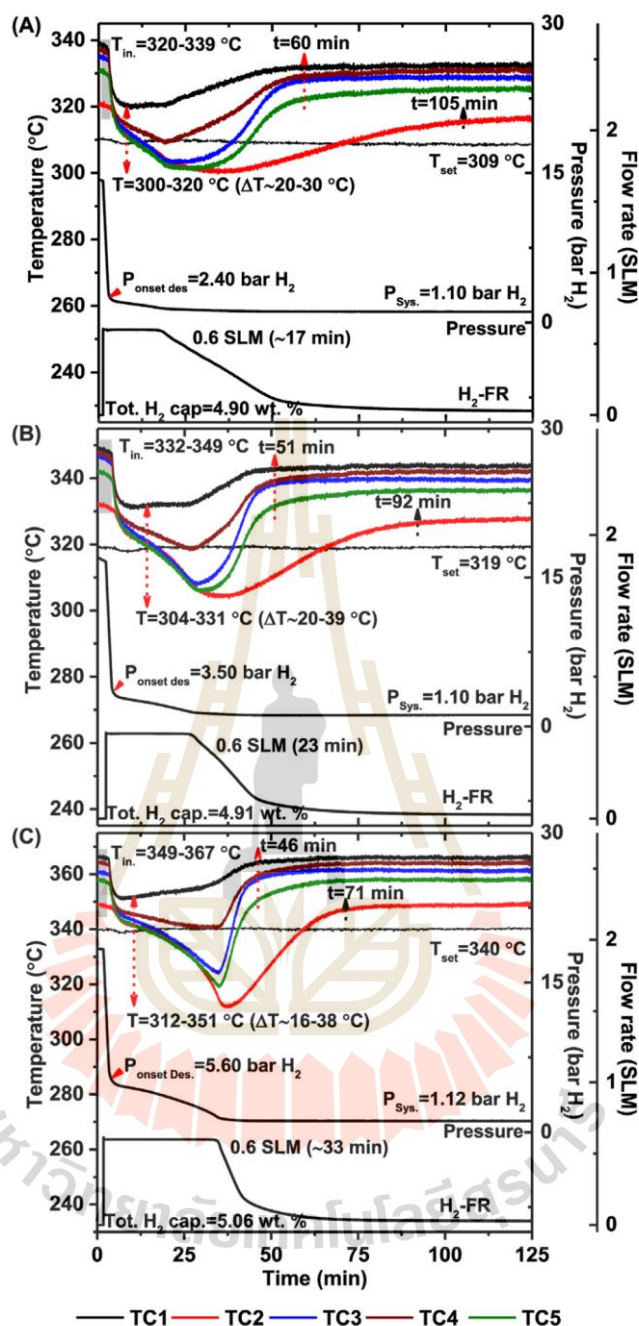


Figure 4.12 Temperature, pressure, and hydrogen mass flow rate profiles during dehydrogenation of TiF₄-CNT-MH tank under 0.6 SLM at 310 °C (A), 320 °C (B) and 340 °C (C).

To achieve comparable hydrogen capacities of 4.90-5.06 wt.% H₂, the experiment at a lower T_{set} requires a longer dehydrogenation time. For example, dehydrogenations at T_{set}=309 °C are completed within 60 min (TC1 and TC3-TC5) and 105 min (TC2) (Figure 4.12(A)), while those at T_{set}=340 °C proceed significantly faster in

46 min (TC1 and TC3-TC5) and 71 min (TC2) (Figure 4.12(C)). Additionally, the experiment at elevated T_{set} exhibits significant temperature reduction during the endothermic event (ΔT) and maintained H_2 -FR at 0.6 SLM for a longer period. Specifically, ΔT and the time of constant H_2 -FR (0.6 SLM) for the experiment at $T_{\text{set}}=309$ °C are approximately 20-30 °C and 17 min (Figure 4.12(A)), respectively, while those at $T_{\text{set}}=319$ and 340 °C increase to 16-39 °C and 23-33 min, respectively (Figure 4.12(B) and (C)). These suggest that the dehydrogenation rate under H_2 -FR=0.6 SLM of the TiF_4 -CNT-MH tank remains consistent at elevated T_{set} . The delayed dehydrogenation rate at the center of the tank (TC2) compared to other positions can be explained by the lowest T_{in} , consistent with the discussion of the results in Figure 4.11. For dehydrogenation in both axial and radial directions, since the trends of ΔT at all TCs are identical to the results in Figure 4.11, the same explanation is applicable. It should also be noted that the rates of temperature reduction and increment during the endothermic dehydrogenation of the experiment at low T_{set} (309 °C) are gradual, resulting in symmetrically U-shaped curves of temperature profiles at all TCs (Figure 4.12(A)). For the experiments at high T_{set} (319-340 °C), the temperature reduction rate is rather slow at $P_{\text{sys}} \sim P_{\text{onset des}}$ and rapidly enhances with the reduction of P_{sys} (Figure 4.12(B) and (C)). These findings indicate that the slow dehydrogenation rate of the experiment at low T_{set} is compatible with H_2 -FR=0.6 SLM, preventing the accumulation of desorbed hydrogen inside the tank. However, experiments at high T_{set} , starting at high pressure ($P_{\text{onset des}}$) and proceeding rapidly, are delayed by the slow H_2 -FR. Therefore, a suitable H_2 -FR should be applied when targeting the best kinetics.

Further investigations focus on the dehydrogenation processes of the TiF_4 -CNT-MH tank under H_2 -FR of 1.0 SLM at $T_{\text{set}}=309$ -340 °C. From Figure 4.13, the initial temperatures (T_{in}) for all experiments under H_2 -FR=1.0 SLM are approximately 8-30 °C higher than T_{set} , aligning with the observations from experiments under H_2 -FR=0.6 SLM (Figure 4.12). Comparable dehydrogenation times of 67-70 min (TC1 and TC3-TC5) and 120-123 min (TC2), temperature reduction of 16-28 °C, and total hydrogen capacities of 4.97-4.98 wt.% H_2 are achieved from the experiments at $T_{\text{set}}=309$ and 319 °C (Figure 4.13(A) and (B)). Thus, under the influence of the higher H_2 -FR (1.0 SLM), dehydrogenation kinetics remain consistent at $T_{\text{set}}=309$ -319 °C. Significant improvement

in dehydrogenation kinetics is observed at $T_{\text{set}}=340\text{ }^{\circ}\text{C}$, evident in the reduced reaction time to 43 min (TC1 and TC3-TC5) and 78 min (TC2), the increased ΔT up to $37\text{ }^{\circ}\text{C}$, and total capacity of 5.06 wt.% H_2 (Figure 4.13(C)).

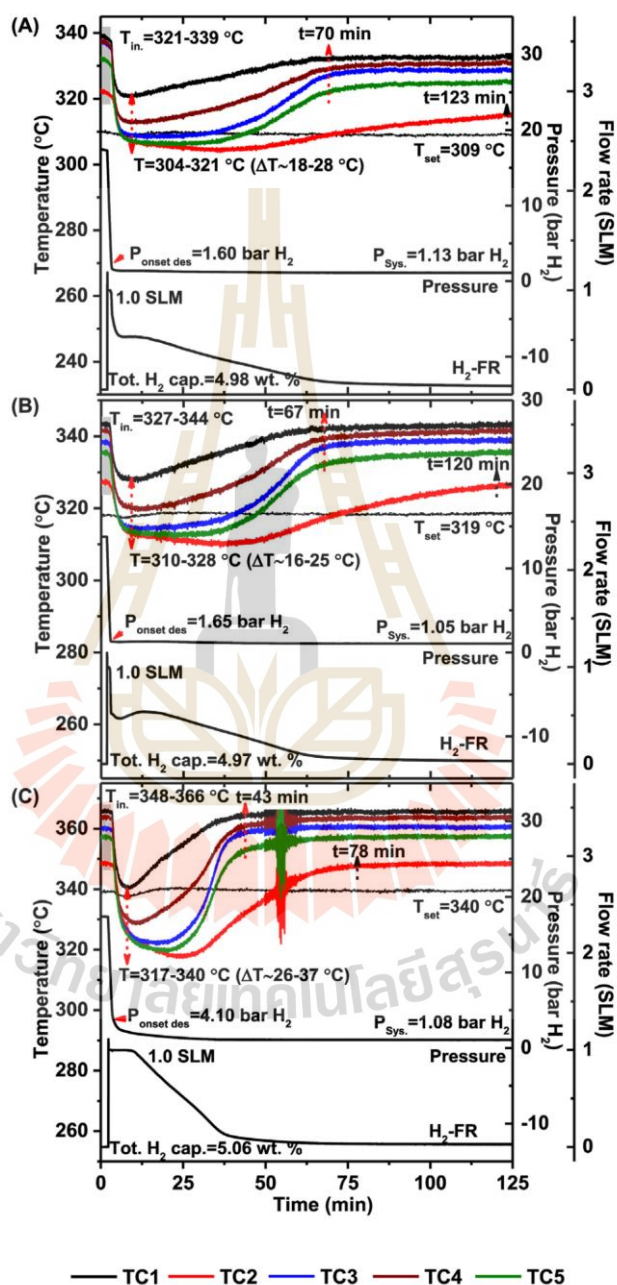
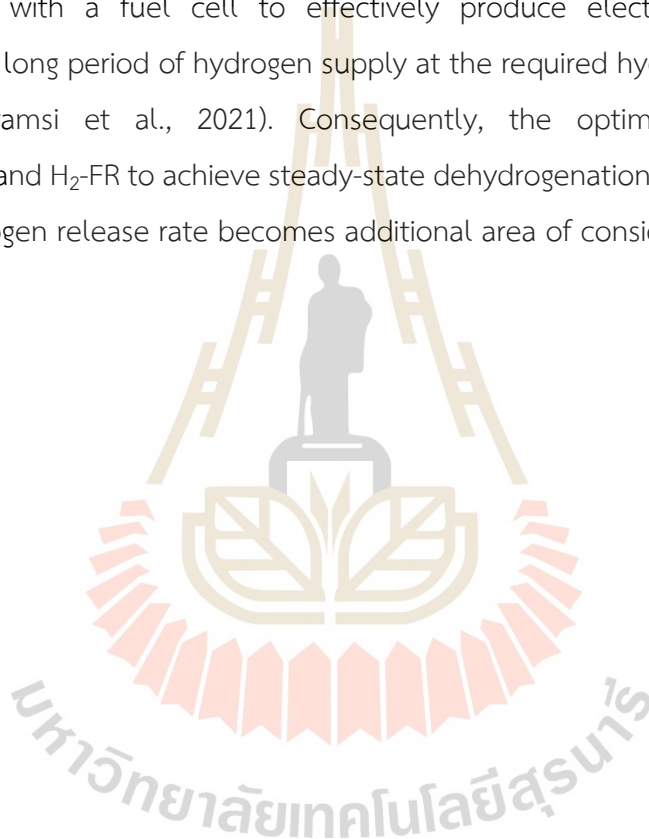
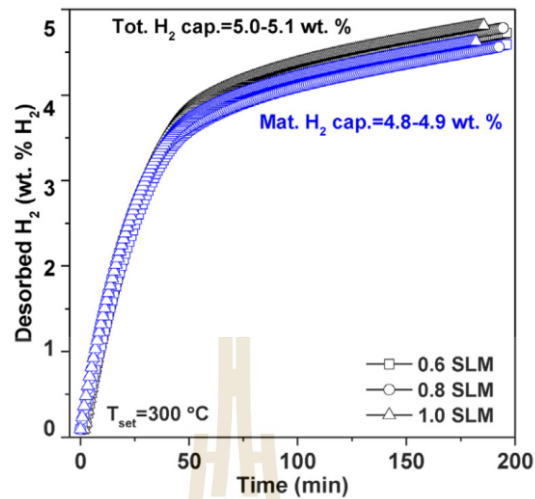


Figure 4.13 Temperature, pressure, and hydrogen mass flow rate profiles during dehydrogenation of TiF₄-CNT-MH tank under 1.0 SLM at 310 °C (A), 320 °C (B) and 340 °C (C).

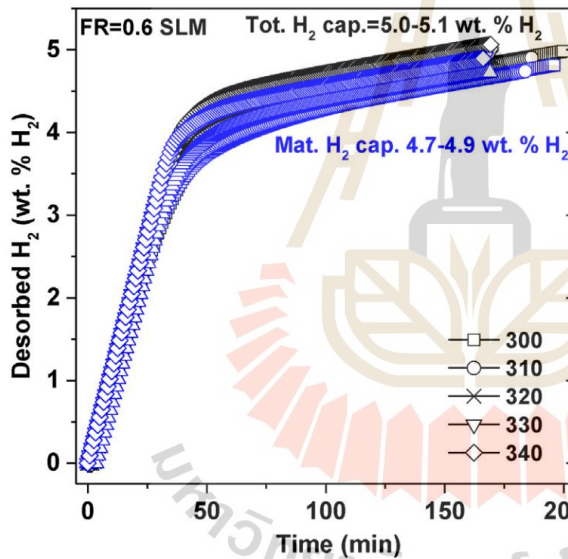
Furthermore, the dehydrogenation performances of the $\text{TiF}_4\text{-CNT-MH}$ tank under different T_{set} and $\text{H}_2\text{-FR}$ conditions are characterized in Figure 4.14. Comparable total and material capacities of approximately 5.0 and 4.7-4.9 wt.% H_2 , respectively, are observed under all conditions. By increasing both T_{set} and $\text{H}_2\text{-FR}$, the dehydrogenation kinetics of the $\text{TiF}_4\text{-CNT-MH}$ tank are enhanced (Figure 4.14(C)). Therefore, achieving a fast dehydrogenation rate at high operating temperatures requires a higher $\text{H}_2\text{-FR}$ for optimal kinetic results. However, the most suitable condition for coupling with a fuel cell to effectively produce electrical power involves maintaining a long period of hydrogen supply at the required hydrogen mass flow rate (Nyallang Nyamsi et al., 2021). Consequently, the optimization of operating temperature and $\text{H}_2\text{-FR}$ to achieve steady-state dehydrogenation while maintaining the desired hydrogen release rate becomes additional area of consideration.



(A)



(B)



(C)

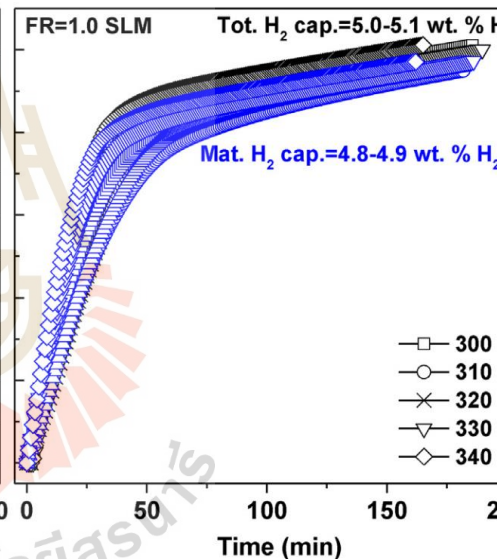


Figure 4.14 Dehydrogenation kinetics of $\text{TiF}_4\text{-CNT-MH}$ tank at $300\text{ }^\circ\text{C}$ under 0.6-1.0 SLM (A) and at $300\text{-}340\text{ }^\circ\text{C}$ under 0.6 SLM (B) and 1.0 SLM (C).

Subsequent investigations focus on the kinetic behaviors of the $\text{TiF}_4\text{-CNT-MH}$ tank under different T_{set} and $\text{H}_2\text{-FR}$, employing the reduced time method (Jones et al., 1975; Sharp et al., 1966) and referring to the kinetic models listed in Table 3.2. Considering gas-solid reactions, limitations related to fluid dynamics and heat transfer become more prominent with increased material content. Fluid dynamic limitations relate to hydrogen diffusion within the hydride bed, while heat transfer restrictions

arise from the low thermal conductivity of hydrides, influencing heat uptake and release during de/rehydrogenation. Typically, analyses on kinetic behaviors are conducted for a specific mass of hydride, neglecting fluid dynamic and heat transfer restrictions, as in the case of laboratory scale studies (Atilio Puszkiel, 2019). However, we aim to explore how the kinetic behaviors of TiF₄-CNT-MH change when fluid dynamic and heat transfer restrictions are considered after upscaling to a hydrogen storage tank.

In Figure 4.10(A), the best-fitted kinetic model of TiF₄-CNT-MH in the laboratory scale is the geometrical contraction with the rate-limiting step of R2 (Table 3.2). For the TiF₄-CNT-MH tank, the plots of $(t/t_{0.5})_{\text{theoretical}}$ versus $(t/t_{0.5})_{\text{experimental}}$ during dehydrogenation at $T_{\text{set}}=300$ °C under various H₂-FR (0.6-1.0 SLM) show the best-fitted results as the geometrical contraction model with the rate-limiting step of R3 (Figure 4.15). With constant H₂-FR, the best-fitted model remains as the geometrical contraction with the rate-limiting step of R2 and R3 up to $T_{\text{set}}=330$ °C (0.6 SLM) and 340 °C (1.0 SLM) (Figure 4.16 and Figure 4.17). At $T_{\text{set}}=340$ °C under H₂-FR=0.6 SLM, the best-fitted result appears as the nucleation model with the rate-limiting step of A2 (Figure 4.16). Both geometrical contraction and nucleation models, with the rate-limiting step of R2, R3, and A2, align with step (i) of the dehydrogenation process, i.e., the decomposition of the hydride phase with metal/hydride interface movement (Atilio Puszkiel, 2019).

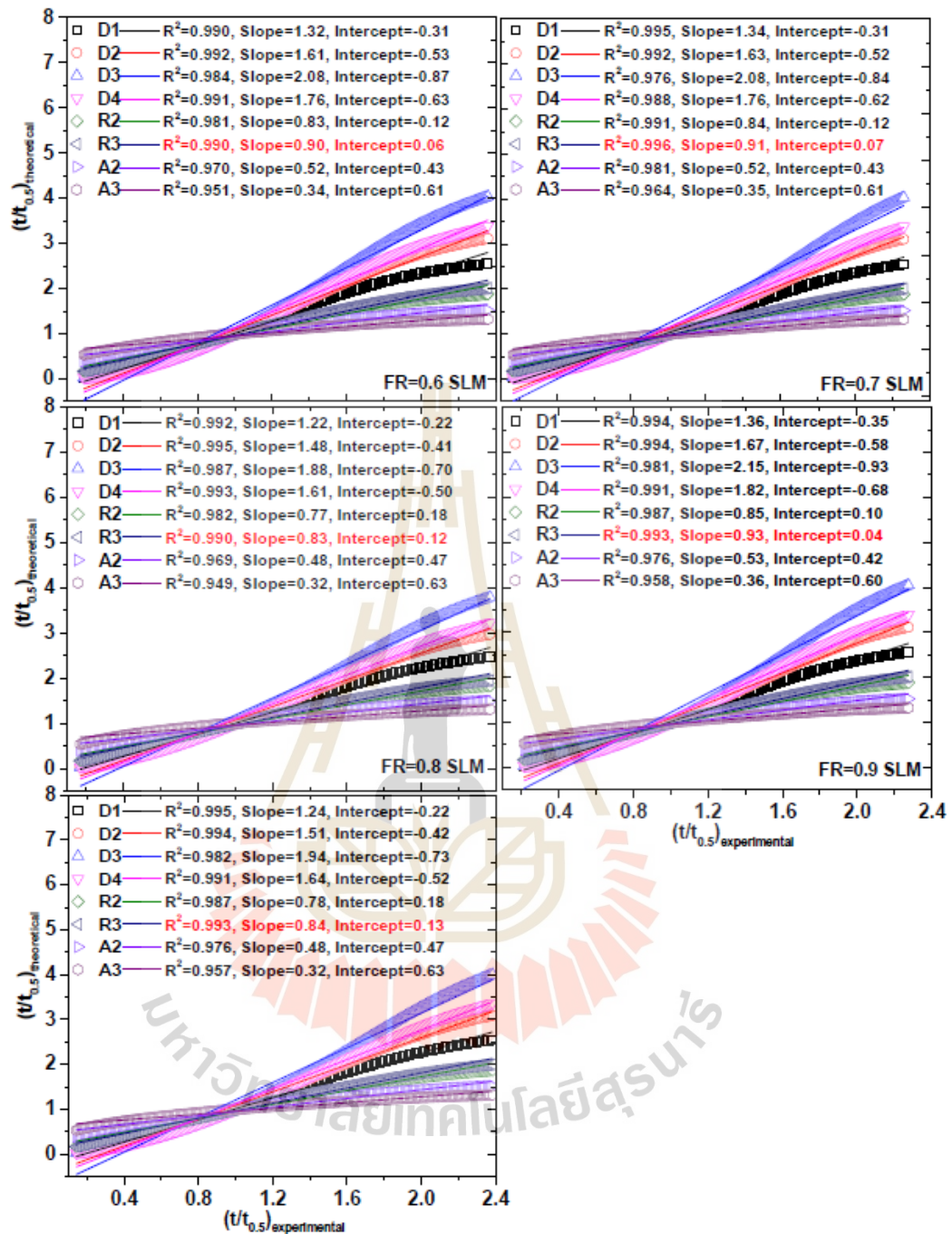


Figure 4.15 Plots of $(t/t_{0.5})_{\text{theoretical}}$ versus $(t/t_{0.5})_{\text{experimental}}$ and model fitting during dehydrogenation of $\text{TiF}_4\text{-CNT-MH}$ tank with H_2 -FR of 0.6-1.0 SLM.

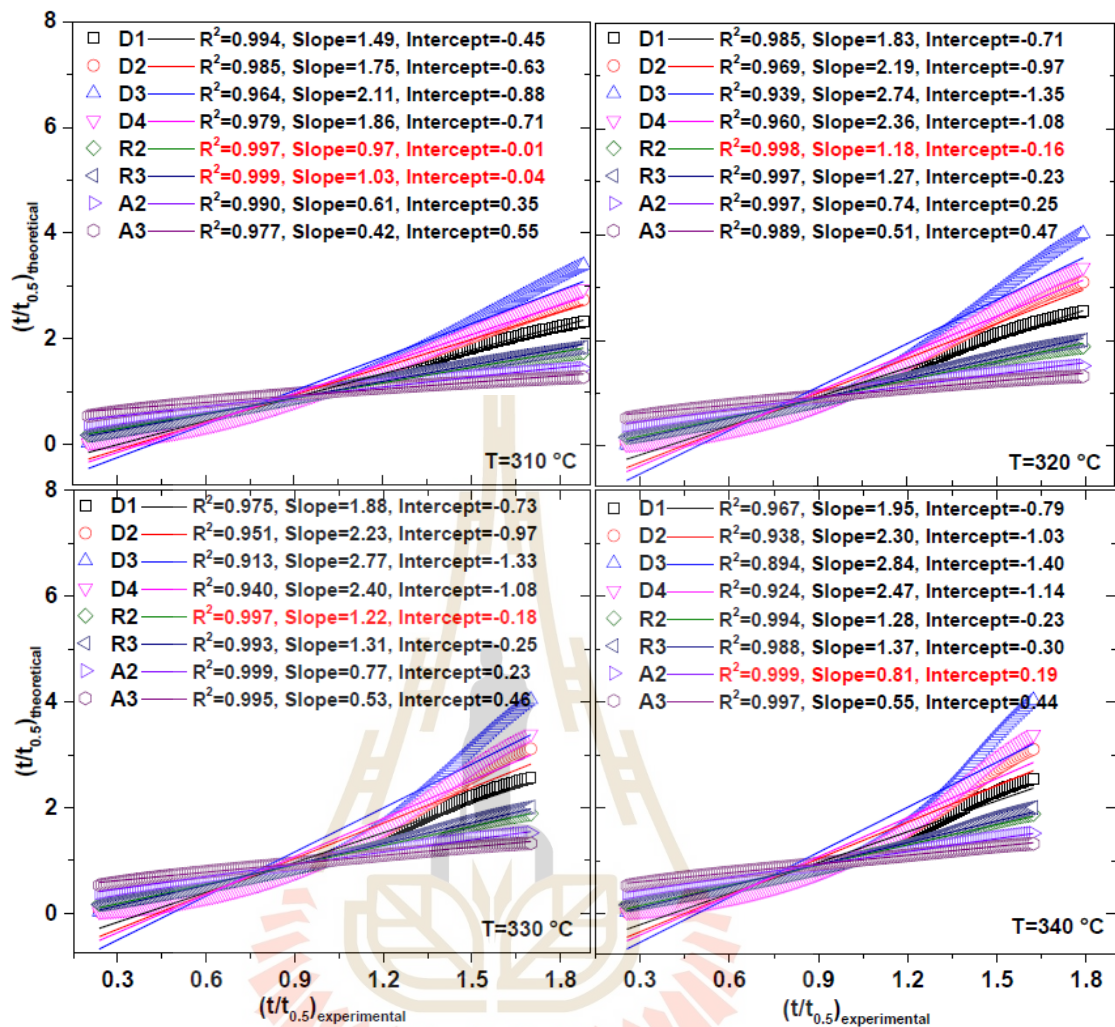


Figure 4.16 Plots of $(t/t_{0.5})_{\text{theoretical}}$ versus $(t/t_{0.5})_{\text{experimental}}$ and model fitting during dehydrogenation of TiF₄-CNT-MH tank at 310-340 °C with hydrogen mass flow rate of 0.6 SLM.

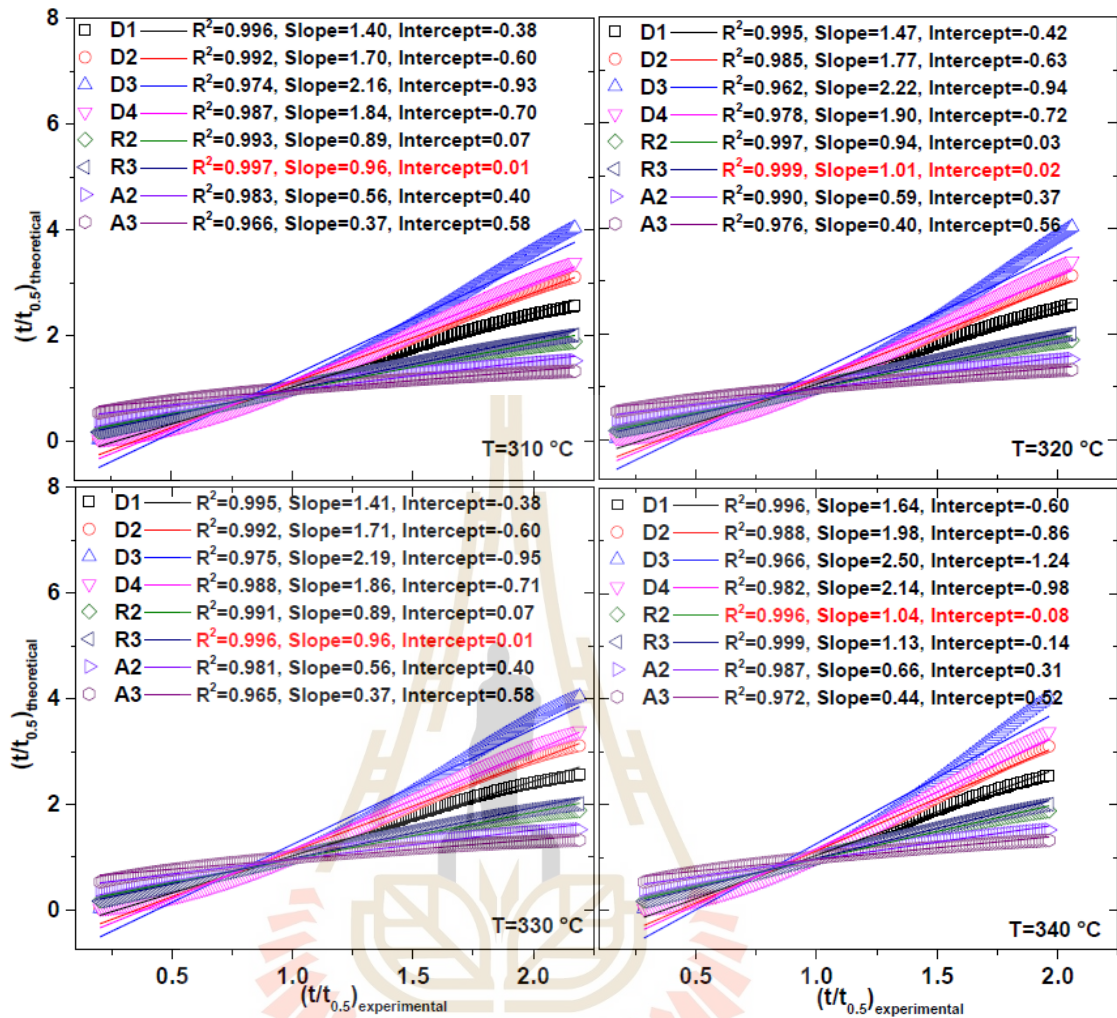


Figure 4.17 Plots of $(t/t_{0.5})_{\text{theoretical}}$ versus $(t/t_{0.5})_{\text{experimental}}$ and model fitting during dehydrogenation of $\text{TiF}_4\text{-CNT-MH}$ tank at 310-340 °C with hydrogen mass flow rate of 1.0 SLM.

The alterations in kinetic behaviors after upscaling TiF₄-CNT-MH from the laboratory to the tank scale and under different operating temperatures and H₂-FR are summarized. In Figure 4.18, the best-fitted models for TiF₄-CNT-MH in both laboratory and tank scales under nearly all T_{set} and H₂-FR conditions are comparable, as the geometrical contraction. At T_{set}=300 °C under all H₂-FR, dehydrogenations in the laboratory scale reveal the rate-limiting step of R2, while those in the tank scale are represented by R3. As the sample mass increases to the tank scale, the rate-limiting step for the decomposition of the hydride phase with metal/hydride interface movement tends to shift from two-dimensional to three-dimensional growth (R2 to R3). By elevating T_{set} up to 320 and 340 °C for H₂-FR of 0.6 and 1.0 SLM, respectively, the rate-limiting step of TiF₄-CNT-MH tank approaches that of the laboratory scale (R2). This can be attributed to the heat compensation for endothermic dehydrogenation achieved at high T_{set}, potentially resulting in the reduced heat transfer restrictions and comparable kinetic behaviors between laboratory and tank scales. Moreover, it is noteworthy that at low H₂-FR, comparable kinetic behaviors between laboratory and tank scales are observed at lower T_{set}. For instance, the rate-limiting step of R2 is observed at T_{set}=310-320 °C for the experiment under 0.6 SLM, while under higher H₂-FR (1.0 SLM), it occurs at T_{set}=340 °C. The dehydrogenation at high H₂-FR (1.0 SLM) likely induces fluid dynamic restrictions, as hydrogen diffusion near the H₂ in/outlet position is significantly faster than in other positions within the hydride beds.

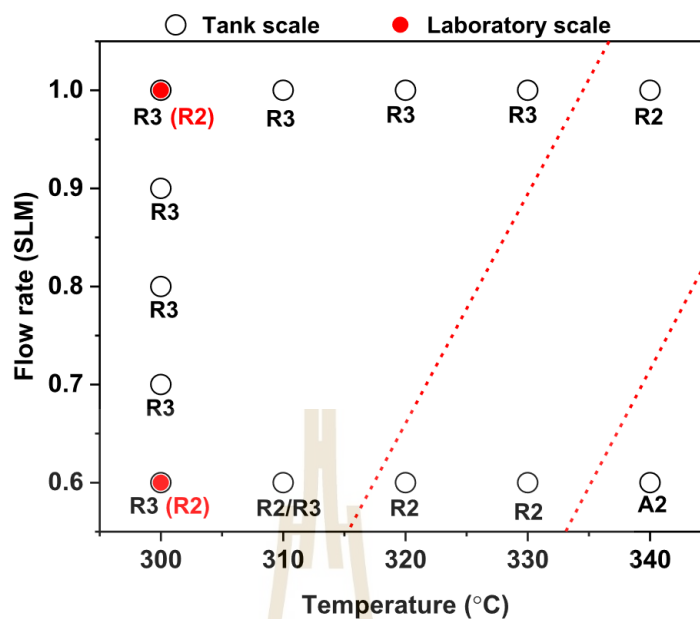


Figure 4.18 Rate-limiting step for desorption as a function of H_2 -FR and temperatures of TiF_4 -CNT-MH in laboratory and tank scales.

In conclusion, the investigation focuses on examining the dehydrogenation kinetics of TiF_4 -MWCNT-doped MgH_2 under varying operational conditions, including temperatures of 300-340 °C and H_2 -FR ranging from 0.6 to 1.0 SLM. In the laboratory scale (1.8320 g), increase in H_2 flow rate significantly enhances the dehydrogenation rate at $T = 300$ °C, while the kinetic behaviors and rate-limiting step remain consistent as the geometrical contraction model and R2. For the tank scale (45.2252 g), dehydrogenation kinetics remain consistent across all H_2 -FR at $T = 300$ °C. However, maintaining H_2 -FR at 0.6 SLM leads to changes in desorption kinetics with temperature. At lower temperature and H_2 -FR, the accumulation of desorbed hydrogen in the tank is hindered. Conversely, at higher temperatures, improved kinetics results in the consistent H_2 -FR of 0.6 SLM over extended period. Achieving optimal dehydrogenation kinetics requires a higher H_2 flow rate (1.0 SLM) at elevated temperatures.

The most suitable model for describing kinetic behaviors across various temperatures and H_2 flow rate conditions in both laboratory and tank-scale experiments is the geometrical contraction model. Particularly at lower temperatures, scaling up the sample mass to the tank scale induces a shift in the rate-limiting step from two-dimensional to three-dimensional growth (R2 to R3). Dehydrogenation at high

H₂ flow rate (1.0 SLM) may introduce fluid dynamic restriction due to significant variations in hydrogen diffusion at the H₂ inlet and outlet, as well as within the hydride beds.

4.2 Solid-state batteries

4.2.1 Nanoconfinement of an ammine magnesium borohydride composite electrolyte in a mesoporous silica scaffold

Specific surface area, pore size distributions, and pore volume of the SBA-15 are determined by N₂ adsorption-desorption technique. The surface area, pore size, and pore volume of SBA-15 are 825 m²/g, 5.8 nm, and 0.77 cm³/g, respectively (Figure 4.19(A) and (B)). Rietveld refinement results indicate that the as-prepared composite contained 47.7 wt.% (53.1 mol%) of Mg(BH₄)₂·NH₃ and 52.3 wt.% (46.9 mol%) of Mg(BH₄)₂·2NH₃, resulting in the composition Mg(BH₄)₂·1.47NH₃ (Figure 4.20). Powder X-ray diffraction (PXD) data of confined samples are shown in Figure 4.21. The PXD data of the Mg(BH₄)₂·1.47NH₃ and SBA-15 are also presented in Figure 4.21 for comparison. The lack of peaks in the diffraction pattern of MI100 suggests that by using 100% pore filling, the amorphous state of Mg(BH₄)₂·1.47NH₃ is maintained in pores of SBA-15. This is supported by the change in background between MI100 and SBA-15, which suggests the presence of additional amorphous material. In the case of MI200 and MI300, diffraction patterns of Mg(BH₄)₂·NH₃ are observed, suggesting recrystallization of excess Mg(BH₄)₂·NH₃ on the surface of SBA-15 upon melt infiltration, along with the amorphous material being stabilized on the outer surface of the nano-particles of SBA-15.

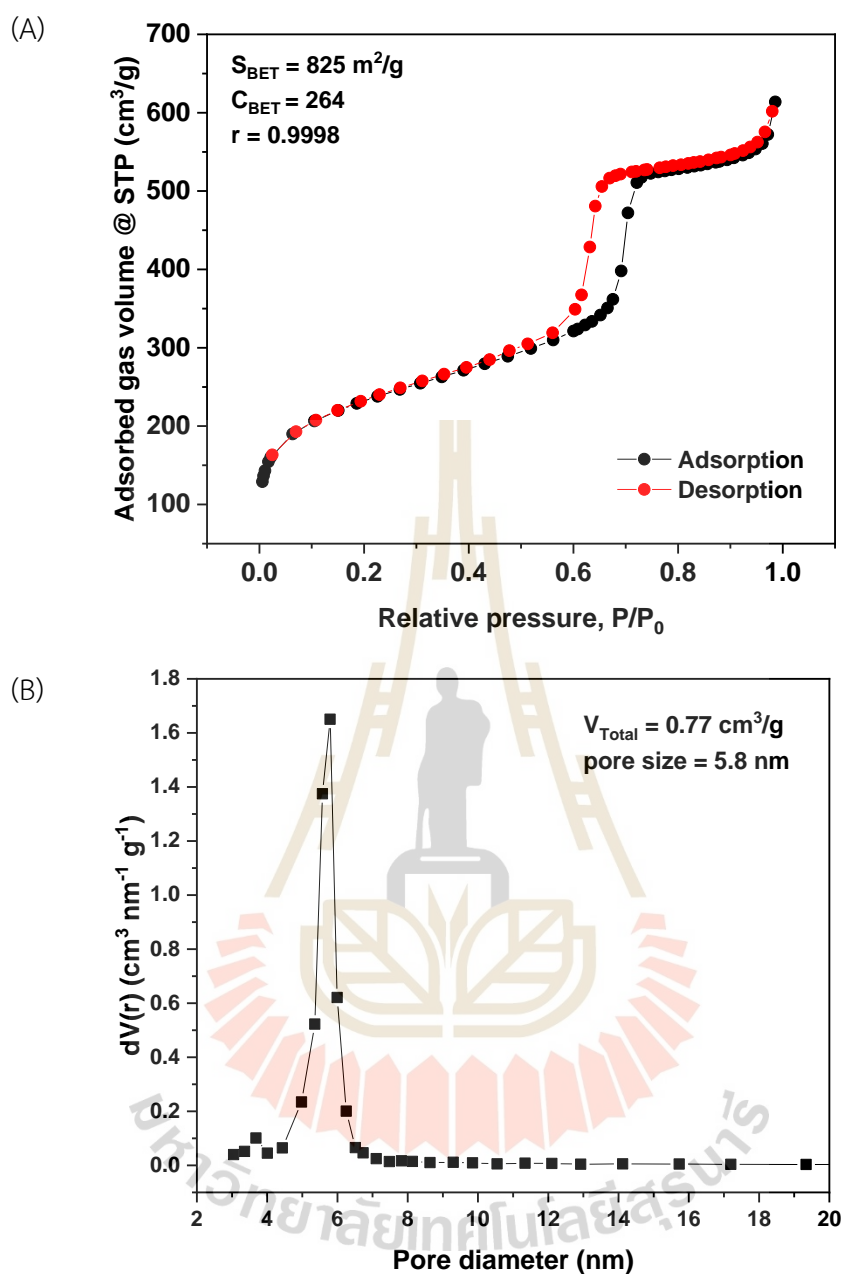


Figure 4.19 Nitrogen adsorption-desorption isotherms (A) and corresponding pore size distribution (B) of mesoporous silica SBA-15 after drying at 300 °C under dynamic vacuum overnight.

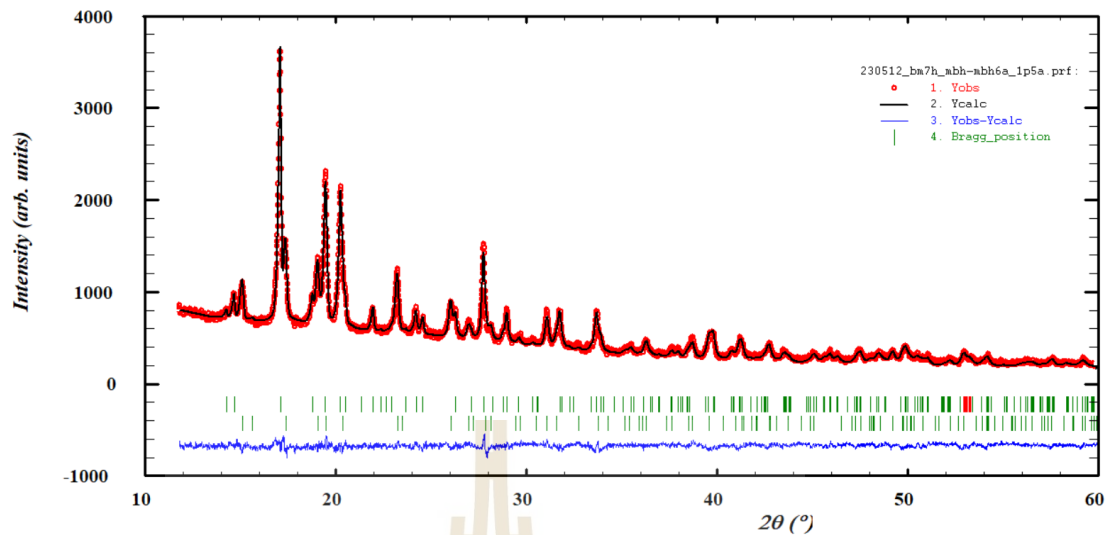


Figure 4.20 Reitveld refinement of powder X-ray diffraction (PXRD) data for as-prepared $\text{Mg}(\text{BH}_4)\cdot 2\text{NH}_3$ and $\text{Mg}(\text{BH}_4)\cdot \text{NH}_3$ composite ($\lambda = 1.54056 \text{ \AA}$), showing observed (red circles) and calculated (black line) curves, and a difference curve below (blue line). Reflections corresponding to monoclinic $\text{Mg}(\text{BH}_4)\cdot 2\text{NH}_3$ (1st trick) and $\text{Mg}(\text{BH}_4)\cdot \text{NH}_3$ (2nd trick). Final discrepancy factors: $R_p = 3.48 \%$, $R_{wp} = 3.83 \%$ (not corrected for background), $R_p = 14.2 \%$, $R_{wp} = 9.05 \%$ (conventional Rietveld R-factors), $R_{\text{Bragg}}(\text{Mg}(\text{BH}_4)\cdot 2\text{NH}_3) = 5.84 \%$, $R_{\text{Bragg}}(\text{Mg}(\text{BH}_4)\cdot \text{NH}_3) = 5.42 \%$, and global $\chi^2 = 501$. The mixture consists of 52.3 wt.% of $\text{Mg}(\text{BH}_4)\cdot 2\text{NH}_3$ and 47.7 wt.% of $\text{Mg}(\text{BH}_4)\cdot \text{NH}_3$, which is equivalent to $\text{Mg}(\text{BH}_4)\cdot 1.47\text{NH}_3$

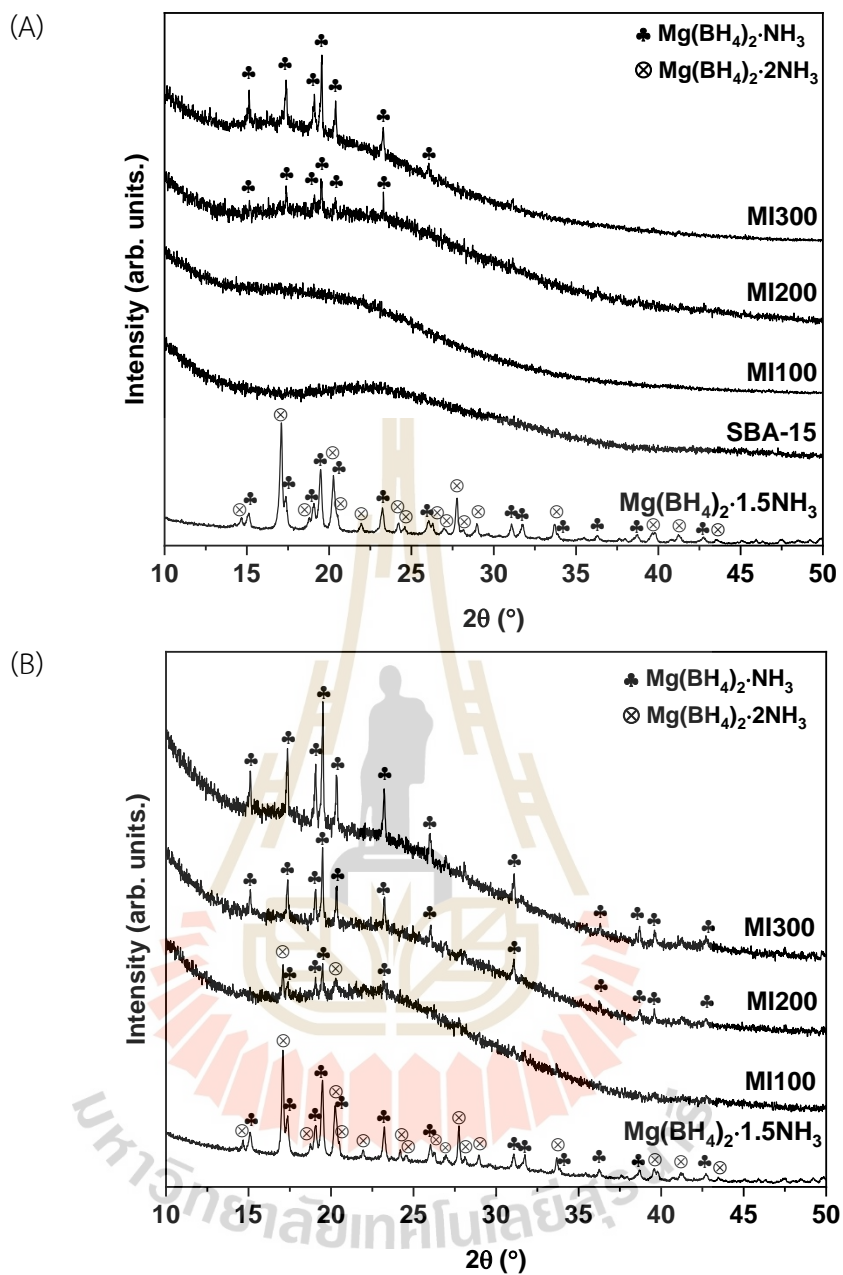


Figure 4.21 Powder X-ray diffraction diagrams of the composite, the scaffold and the nanoconfined samples, (A) after synthesis and (B) after 5 months of storage under argon atmosphere.

Solid-state ^{11}B magic-angle spinning (MAS) nuclear magnetic resonance (NMR) spectra of $\text{Mg}(\text{BH}_4)_2 \cdot 1.47\text{NH}_3$ and the nanoconfined samples are recorded and shown in Figure 4.22. The composite $\text{Mg}(\text{BH}_4)_2 \cdot 1.47\text{NH}_3$ reveals three different boron resonances at -40.5, -41.5, and -42.1 ppm. This observation indicates a physical mixture of $\text{Mg}(\text{BH}_4)_2 \cdot \text{NH}_3$ and $\text{Mg}(\text{BH}_4)_2 \cdot 2\text{NH}_3$, which contain one (-40.5 ppm) and two (-41.5 and -42.1 ppm) distinct boron sites, respectively (Yan, Dononelli et al., 2020; Yan et al., 2022a). The resonances can be satisfactorily simulated with Lorentz-shaped peaks, from which a full width at half maximum (*FWHM*) linewidth of 1.08 ± 0.05 ppm is estimated for the tallest resonance at -40.5 ppm from $\text{Mg}(\text{BH}_4)_2 \cdot \text{NH}_3$. For all confined samples, the sharp peak at -40.3 ppm with a Lorentzian line shape indicates the presence of a high degree of boron dynamics in the eutectic molten state, suggesting the stabilization of the molten state as seen in previous studies (Yan, Grinderslev, Jørgensen et al., 2020). The MI100 sample (*FWHM*= 0.66 ± 0.05 ppm for the -40.3 ppm resonance) is estimated to consist of 63 mol % nanoconfined material and 37 mol % $\text{Mg}(\text{BH}_4)_2 \cdot 2\text{NH}_3$. In contrast, the sharp peak (at -40.3 ppm) for MI200 and MI300 can be simulated using two Lorentzian peaks, one with *FWHM*=1.08 ppm ($\text{Mg}(\text{BH}_4)_2 \cdot \text{NH}_3$) and the other with *FWHM*= $0.62 \pm$ ppm (MI200) or 0.67 ppm (MI300). The intensities from these simulations indicate that MI200 consists of 72 mol% nanoconfined material in the non-crystalline ‘eutectic molten state’ and 28 mol% $\text{Mg}(\text{BH}_4)_2 \cdot \text{NH}_3$, whereas MI300 contains 74 mol% nano-confined material and 26 mol% $\text{Mg}(\text{BH}_4)_2 \cdot \text{NH}_3$. This is consistent with PXD results, where diffraction from $\text{Mg}(\text{BH}_4)_2 \cdot \text{NH}_3$ is visible. Two rather small resonances at -41.5, and -42.1 ppm from $\text{Mg}(\text{BH}_4)_2 \cdot 2\text{NH}_3$ are observed for MI100, however, this phase is barely visible from the diffraction pattern after synthesis, but it is more clearly seen after 5 months of storage (Figure 4.21(A) and (B)). This may be attributed to incomplete infiltration. As the degree of pore filling increases to 200 % and 300 %, there is no evidence of $\text{Mg}(\text{BH}_4)_2 \cdot 2\text{NH}_3$ in the ^{11}B NMR spectra, in accordance with the PXD results (Figure 4.21). There is no discernible difference in linewidth between the infiltrated samples, indicating that degree of pore filling does not affect boron dynamics in the range from 100 to 300 % (Table 4.1). Thus, the highly dynamic eutectic molten state is stabilized both inside pores and on the surface of SBA-15 nano-particles in accord with previous work.

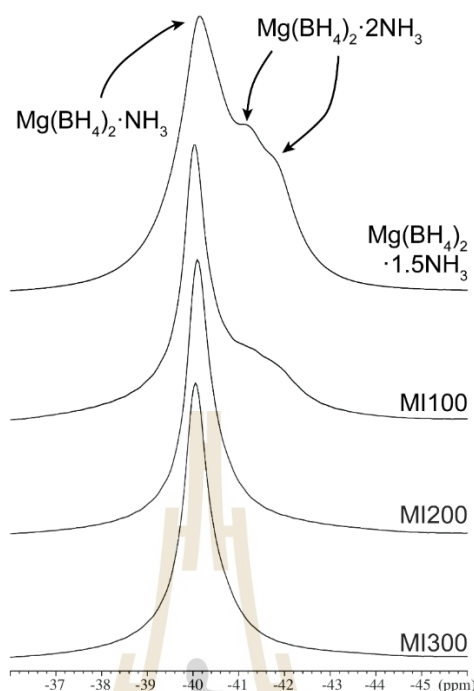


Figure 4.22 Solid-state ^{11}B MAS NMR spectra, illustrating the central-transition region, for the composite and the nanoconfined samples.

Table 4.1 Linewidth of the dominant resonance at -40 ppm for $\text{Mg}(\text{BH}_4)\cdot 1.47\text{NH}_3$ and MI100-300. It is not possible to get an accurate assessment of the starting compound due to significant peak overlap. All values are within the margin of error of the measurement.

Sample	Linewidth at -40 ppm
$\text{Mg}(\text{BH}_4)\cdot 1.47\text{NH}_3$	$1.08 (\pm 0.05 \text{ ppm})$
MI100	$0.66 (\pm 0.05 \text{ ppm})$
MI200	$0.62 (\pm 0.05 \text{ ppm})$
MI300	$0.67 (\pm 0.05 \text{ ppm})$

Furthermore, the ionic conductivity of MI100-MI300 is characterized by electrochemical impedance spectroscopy (EIS). The Mg^{2+} ion conductivity as a function of temperature of the first heating and cooling cycle of the samples are shown in Figure 4.23. At $T = 32\text{--}80$ °C, the MI100 reveals the Mg^{2+} ion conductivity of 3.1×10^{-8} – $3.5 \times 10^{-8} \text{ S}\cdot\text{cm}^{-1}$. Considering the cycling stability of MI100 (Figure 4.24(A)), the conductivity gradually decreases in the 2nd and 3rd cycles. This may be attributed to

the fact that electrolyte further intercalates into SBA-15, which leads to the reduced particle-particle contact and lower ionic conductivity. Both MI200 and MI300 achieved higher Mg^{2+} ionic conductivities of $9.1 \times 10^{-6} - 2.7 \times 10^{-4} \text{ S}\cdot\text{cm}^{-1}$ and $5.5 \times 10^{-6} - 7.4 \times 10^{-4} \text{ S}\cdot\text{cm}^{-1}$, respectively. This could be due to the existence of electrolyte on the surface of SBA-15, which provides additional pathways for Mg^{2+} ion migration as compared to MI100. Moreover, the significant increase in ionic conductivity of MI200 is observed upon the 1st cooling cycle and stable for at least 3 cycles of heating and cooling between temperature of 32-80 °C (Figure 4.24(B)). Therefore, by using 200% degree of pore filling, the grain boundaries between the particles disappear, resulting in the higher ionic conductivity in the following cycles. For the MI300, the apparent hysteresis is due to melting/recrystallization of the $\text{Mg}(\text{BH}_4)_2\cdot 1.47\text{NH}_3$. This suggests that the amount of SBA-15 is too low to suppress the recrystallization, and it behaves similar to the bulk sample (Figure 4.24(C)).

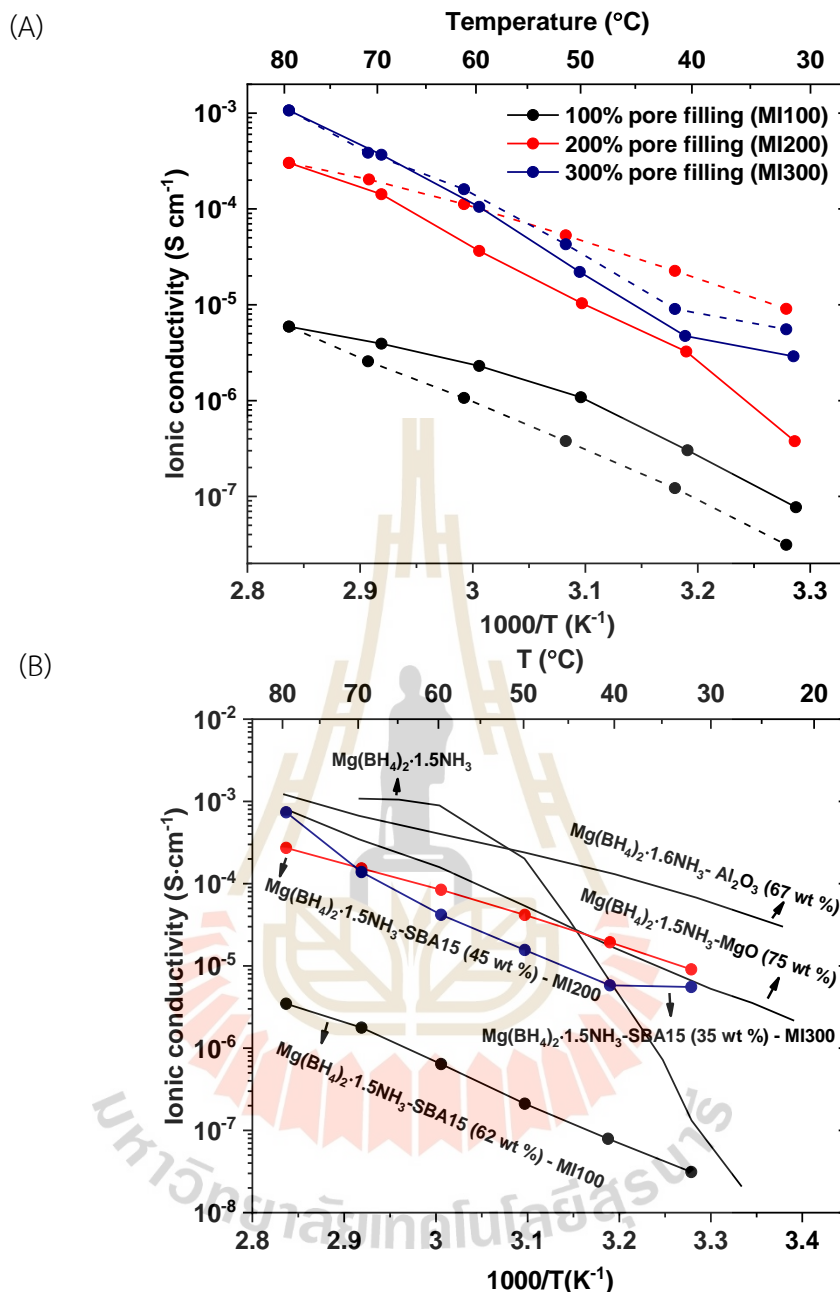


Figure 4.23 Mg^{2+} ion conductivity as a function of temperature of the MI100, MI200, and MI300 during the 2nd heating cycle (A) and the other ammine magnesium borohydrides doped with oxide nanoparticles (B) (Yan et al., 2022a; Yan, Grinderslev, Jørgensen et al., 2020).

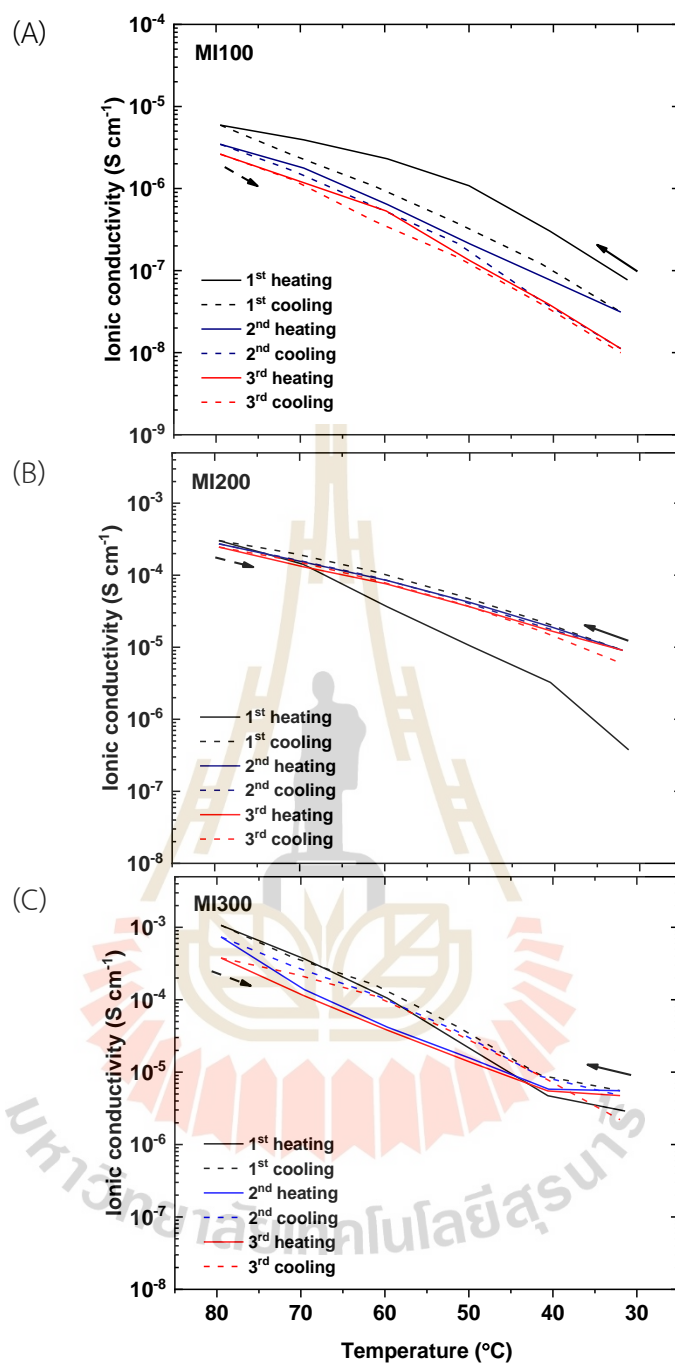


Figure 4.24 Temperature-dependent Mg^{2+} -ionic conductivities of the MI100-300 upon heating and cooling for 3 cycles at temperature range of 30–80 $^{\circ}C$.

Comparing with $\text{Mg}(\text{BH}_4)_2 \cdot 1.5\text{NH}_3$, the MI200 and MI300 show higher Mg^{2+} ion conductivity at $T < 50$ °C. Moreover, the MI200 shows a slightly higher Mg^{2+} ion conductivity to $\text{Mg}(\text{BH}_4)_2 \cdot 1.5\text{NH}_3$ doped with 75 wt.% of MgO at the low temperature range of 32–45 °C (Yan, Grinderslev, Jørgensen et al., 2020). By plotting $\ln(\sigma T)$ versus $1/T$ (K^{-1}), the activation energy could be extracted. In all cases, the activation energy is lower than $\text{Mg}(\text{BH}_4)_2 \cdot 1.5\text{NH}_3$ (3.4 eV at $T < 55$ °C) at the temperature range 32–80 °C (Table 4.2).

Table 4.2 Magnesium ionic conductivity ($\sigma(\text{Mg}^{2+})$) and the activation energy (E_A) at the temperature range of 32–80 °C of MI100–300 and other amine magnesium borohydride nanocomposites. (Yan et al., 2022b; Yan, Grinderslev, Jørgensen et al., 2020)

Samples	E_A (eV)	$\sigma(\text{Mg}^{2+}) / (\text{S cm}^{-1})$
		Min(32 °C) – max(80 °C)
MI100	0.97	$3.1 \times 10^{-8} - 3.4 \times 10^{-6}$
MI200	0.69	$9.1 \times 10^{-6} - 2.7 \times 10^{-4}$
MI300	0.99	$3.2 \times 10^{-6} - 7.4 \times 10^{-6}$
Literature (Yan et al., 2022b; Yan, Grinderslev, Jørgensen et al., 2020)		
$\text{Mg}(\text{BH}_4)_2 \cdot 1.5\text{NH}_3$ - 75 wt.% MgO	0.94	$5.3 \times 10^{-6} - 8.3 \times 10^{-4}$
$\text{Mg}(\text{BH}_4)_2 \cdot 1.6\text{NH}_3$ - 67 wt.% Al_2O_3	0.56	$6.7 \times 10^{-5} - 1.2 \times 10^{-3}$

The thermal stability of all samples is determined using thermogravimetric analysis (TGA) – differential scanning calorimetry (DSC) – mass spectrometry (MS). Thermal decomposition profile of as-prepared $\text{Mg}(\text{BH}_4)_2 \cdot 1.47\text{NH}_3$ reveals onset decomposition temperature (T_{onset}) of approximately 100 °C (Figure 4.25(A)), which is lower than the previous report of $\text{Mg}(\text{BH}_4)_2 \cdot 1.5\text{NH}_3$ ($T_{\text{onset}} \sim 120$ °C) (Yan, Grinderslev, Jørgensen et al., 2020). This difference can be attributed to the lower heating rate. It should be noted that the DSC curve does not exhibit clear thermal events for all experiments due to the low heating rate (2 °C/min) and the small amount of sample

(~3.5 mg) (Figure 4.25). Thermal decomposition profiles of confined samples exhibit high thermal stability at $T > 100$ °C, then start to release H_2 and a small amount of NH_3 in case of MI300 (Figure 4.25(D)). Mass loss of the confined samples (1.86 – 2.60 wt.%) increases with $Mg(BH_4)_2 \cdot 1.47NH_3$ content. The reduction of main H_2 release temperature from 193 °C for $Mg(BH_4)_2 \cdot 1.47NH_3$ ((Figure 4.25(A)) to 157–182 °C for the confined samples ((Figure 4.25(B)-(D)) can be due to the effect of nanoconfinement.

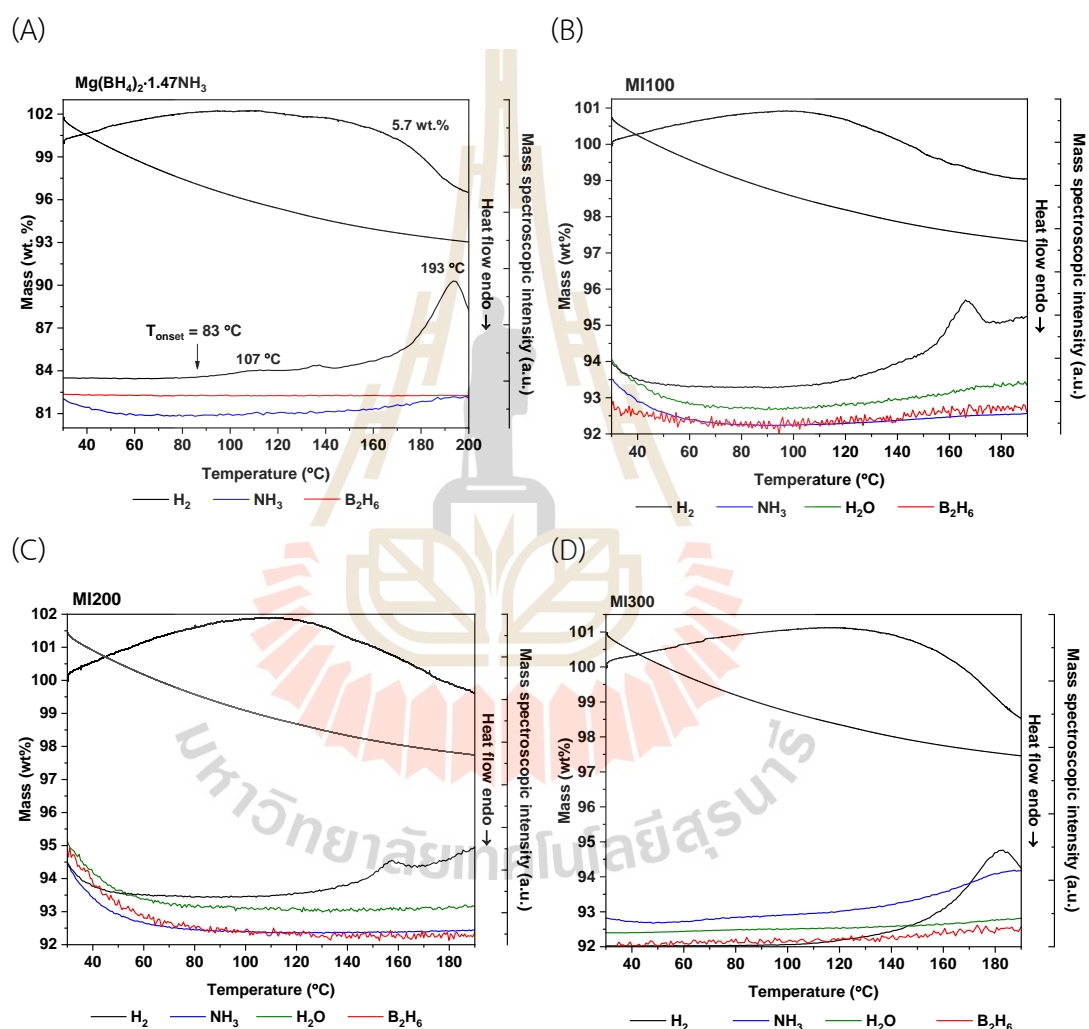


Figure 4.25 Thermogravimetric analysis (TGA)-differential scanning calorimetry (DSC) and Mass spectroscopy (MS) results of as prepared $Mg(BH_4)_2 \cdot 1.5NH_3$ heated from 30 to 200 °C (2 °C min^{-1}). The mass loss in the temperature range 100 to 200 °C is $\Delta m/m = 5.7$ wt.%, which corresponds to loss of 0.26 NH_3 molecules per formula unit. Black is hydrogen, blue is ammonia, red is diborane and green in water.

In conclusion, the nanoconfinement of $\text{Mg}(\text{BH}_4)_2 \cdot 1.47\text{NH}_3$ in the pores of SBA-15 scaffold with different degrees of pore filling of 100%-300% (MI100-MI300) is synthesized by melt infiltration. The confined samples show good thermal stability up to ~ 100 °C. Among the confined samples, the MI200 shows good reversible ion conductivity upon cycling, relatively high Mg^{2+} ion conductivity of 9.1×10^{-6} – 2.7×10^{-4} $\text{S}\cdot\text{cm}^{-1}$, and low activation energy of 0.69 eV at $T=32$ – 80 °C. The recrystallization of $\text{Mg}(\text{BH}_4)_2 \cdot 1.47\text{NH}_3$ is found and pronounced in the sample with high degree of pore filling. Solid-state NMR results indicate the successful stabilization of highly dynamic molten state of $\text{Mg}(\text{BH}_4)_2 \cdot 1.47\text{NH}_3$ through nanoconfinement.

4.3 References

- Atilio Puzkiel, J. (2019). Tailoring the Kinetic Behavior of Hydride Forming Materials for Hydrogen Storage. In M. Rahman and A. Mohammed Asiri (Eds.), *Gold Nanoparticles—Reaching New Heights*. IntechOpen. <https://doi.org/10.5772/intechopen.82433>
- Bösenberg, U., Ravnsbæk, D. B., Hagemann, H., D’Anna, V., Minella, C. B., Pistidda, C., ... Dornheim, M. (2010). Pressure and Temperature Influence on the Desorption Pathway of the LiBH_4 – MgH_2 Composite System. *The Journal of Physical Chemistry C*, *114*(35), 15212–15217. <https://doi.org/10.1021/jp104814u>
- Cova, F., Rönnebro, E. C. E., Choi, Y. J., Gennari, F. C., and Larochette, P. A. (2015). New Insights into the Thermodynamic Behavior of 2LiBH_4 – MgH_2 Composite for Hydrogen Storage. *The Journal of Physical Chemistry C*, *119*(28), 15816–15822. <https://doi.org/10.1021/acs.jpcc.5b02047>
- Jones, L. F., Dollimore, D., and Nicklin, T. (1975). Comparison of experimental kinetic decomposition data with master data using a linear plot method. *Thermochimica Acta*, *13*(2), 240–245. [https://doi.org/10.1016/0040-6031\(75\)80085-2](https://doi.org/10.1016/0040-6031(75)80085-2)
- Kamitsos, E. I., Karakassides, M. A., and Chryssikos, G. D. (1987). Vibrational spectra of magnesium-sodium-borate glasses. 2. Raman and mid-infrared investigation of the network structure. *The Journal of Physical Chemistry*, *91*(5), 1073–1079. <https://doi.org/10.1021/j100289a014>

- Nyallang Nyamsi, S., Lototsky, M. V., Yartys, V. A., Capurso, G., Davids, M. W., and Pasupathi, S. (2021). 200 NL H₂ hydrogen storage tank using MgH₂-TiH₂-C nanocomposite as H storage material. *International Journal of Hydrogen Energy*, 46(36), 19046–19059. <https://doi.org/10.1016/j.ijhydene.2021.03.055>
- Sharp, J. H., Brindley, G. W., and Achar, B. N. N. (1966). Numerical Data for Some Commonly Used Solid State Reaction Equations. *Journal of the American Ceramic Society*, 49(7), 379–382. <https://doi.org/10.1111/j.1151-2916.1966.tb13289.x>
- Surrey, A., Bonatto Minella, C., Fechler, N., Antonietti, M., Grafe, H.-J., Schultz, L., and Rellinghaus, B. (2016). Improved hydrogen storage properties of LiBH₄ via nanoconfinement in micro- and mesoporous aerogel-like carbon. *International Journal of Hydrogen Energy*, 41(12), 5540–5548. <https://doi.org/10.1016/j.ijhydene.2016.01.163>
- Thongtan, P., Dansirima, P., Thiangviriyaya, S., Thaweelap, N., Suthummapiwat, A., Plerdsranoy, P., and Utke, R. (2018). Reversible hydrogen sorption and kinetics of hydrogen storage tank based on MgH₂ modified by TiF₄ and activated carbon. *International Journal of Hydrogen Energy*, 43(27), 12260–12270. <https://doi.org/10.1016/j.ijhydene.2018.04.171>
- Yan, Y., Dononelli, W., Jørgensen, M., Grinderslev, J. B., Lee, Y.-S., Cho, Y. W., ... Jensen, T. R. (2020). The mechanism of Mg²⁺ conduction in ammine magnesium borohydride promoted by a neutral molecule. *Physical Chemistry Chemical Physics*, 22(17), 9204–9209. <https://doi.org/10.1039/D0CP00158A>
- Yan, Y., Grinderslev, J. B., Burankova, T., Wei, S., Embs, J. P., Skibsted, J., and Jensen, T. R. (2022a). Fast Room-Temperature Mg²⁺ Conductivity in Mg(BH₄)₂·1.6NH₃-Al₂O₃ Nanocomposites. *The Journal of Physical Chemistry Letters*, 13(9), 2211–2216. <https://doi.org/10.1021/acs.jpcllett.2c00136>
- Yan, Y., Grinderslev, J. B., Burankova, T., Wei, S., Embs, J. P., Skibsted, J., and Jensen, T. R. (2022b). Fast Room-Temperature Mg²⁺ Conductivity in Mg(BH₄)₂·1.6NH₃-Al₂O₃ Nanocomposites. *The Journal of Physical Chemistry Letters*, 13(9), 2211–2216. <https://doi.org/10.1021/acs.jpcllett.2c00136>

- Yan, Y., Grinderslev, J. B., Jørgensen, M., Skov, L. N., Skibsted, J., and Jensen, T. R. (2020). Ammine Magnesium Borohydride Nanocomposites for All-Solid-State Magnesium Batteries. *ACS Applied Energy Materials*, 3(9), 9264–9270. <https://doi.org/10.1021/acsaem.0c01599>
- Zhai, B., Xiao, X., Lin, W., Huang, X., Fan, X., Li, S., ... Chen, L. (2016). Enhanced hydrogen desorption properties of $\text{LiBH}_4\text{-Ca}(\text{BH}_4)_2$ by a synergetic effect of nanoconfinement and catalysis. *International Journal of Hydrogen Energy*, 41(39), 17462–17470. <https://doi.org/10.1016/j.ijhydene.2016.06.170>
- Zhang, J., Li, Z., Wu, Y., Guo, X., Ye, J., Yuan, B., ... Jiang, L. (2018). Recent advances on the thermal destabilization of Mg-based hydrogen storage materials. *RSC Advances*, 9(1), 408–428. <https://doi.org/10.1039/C8RA05596C>
- Zhao, Y., Liu, H., Liu, Y., Wang, Y., Yuan, H., and Jiao, L. (2017). Synergistic effects of destabilization, catalysis and nanoconfinement on dehydrogenation of LiBH_4 . *International Journal of Hydrogen Energy*, 42(2), 1354–1360. <https://doi.org/10.1016/j.ijhydene.2016.03.102>

CHAPTER V

CONCLUSION

In summary, this research inspected two aspects of Mg-based hydride materials including hydrogen storages and batteries. For hydrogen storage applications, the small tank containing nanoconfined $2\text{LiBH}_4\text{-MgH}_2$ into the pores of activated carbon (AC) and the $\text{TiF}_4\text{-MWCNT}$ -doped MgH_2 -based tank were studied. Regarding solid-state batteries, the nanoconfined $\text{Mg}(\text{BH}_4)_2 \cdot 1.47\text{NH}_3$ into the pores of the SBA-15 scaffold was investigated.

For the small tank (packing volume of 21.7 mL) containing nanoconfined $2\text{LiBH}_4\text{-MgH}_2$ into the pores of AC, de/rehydrogenation pathways and performances were investigated. Total and material hydrogen storage capacities upon five de/rehydrogenation cycles were 3.56-4.55 and 2.03-3.28 wt. % H_2 , respectively. The deficient reversible capacity with respect to the theoretical capacity was due to partial decomposition of LiBH_4 during sample preparation, incomplete dehydrogenation of LiBH_4 , and formation of thermally stable $\text{Li}_2\text{B}_{12}\text{H}_{12}$ upon cycling. Several reaction pathways during de/rehydrogenation were observed. For dehydrogenation at 358-382 °C, two-step reaction of $\text{MgH}_2 \rightarrow \text{Mg} + \text{H}_2$ and $\text{Mg} + \text{LiBH}_4 \rightarrow \text{MgB}_2 + \text{LiH} + 3\text{H}_2$ were detected at high and low pressure, respectively. The effective formation of MgB_2 was found at high temperature and under 3.3-3.6 bar H_2 . In the case of rehydrogenation at $T > 400$ °C under 30-40 bar H_2 , absorption of Mg to MgH_2 was found at high pressure, while that of $\text{MgB}_2 + \text{LiH}$ to produce $\text{LiBH}_4 + \text{Mg}$ was at lower pressure. At $T < 400$ °C, hydrogenation of $\text{MgB}_2 + \text{LiH}$ to form $\text{LiBH}_4 + \text{MgH}_2$ was achieved. To accomplish controllable reaction mechanisms of the hydride tank, the effective thermal conductivity of materials, a well-designed temperature control system, and high hydrogen permeability were necessary. Shifting focus to the study of $\text{TiF}_4\text{-MWCNT-MgH}_2$. The dehydrogenation kinetics at different operating temperatures ($T = 300\text{-}340$ °C) and hydrogen mass flow rates ($\text{H}_2\text{-FR} = 0.6\text{-}1.0$ SLM) was investigated. For the laboratory scale (1.8320 g), dehydrogenation rate was enhanced with $\text{H}_2\text{-FR}$, whereas

kinetic behaviors and rate-limiting step were constant as geometrical contraction model and R2, respectively. For tank scale (45.2252 g), comparable dehydrogenation kinetics was for all H₂-FR at T=300 °C. The change of dehydrogenation kinetics with temperatures was found at H₂-FR = 0.6 SLM. At low temperature, slow dehydrogenation compatible with low H₂-FR led to no accumulation of the desorbed hydrogen inside the tank. For the experiments at high temperature, the enhanced kinetics yielded to constant hydrogen release rate (0.6 SLM) for longer period. To accomplish the best dehydrogenation kinetics, higher H₂-FR (1.0 SLM) was required at elevated temperature. For kinetic behaviors, the best fitted model in laboratory and tank scale under almost all temperatures and H₂-FR were comparable as geometrical contraction. At low temperature, the enhanced sample mass to tank scale resulted in the change of rate-limiting step from two-to three-dimensional growth (R2 to R3). Dehydrogenation at high H₂-FR (1.0 SLM) might result in fluid dynamic restriction due to significantly different hydrogen diffusion at H₂ in/outlet and in the hydride beds.

Furthermore, nanoconfinement of Mg(BH₄)₂·1.47NH₃ composite in the porous scaffold SBA-15 was achieved through melt infiltration with different degrees of pore filling (100-300%). The confined samples (MI100-MI300) revealed a high thermal stability up to ~100 °C. PXD results revealed the amorphous state of Mg(BH₄)₂·1.47NH₃ composite in MI100 and a small excess of Mg(BH₄)₂·NH₃ on the surface of SBA-15 in MI200 and MI300. Solid-state ¹¹B NMR results indicated the present of the highly dynamic molten state of Mg(BH₄)₂·1.47NH₃ in all confined samples, resulting in high Mg²⁺ ionic conductivity and reduced activation energy. Interestingly, the highest Mg²⁺ ionic conductivity of 9.1×10^{-6} - 2.7×10^{-4} S·cm⁻¹ with low activation energy of 0.69 eV at T = 32-80 °C were obtained from the MI200.

CURRICULUM VITAE

- Name** Miss Pammarin Dansirima
- Education** 2013 – 2017 B.Sc. (First class Honors) Chemistry, Suranaree University
2017 – present Ph.D. candidate (Chemistry), Suranaree University
- Scholarship** The Royal Golden Jubilee Ph.D. Program
- Awards** Oral presentation at The TSRI Congress 2019. (the second runner-up)
- Publications**
- 1 P. Plerdsranoy, P. Dansirima, T. R. Jensen and R. Utke, *Int. J. Hydrog. Energy*, 2023, **48**, 28435–28444.
 - 2 P. Dansirima, S. Thiangviriyaya, P. Plerdsranoy, N. Chanlek and R. Utke, *RSC Adv.*, 2023, **13**, 16926–16934.
 - 3 Y. Shang, O. Jin, J. A. Puzskiel, F. Karimi, P. Dansirima, C. Sittiwet, R. Utke, S. Soontaranon, T. T. Le, G. Gizer, D. V. Szabó, S. Wagner, C. Kübel, T. Klassen, M. Dornheim, A. Pundt and C. Pistidda, *Int. J. Hydrog. Energy*, 2022, **47**, 37882–37894.
 - 4 P. Dansirima, A. Pagon, O. Utke and R. Utke, *Int. J. Hydrog. Energy*, 2022, **47**, 7351–7361.
 - 5 C. Sitthiwet, P. Plerdsranoy, P. Dansirima, P. Eiamlamai, O. Utke and R. Utke, *J. Alloys Compd.*, 2020, **832**, 155026.
 - 6 P. Dansirima, L. Ngamwongwan, S. Suthirakun, O. Utke and R. Utke, *RSC Adv.*, 2020, **10**, 33171.
 - 7 S. Thiangviriyaya, P. Plerdsranoy, C. Sitthiwet, P. Dansirima, P. Thongtan, P. Eiamlamai, O. Utke and R. Utke, *Int. J. Hydrog. Energy*, 2019, **44**, 20173–20182.
 - 8 P. Plerdsranoy, S. Thiangviriyaya, P. Dansirima, P. Thongtan, D. Kaewsuwan, N. Chanlek and R. Utke, *J. Phys. Chem. Solids*, 2019, **124**, 81–88.
 - 9 P. Dansirima, S. Thiangviriyaya, P. Plerdsranoy, O. Utke and R. Utke, *Int. J. Hydrog. Energy*, 2019, **44**, 10752–10762.
 - 10 P. Thongtan, P. Dansirima, S. Thiangviriyaya, N. Thaweelap, A. Suthummapiwat, P. Plerdsranoy and R. Utke, *Int. J. Hydrog. Energy*, 2018, **43**, 12260–12270.